Tuning apicobasal polarity and junctional recycling in the hemogenic endothelium orchestrates the morphodynamic complexity of emerging pre-hematopoietic stem cells

Léa Torcq,[1,2] Sara Majello,[1] Catherine Vivier,[1] and Anne A. Schmidt [1,6,*]

[1] Institut Pasteur, Université Paris Cité, CNRS UMR3738, Department of Developmental and Stem Cell Biology, F-75015 Paris, France

[2] Sorbonne Université, Collège doctoral, F-75005 Paris, France

[6] Lead contact

* Correspondence: anne.schmidt@pasteur.fr

Abstract

Hematopoietic stem cells emerge in the embryo from an aortic-derived tissue called the hemogenic endothelium (HE). The HE appears to give birth to cells of different nature and fate but the molecular principles underlying this complexity are largely unknown. Here we show, in the zebrafish embryo, that two cell types emerge from the aortic floor with radically different morphodynamics. With the support of live imaging, we bring evidence suggesting that the mechanics underlying the two emergence types rely, or not, on apicobasal polarity establishment. While the first type is characterized by reinforcement of apicobasal polarity and maintenance of the apical/luminal membrane until release, the second type emerges via a dynamic process reminiscent of trans-endothelial migration. Interfering with Runx1 function suggests that the balance between the two emergence types depends on tuning apicobasal polarity at the level of the HE. In support of this and unexpectedly, we show that the zebrafish Pard3 isoform - Pard3ba - is sensitive to interference with Runx1 activity, in aortic endothelial cells. This supports the idea of a signaling cross talk controlling cell polarity and its associated features, between aortic and hemogenic cells. In addition, using new transgenic fish lines that express Junctional Adhesion Molecules and functional interference, we bring evidence for the essential role of ArhGEF11/PDZ-RhoGEF in controlling the HE-endothelial cell dynamic interface, including cell-cell intercalation, which is ultimately required for emergence completion. Overall, we highlight critical cellular and dynamic events of the endothelial-to-hematopoietic transition that support emergence complexity, with a potential impact cell fate.

Major subject areas: Developmental Biology and Stem cells, Cell Biology.

Keywords: hematopoiesis, stem cell, cell extrusion, hemogenic endothelium, endothelial-to-hematopoietic transition, apico-basal polarity, Pard3, JAMs, zebrafish.

Introduction

Hematopoietic stem cells (HSCs) endowed with full regenerative potential in adult vertebrates are generated during a narrow-time window of few days during embryonic development. These cells, at the root of all blood and immune cells in the body, emerge from intra-embryonic aortic vessels and, more specifically, from a specialized type of vascular tissue called the hemogenic endothelium (HE, (Wu and Hirschi 2021)). A series of seminal studies have evidenced the autonomous production of repopulating HSCs within an intraembryonic region called the Aorta-Gonad-Mesonephros (AGM), before their appearance in other hematopoietic organs (A. L. Medvinsky et al. 1993; Müller et al. 1994; Garcia-Porrero, Godin, and Dieterlen-Lièvre 1995; A. Medvinsky and Dzierzak 1996; Cumano, Dieterlen-Lievre, and Godin 1996). Thereafter, the endothelial origin of HSCs was evidenced (Jaffredo et al. 1998; de Bruijn et al. 2002; T. E. North et al. 2002). The direct visualization, in real-time, of the emergence of precursors of hematopoietic stem and progenitor cells (HSPCs) from the dorsal aorta, termed the Endothelial-to-Hematopoietic Transition (EHT), was finally achieved *in vitro* (Eilken, Nishikawa, and Schroeder 2009), *ex-vivo* from mouse sections (Boisset et al. 2010), and *in vivo* in the zebrafish embryo (Bertrand et al. 2010; Kissa and Herbomel 2010), using live microscopy. This opened the way to a more detailed analysis of the characteristics of the HE at the transcriptional level, revealing its transient nature and its early hematopoietic commitment (Swiers et al. 2013).

The HE is characterized by inherent heterogeneity and is not only contributing to the formation of precursors to long-term HSCs (pre-HSCs) but also to more restricted progenitors (Hadland and Yoshimoto 2018). These progenitors can be born from HE sub-types that are found in extra-embryonic source such as the yolk-sac – in which case it gives rise to erythro-myeloid progenitors that will sustain erythro-myelopoiesis until birth (Frame et al. 2016) -, or both from extra and intra-embryonic sources (the yolk sac and the dorsal aorta) in which cases

63 progenitors are biased, such as for example in the mouse, toward T- and B- innate-type
64 lymphoid progenitors (Yoshimoto et al. 2011; 2012) or toward less restricted, multipotent
65 progenitors (Hadland and Yoshimoto 2018; Dignum et al. 2021). Importantly, while some of
66 the non-HSC derived progenitors born during embryonic life only support the functions of the
67 immune system during embryonic/ fetal life, others can persist in the adult to exert tissue-
68 resident functions, as has been mainly described in the mouse (Ghosn et al. 2019). However,
69 studies in human embryos support the idea that developmental hematopoiesis is highly similar
70 in mice and humans (Ivanovs et al. 2011; 2017).
71 A key question regarding the issue of the capacity of the HE to give birth to cells endowed with
72 different hematopoietic potential is whether this comes from HE cells of distinct origin (in which
73 case the HE would be a mosaic of precursors with distinct potential) or if this results from
74 extrinsic environmental cues that impose variability in the constantly evolving developmental
75 context (for a discussion, see (Barone et al. 2022)).
76 To address this type of question, high-resolution experimental settings need to be developed,
77 if possible at the single-cell resolution. Along this line, recent developments of transcriptomics,
78 including single cell RNAseq, spatially resolved in situ transcriptomic approaches, and in situ
79 barcoding, have been invaluable (Weijts, Yvernogeau, and Robin 2021). Among those high-
80 resolution approaches, cell fate mapping and lineage tracing approaches that include imaging
81 technologies have been very instrumental, particularly when performed with the zebrafish
82 model that reproduces many aspects of developmental hematopoiesis in higher vertebrates
83 (Orkin and Zon 2008). Recently, work performed in the zebrafish embryo has brought evidence
84 for heterogeneity of hematopoietic stem cell precursors being born from the HE, in the ventral
85 floor of the dorsal aorta and independently from HSCs, including a wave of transient T-
86 lymphocytes (using temporally-spatially resolved fate-mapping, (Tian et al. 2017)) and lympho-
87 myeloid biased progenitors born from a myeloid-lymphoid biased Spi2+ HE that appears to co-
88 exist with an erythroid-biased HE (using single-cell RNA-sequencing, (Xia et al. 2023)).

While light starts to be shed on the molecular and signaling cues that appear to regulate HE sub-specification and a continuum from arterial endothelium, HE maturation, and subsequent heterogeneity in HSPCs (Zhu et al. 2020), the essential molecular and cell biological properties that support HE functional plasticity remain to be determined.

Here, using the zebrafish embryo as a model, we complement our previous work describing essential molecular and mechanistic features of EHT cell emergence (Lancino et al. 2018). With the support of high-resolution live imaging and the generation of new transgenic fish lines that express a functional marker of cell polarity (Podocalyxin, a sialomucin of the CD34 family (Nielsen and McNagny 2008)), we show that the HE is giving birth to two cell types with distinct cell polarity status; these cells also emerge with radically different morphodynamic characteristics, which raises the intriguing possibility of an incidence of EHT emergence complexity on downstream fate, after release from the aortic wall.

To substantiate the significance of apico-basal polarity control in the EHT, we investigate on the potential involvement of Pard3 proteins. These proteins, recruited by transmembrane receptors via their PSD-95/Dlg/ZO-1 (PDZ) domains (Buckley and St Johnston 2022), are at the root of apicobasal polarity initiation and are essential for the maintenance of apical membrane functional properties (Román-Fernández and Bryant 2016). Among the four Pard3 isoforms expressed in the zebrafish (encoded by four different genes and non-including splicing variants), we describe the specific expression of the zebrafish Pard3ba isoform in the aorta, during the EHT time-window. We show that the expression of Pard3ba is sensitive to interference with the transcription factor Runx1 whose function is essential for EHT completion (Kissa and Herbomel 2010) and for regulating HSC number (Adamo et al. 2009; T. E. North et al. 2009). In link with apico-basal polarity and to address its incidence on the biomechanics of the emergence of the two EHT cell types that we describe, we generated new fish lines that express Junctional Adhesion Molecules (JAMs) fused with eGFP (eGFP-JAMs). The JAMs belong to tight junction complexes (Garrido-Urbani, Bradfield, and Imhof 2014) and recruit

115 Pard3 via direct interaction with their carboxy-terminus (Ebnet et al. 2003), thereby allowing
116 initiation of apico-basal polarity. With our eGFP-JAMs fish lines, we investigate on the function
117 of ArhGEF11/PDZ-RhoGEF that was shown to be involved in disrupting junctional integrity in
118 the context of the epithelial-to-mesenchymal transition as well as in the growth and migration
119 of invasive cancer cells (more specifically one splicing variant of its c-terminus conserved in
120 mammalian species, Itoh et al. 2017; Lee et al. 2018). We reveal the function of
121 ArhGEF11/PDZ-RhoGEF in the dynamic interplay between HE/EHT cells and their endothelial
122 neighbors, particularly in cell-cell intercalation which is essential for EHT completion and the
123 proper sealing of the aortic floor.
124

125 # Results

126 **Apicobasal polarity determines emergence types**

127 Our previous work describing the morphodynamic evolution of cells emerging from the aortic
128 floor through the EHT (hereafter designated as "EHT cells"), in the zebrafish embryo, revealed
129 the unusual feature of a cell extruding from the plane of a tissue while maintaining its
130 luminal/apical membrane until the very end of the release process, thus contributing to its
131 peculiar crescent-shaped morphology (Kissa and Herbomel 2010; Lancino et al. 2018), and
132 see the cartoons in ***Figure 1A***). However, to our knowledge, the polarity status of EHT cells
133 has not been investigated so far and the maintenance of a *bona fide* apical domain has never
134 been proven (with the luminal membrane enriched in apically targeted proteins and physically
135 delimited by apical polarity factors and tight junction complexes (Rodriguez-Boulan, Müsch,
136 and Le Bivic 2004; Buckley and St Johnston 2022)). Importantly, the fate of this apical-luminal
137 membrane, after the release, may lead to cells potentially endowed with specific functional
138 features. For example, this membrane surface may be directly and fully exposed to the
139 extracellular space or released in the cytoplasm of EHT cells for recycling and/or degradation,
140 after emergence completion (for examples of different scenarios, see ***Figure 1A,*** and the
141 legend for more details). Overall, this could lead to precursors of hematopoietic stem cells that,
142 ultimately, may be differentially fated.

143 To address the polarity status of EHT cells, we raised transgenic fish lines that express
144 endogenous Podocalyxin (Podxl2, (Herwig et al. 2011)). Podocalyxin was shown to take part
145 in the formation of the preapical domain during polarization and in the regulation of its oriented
146 organization, in tissue culture (Meder et al. 2005; Bryant et al. 2014). Its contribution to
147 lumenization *in vivo*, in the mouse aorta, has been described and it involves negative charge
148 repulsion induced by their glycosyl residues (Strilić et al. 2009; 2010).

149 We first attempted to express transiently, in the vascular system, the full-length Podxl2
150 zebrafish protein fused to eGFP at its extreme N-terminus. We failed to detect the fusion

151 protein at any time point relevant for observing easily the EHT process (a time window ranging
152 from 48 to 72 hpf (hours post-fertilization)); therefore, we designed a N-ter truncated form
153 deleted of the mucin domain and that retains amino-acids 341-587 fused to eGFP at its N-
154 terminus (***Figure 1B*** *and see* ***Methods***). Transient transgenesis revealed that this truncated
155 version is detected and is targeted to the luminal membranes of EHT cells. We then raised 2
156 transgenic (*Tg*) fish lines that express the N-ter truncated form of Podxl2 fused to either eGFP
157 (thereafter abbreviated eGFP-podxl2) and under the control of the Kdrl:Gal4 driver
158 *Tg(Kdrl:Gal4;UAS:RFP; 4xNR:eGFP-podxl2)*, or to mKate2 and under the control of the Kdrl
159 promoter *Tg(Kdrl:mKate2-podxl2)*. We observed that eGFP-podxl2 is enriched at the luminal
160 side of crescent-shaped EHT undergoing cells (see ***Figure 1C, Figure 1 - figure supplement***
161 ***1A*** and ***Figure 1 – video 1*** (z-stack at t = 0) and their legends for the details of the
162 luminal/apical membrane evolution through time). Thereafter, these cells will be referred to as
163 EHT pol+ cells.
164 We also followed the cell after emergence and observed the evolution of the luminal/apical
165 membrane appearing as internal pseudo-vacuoles. We illustrate the reduction of their volume
166 via membrane retrieval and, ultimately, their remanence as an intracellular membrane
167 compartment which we define as a post-EHT signature (***Figure 1- figure supplement 1A*** and
168 ***Figure 1- video 2*** (z-stack at t = 80 min)); we propose a model for the intracellular evolution
169 of the luminal/apical membrane (***Figure 1- figure supplement 1B***) which, unfortunately,
170 cannot be traced after 2-3 hrs post-emergence because of the apparent short half-life of eGFP-
171 podxl2 and of the drop in activity of the Kdrl promoter. Of notice, the pseudo-vacuoles are
172 reminiscent of the cystic formations observed in EHT cells in the mouse and visualized by
173 electron-microscopy (T. North et al. 1999; Marshall and Thrasher 2001) and also of the
174 vacuolar structures recently described in EHT cells in avian embryos (Sato et al. 2023; for
175 more details, see ***Discussion***).

176 While imaging the EHT using the Podxl2 expressing lines that clearly delimitate the luminal
177 membrane, we unambiguously identified a second type of emergence. This second cell type
178 is primarily characterized by a round-to-ovoid morphology (cells never bend as crescent-
179 shaped EHT pol+ cells, see ***Figure 1D*** and ***Figure 1 – video 3*** for a time-lapse sequence).
180 Importantly, these cells do not show any enrichment of eGFP-podxl2 at the luminal membrane
181 and will be referred to as EHT pol- cells. EHT pol- cells were observed in all other *Tg* fish lines
182 that we are routinely imaging, including the *Tg(Kdrl:Gal4;UAS:RFP)* parental line that was used
183 for transgenesis, thus excluding the possibility that these cells result from an artefact due to
184 the expression of a deleted form of Podxl2 and/or to its overexpression (see also for example
185 our new *Tg(kdrl:eGFP-Jam3b)* fish line ***Figure 5C*** and ***Figure 6B***).
186 Finally, we have estimated that the ratio between EHT pol+ and EHT pol- cells is of
187 approximately 2/1, irrespective of the imaging time window and of the localization of
188 emergence along the aortic antero-posterior axis (starting from the most anterior part of the
189 AGM (at the limit between the balled and the elongated yolk) down to the caudal part of the
190 aorta facing the CHT). We observed that both EHT pol+ and EHT pol- cells divide during the
191 emergence and remain with their respective morphological characteristics after completing
192 abscission ***(Figure 1 – figure supplement 2);*** hence they appear as pairs of cells that exit the
193 aortic wall sequentially (as shown ***Figure 1C, D***). We also observed that both EHT pol+ and
194 EHT pol- cells express reporters driven by the hematopoietic marker CD41 ***(Figure 1 – figure***
195 ***supplement 3)***, which indicates that they are both endowed with hematopoietic potential.
196 Altogether, our results show that hematopoietic precursor cells emerging from the aortic floor
197 do so with heterogeneity in their morphodynamic characteristics. They also suggest that the
198 control of apico-basal polarity may be at the root of these specific emergence types.

199 **The immature HE is not polarized**

200 EHT pol+ and EHT pol- cells appear to emerge from the hemogenic endothelium (HE), the
201 latter constituting the virtually exclusive cell population of the aortic floor just prior to the

202 initiation of the EHT time-window (around 28 hpf, see (Zhao et al. 2022)). In this context, we
203 addressed the polarity status of HE cells and its evolution throughout the EHT (***Figure 2***).
204 Surprisingly, confocal microscopy using our *eGFP-podxl2* and *mKate2-podxl2* expressing fish
205 lines revealed that HE cells do not appear to be polarized, based on the absence of Podxl2
206 enrichment at luminal membranes, at the initiation of the EHT time-window and later (at
207 approximately 28 - 30 hpf, ***Figure 2 – figure supplement 1,*** see also at 35 hpf ***Figure 2A***, top
208 left panel, green arrows and ***Figure 2 - figure supplement 2*** and at 48 – 55 hpf ***Figure 3 –***
209 ***figure supplement 2A***). Interestingly, the cytoplasm of characteristic elongated HE cells
210 located on the aortic floor is filled with more-or-less large membrane vesicles that carry eGFP-
211 podxl2 (the largest vesicles reaching approximately 30μm in diameter). This suggests that HE
212 cells contain a reservoir of eGFP-podxl2 membranes that may be subjected to exocytose; as
213 such, HE cells may be comparable to endothelial cells organizing a vascular lumen and that
214 have been proposed to exocytose large intracellular macropinocytic-like vacuoles when
215 cultured in 3D extracellular matrices (Bayless and Davis 2002; Davis, Bayless, and Mavila
216 2002) or, *in vivo*, in the zebrafish model (Kamei et al. 2006; Lagendijk, Yap, and Hogan 2014).
217 This finding is unexpected since HE cells are assumed to possess aortic cell characteristics
218 (i.e exhibit an apicobasal polarity) as they are supposedly integrated in the aortic wall
219 contemporarily to aortic precursors (Jin et al. 2005) and may have been taking part in the
220 lumenization of the ancestral vascular cord, a process that takes place around 18-20 hpf.
221 Consequently, loss of apicobasal polarity features of HE cells at 28-30 hpf may be part of the
222 programme that initiates the EHT process.
223 Although technically difficult for long hours (because of important variations in the volume of
224 the balled yolk that trigger drifting of embryos), we have been able to follow over time non-
225 polarized HE cells and to visualize the evolution of their vesicular content, starting at the
226 initiation of the EHT time-window (around 35 hpf, see ***Figure 2*** and ***Figure 2 – figure***
227 ***supplement 2***). Interestingly, we could follow a dividing HE cell for which the vesicular content
228 labelled with eGFP-podxl2 appeared to partition unequally between daughter cells (***Figure 2A,***

229 t = 30 min, HE cell 1' inherits the largest macropinocytic-like vacuole (green asterisk) and
230 emerges unambiguously as an EHT pol+ cell (t = 360 min, EHT cell 1'), with eGPF-podxl2
231 enriched at the apical/luminal membrane (surrounding the green asterisk) and virtually
232 undetected at the basal membrane (magenta arrow)). This suggests that asymmetric
233 inheritance of cytosolic vesicles containing apical proteins may contribute, presumably after
234 delivery to the luminal membrane, to specify the apical membrane of EHT pol+ cells.

235 Altogether, these results support the idea that the HE, at the initiation of the EHT time-window,
236 is not polarized. Subsequently, HE cells establish – or not – apical and basal membrane
237 domains, which characterizes EHT pol+ or EHT pol- cell types, respectively (see our
238 hypothetical model ***Figure 2B***). In the case of EHT pol+ cells and while emergence is
239 proceeding, apicobasal polarity is maintained (if not reinforced) until the release.

240 **Interfering with Runx1 function alters HE maturation, the EHT progression, and the**
241 **balance between EHT cell types**

242 To provide functional support to our findings and hypotheses on apico-basal polarity control in
243 the gradual maturation of the HE throughout the EHT time-window, we thought of interfering
244 with the activity of the transcription factor Runx1 whose expression is sensitive to fluid sheer
245 stress (Adamo et al. 2009).

246 To interfere with Runx1 function, we generated a *Tg* fish line that expresses a truncated form
247 of Runx1 (dt-runx1; fish line *Tg(Kdrl:Gal4;UAS:RFP;4xNR:dt-runx1-eGFP)* thereafter
248 abbreviated *Tg(dt-runx1)*) deleted from its transactivation domain and carboxy-terminus but
249 retaining its DNA-binding domain (the Runt domain (aa 55-183, (Kataoka et al. 2000; Burns et
250 al. 2002; Kalev-Zylinska et al. 2002), see ***Figure 3C)***. Importantly, in this *Tg* fish line, dt-runx1
251 expression is restricted to the vascular system, hence excluding expression in the brain region
252 that express Runx1 endogenously (see the aforementioned articles) and preventing biases
253 owing to potential interference with neuronal functions. In addition, owing to the expression of
254 eGFP concomitantly to dt-runx1 (the C-terminal eGFP is cleaved from dt-runx1 via a T2a site

255 for endopeptidase, see cartoons at the top of panel C), this fish line allows for the easy
256 selection of embryos for imaging and for phenotypic analysis. In preliminary experiments
257 aimed at addressing the localization of dt-runx1 as well as its stability, we expressed it
258 transiently and measured its proper targeting to the nucleus (the construct also contains a
259 double HA (2xHA) epitope for immuno-detection, see ***Figure 3C****).*
260 To characterize further the *Tg(dt-runx1)* fish line, we addressed the incidence of dt-Runx1
261 expression on HE and EHT cell populations during the EHT time-window as well as later on,
262 at 5 days post-fertilization (5dpf) in the thymus, as a readout of hematopoiesis efficiency. We
263 made the following observations:
264 Firstly, using 48 - 55 hpf *Tg(dt-runx1)* embryos and live imaging we observed, in comparison
265 to controls, a significant accumulation of HE cells (see ***Figure 3A***, top and bottom panels (he,
266 arrowheads), see also the quantifications ***Figure 3B***, top graph, median value of 17 cells for
267 controls and 25 cells for mutants). In the mutant condition, the bulk of HE cells also include
268 uncharacterized EHT cells (***Figure 3A***, middle panel, blue arrows); hypothetically, these may
269 be EHT cells at an early phase of their emergence, including cells that may have evolved as
270 EHT pol- cells in unperturbed conditions, owing to the absence of luminal membrane
271 invagination. We also observed the unusual tendency for the accumulation of EHT pol+ cells
272 (***Figure 3A***, green and pink arrows), with a maximum value of 3 cells per embryo for controls
273 that reached the unusual - never observed in control conditions -, values of 11, 9 and 8 cells
274 for 3 mutants out of 7 (***Figure 3B***, middle graph). In addition to the increase in the proportion
275 of EHT pol+ cells in the ventral side of the aorta (***Figure 3B***, right panel, with a value of 4% for
276 controls and reaching 7% for mutants, consistently with the increase in the absolute count per
277 embryo), we also observe an increase in the proportion of EHT pol+ cells in lateral sides of the
278 dorsal aorta (***Figure 3A***, pink arrows and ***Figure 3B***, right graph, with a value of 4% for controls
279 and reaching 9% for mutants). Finally, we did not observe any significant modification in the
280 number of EHT pol- cells (same median values for both controls and mutants, the values

281 oscillating between 0 and 1 cell per embryo, with only one example of an embryo exhibiting 2
282 apparent EHT pol- cells (***Figure 3B***, bottom graph)).
283 Secondly, using 48 - 55 hpf *Tg(dt-runx1)* embryos and controls *Tg(Kdrl:eGFP)* we confirm, by
284 whole mount in situ hybridization performed with an RNAscope probe specific for myb (***Figure***
285 ***3 – figure supplement 1***), that the cells that accumulate in the aortic floor of dt-Runx1 mutants
286 are indeed of hematopoietic nature (see the cells with RNAscope spots in magenta or marked
287 by blue arrows, ***Figure 3 – figure supplement 1A,*** zoomed areas). Unfortunately, chemical
288 fixation impaired the maintenance of EHT pol+ and EHT pol- specific cell shape, preventing us
289 from classifying emerging cell populations. However, cell counts after segmentation using the
290 Imaris software confirmed, based on cell localization, the specific increase of hemogenic/EHT
291 cells in aortic floors of mutants (median values of 34 and 16.5 for mutants and controls,
292 respectively, ***Figure 3 – figure supplement 1B*** (right panel) while no difference was measured
293 for endothelial roof cells between mutants and controls (left panel). Quantification of myb
294 positive cells confirmed the increase of hemogenic cells in the aortic floors of mutants in
295 comparison to controls, albeit with slightly smaller numbers (median values of 20.5 and 8.5 in
296 mutants and controls, respectively (***Figure 3 – figure supplement 1C***, middle panel)), most
297 probably because myb becomes detectable only when the EHT process has initiated. In
298 comparison to floor cells, very few roof cells express myb (median values of 2.0 and 1.5 in
299 mutants and controls, respectively (***Figure 3 – figure supplement 1C***, left panel)) consistently
300 with the idea that the aortic roof is not hemogenic (Zhao et al. 2022)). Importantly, the increase
301 of pre-hematopoietic cells in the aortic floor in the mutants correlates with a decrease in
302 hematopoietic cells lodging in the sub-aortic region, reinforcing the idea of impairment in EHT
303 cell emergence (***Figure 3 – figure supplement 1C***, right panel). Finally, quantification of the
304 number of myb RNAscope spots per segmented hemogenic cells highlights the important
305 increase in expression by hemogenic cells in the floor of dt-Runx1 mutants, in comparison to
306 controls (with median values of 4 and 0, respectively *(**Figure 3 – figure supplement 1D***, right
307 panel). In comparison, virtually none of the roof cells contain more than 2 spots (***Figure 3 –***

308 ***figure supplement 1D***, with 2/162 and 1/220 cells for the mutants and controls, respectively,
309 with median values of 0 for both conditions). Altogether, these last results confirm that pre-
310 hematopoietic cells accumulate in the aortic floor of dt-Runx1 mutants; the very substantial
311 increase in the detection of myb mRNAs suggests an increase in the residential time in the
312 aortic floor, which reinforces the idea that these cells are impaired in their release from the
313 aortic floor.
314 Thirdly, between 30 and 55 hpf, using live confocal microscopy and contrarily to what we
315 observed with our fish lines expressing either eGFP-podxl2 (***Figure 2 and Figure 2 – figure***
316 ***supplement 1 and 2***) or mKate2-podxl2 (***Figure 3 – figure supplement 2A***) in which HE cells
317 appear to be non-polarized, embryos obtained from outcrossing *Tg(dt-runx1) and*
318 *Tg(Kdrl:mKate2-podxl2)* fishes appear to contain polarized HE cells, based on enrichment of
319 the polarity marker at luminal membranes (***Figure 3 - figure supplement 2B)***.
320 Fourthly and occasionally, in live embryos, we observe - for EHT cells exhibiting invagination
321 of the luminal membrane -, scattered cytosolic and sub-plasmalemmal pools of Podxl2-
322 containing membranes and, consistently, the apparent decrease of Podxl2 enrichment at the
323 apical/luminal membrane (see ***Figure 3*** - ***figure supplement 2C*** and compare with ***Figure***
324 ***1C***). In addition and occasionally as well, we observe the reversion of apparent EHT pol+ cells
325 into apparent EHT pol- cells (data not shown). These last two observations suggest that
326 perturbing the control of apicobasal polarity in the HE, in the context of the dt-Runx1 mutant,
327 alters emergence morphodynamics, hypothetically and possibly more specifically in the case
328 of EHT pol- cells whose biomechanical features appear to require turning down the
329 establishment of apical and basal membrane domains.
330 Fifthly, hematopoiesis is affected far downstream of emergence, as attested by the significant
331 increase, at 5 dpf, in the number of hematopoietic cells in the thymus of dt-Runx1 mutants, in
332 comparison to control siblings (see ***Figure 3 - figure supplement 3A*** for images after cell
333 segmentation with the Imaris software accompanied by ***Figure 3 - video 1*** and ***Figure 3 -***
334 ***figure supplement 3B*** for quantifications showing significant increase in thymus volume (left

335 panel) owed to the increase in cell number (middle panel) rather than in cell volume (right
336 panel)).
337 Altogether, the results obtained upon expression of dt-runx1 show impairment of
338 hematopoiesis and suggest that, for both EHT cell types, the progression throughout EHT is
339 perturbed, and so until the release. The accumulation of morphologically characterized EHT
340 pol+ like cells that we observe may result from the sustained apicobasal polarity of the HE at
341 early and later time points. Conversely, characterized EHT pol- cells did not accumulate,
342 although we observed cells of uncharacterized morphology that could correspond to EHT pol-
343 cells that did not evolve properly. In addition, our results suggest that precursors of HE cells
344 are polarized, as is expected to be the case for non-hemogenic aortic cells, and that Runx1 is
345 involved in controlling the molecular events that are tuning apico-basal polarity, starting at the
346 initiation of the EHT time-window.

347 **Interfering with Runx1 activity unravels its function in the control of Pard3ba expression**
348 **and highlights heterogeneous spatial distribution of Pard3ba mRNAs along the aortic**
349 **axis**
350 We then explored the potential involvement of proteins of the Pard3 family during the EHT. We
351 anticipated that interfering directly with Pard3 proteins would hamper the development of the
352 aorta (in addition to other functions of polarized tissues that are essential for embryonic
353 development) and rather searched for correlative evidence for the differential expression of
354 Pard3 isoforms in the hemogenic endothelium, EHT cells and the aortic endothelium, both in
355 wild type and dt-Runx1 expressing embryos. To achieve this task, we analyzed the expression
356 of mRNAs encoding for the four Pard3 isoforms expressed in the zebrafish (***Figure 4A***) by
357 combining qRT-PCR on FACS-sorted endothelial cells and whole-mount *in situ* hybridization
358 at the cellular resolution, using RNAscope. All four Pard3 isoforms are composed of 3 PDZ
359 domains and 2 conserved regions upstream and downstream of these domains (CR regions,
360 ***Figure 4A***).

361 We first sought to measure expression of these different isoforms in the vascular system of 48
362 hpf embryos and, more restrictively, in the trunk region. To do so, we dissociated and FACS-
363 sorted cells of either whole embryos, or dissected trunks, using the *Tg(Kdrl:Gal4; UAS:RFP)*
364 fish line in which soluble RFP is expressed in endothelial tissues (***Figure 4 – figure***
365 ***supplement 1A***). RFP+ vascular cells were found the be slightly enriched in the trunk region,
366 in comparison to whole embryos (***Figure 4 – figure supplement 1A*****,** see the table with 2.10
367 versus 0.95 % of RFP+ cells in the trunk and the whole embryo, respectively). Using qRT-PCR
368 on the FACS-sorted cells, we found that the hematopoietic markers myb and runx1 were
369 heavily detected in RFP+ cell extracts in comparison to RFP- cells (***Figure 4 – figure***
370 ***supplement 1B);*** this suggests that part of the isolated RFP+ cells contain hemogenic and
371 hematopoietic cells (at 48 hpf, it is expected that some newly born hematopoietic cells are
372 retained in the sub-aortic space). When we measured the expression levels of the four Pard3
373 isoforms, we observed, in comparison to control RFP- cells, the enrichment of Pard3aa and
374 Pard3ba in extracts from RFP+ cells isolated from whole embryos, and the opposite for
375 Pard3ab and Pard3bb (***Figure 4 – figure supplement 1C***). These differences were conserved
376 with extracts from RFP+ cells isolated from trunk regions, except for Pard3ba for which
377 important variations in mRNA quantities were obtained, blurring conclusions (we shall come
378 back to this variability beneath). These results suggest that, at least based on the vascular
379 system of whole embryos, Pard3aa and Pard3ba exert functions in endothelial cells, with the
380 possibility of having more specific functions in aortic and HE cells. To discriminate between
381 cell types expressing Pard3aa and Pard3ba isoforms (and in particular vascular cell types), we
382 used RNAscope on whole mount *Tg(Kdrl:eGFP)* embryos, at 48 hpf. Confocal images focused
383 on trunk regions show that Pard3aa is strongly expressed in cells of the spinal cord (potentially
384 neuronal cells and/or radial glia), as well as in the notochord (***Figure 4 – figure supplement***
385 ***2A***). Interestingly, Pard3ba mRNAs are expressed in more restricted areas, in majority in the
386 spinal cord, albeit to a much lesser extent than for Pard3aa as well as in the region of the
387 pronephric duct and the gut epithelium (***Figure 4 – figure supplement 2B***). By curiosity and

388 because it appears to be the most highly expressed in the whole embryo (and hence may be
389 ubiquitously expressed, including in the trunk region and in accordance to the Daniocell
390 resource at https://daniocell.nichd.nih.gov/, Farrell et al. 2018; Sur et al. 2023), we also
391 investigated on the expression of Pard3ab mRNAs (***Figure 4 – figure supplement 2C***). We
392 confirmed its relatively ubiquitous expression in comparison to Pard3aa and Pard3ba, with a
393 massive expression in the spinal cord. To visualize more precisely expression levels in the
394 vascular system in the trunk (more specifically in the aorta and the underlying vein), we
395 zoomed in this region (***Figure 4 – figure supplement 2D***) and observed a homogeneous
396 localization of Pard3aa and Pard3ab mRNAs as well as, strikingly in the case of Pard3ba, a
397 quite heterogeneous localization of mRNAs unequally concentrated along the aortic axis
398 (***Figure 4 – figure supplement 2D,*** middle panel and see also ***Figure 4C***, top panel; these
399 will be referred thereon as Pard3ba mRNA enriched regions (MERs)). Of notice, in the whole
400 aorta, we observed more RNAscope signals for Pard3ab in comparison to Pard3aa and
401 Pard3ba, including in some HE/EHT cells (***Figure 4 – figure supplement 2D***, with positive
402 HE/EHT cells indicated by blue arrows). This indicates that the Pard3ab isoform, consistently
403 with the absence of variation upon dt-Runx1 expression (see beneath), is constitutively
404 expressed in some HE/EHT cells (this may be also the case for the Pard3aa isoform but this
405 should be taken with caution since its mRNAs are more in the limit of detection). We attempted
406 to detect Pard3 isoforms expressed in the vascular system, in the trunk region of the embryo,
407 with available antibodies raised against other species and failed, possibly because of inter-
408 species recognition limitation.
409 We then analyzed Pard3 mRNA levels in the context of dt-Runx1 expression. As we did for
410 *Tg(Kdrl:Gal4;UAS:RFP)* embryos, we isolated by FACS GFP+ and double positive
411 GFP+/RFP+ cells dissociated from dissected trunks of *Tg(dt-Runx1)* 48 hpf embryos. For
412 controls, we also isolated RFP+ cells from dissected *Tg(Kdrl:Gal4;UAS:RFP)* embryos (see
413 ***Methods*** and ***Figure 4 – figure supplement 3A***). qRT-PCR on isolated eGFP+ cells that
414 express dt-Runx1 revealed an increase of approximately 50% of the myb and runx1 mRNAs,

415 in comparison to RFP+ control cells (***Figure 4B,*** left panel), which is consistent with the
416 accumulation of hemogenic/EHT cells that we observe in ***Figure 3*** and in ***Figure 3 – figure***
417 ***supplement 1***. Interestingly, we obtained very little to no variation in the expression levels of
418 Pard3aa, ab and bb mRNAs in dt-Runx1 expressing eGFP+ cells in comparison to control
419 RFP+ cells but, again, a high variability in the case of Pard3ba mRNAs (***Figure 4B,*** right panel).
420 Using RNAscope, the non-homogeneous localization of Pard3ba mRNAs observed in controls,
421 along the aortic axis, was not only conserved but became even more obvious to the eye for dt-
422 Runx1 mutants, owing to the increase in the density of RNAscope spots (***Figure 4C,*** compare
423 top and bottom panels). Confocal images on several controls and dt-Runx1 mutants highlight
424 the heterogeneity in Pard3ba mRNA detection as attested by the variability in the localization
425 and number of RNAscope spots (compare in particular the 5 mutants shown in ***Figure 4 –***
426 ***figure supplement 3B***, right panels). Quantification of RNAscope spots per aortic segment
427 and per hemogenic/EHT cell using Imaris revealed an increase of almost 300% for the former
428 when comparing controls and mutants (median values of 65.00 and 167.50 for controls and
429 dt-Runx1 mutants, respectively, ***Figure 4D***) and that virtually no Pard3ba mRNA was detected
430 in the latter (median values of 0.00 spots per hemogenic/EHT cell for both controls and dt-
431 Runx1 mutants, ***Figure 4E***). A precise representation showing the hemogenic/EHT cell count
432 with RNAscope spots ranging from 0 to 4 reveals, for mutants in comparison to controls, a
433 significant increase in the number of hemogenic/EHT cells not expressing Pard3ba (***Figure 4***
434 ***– figure supplement 3C,*** first panel from the left), as well as a slight tendency for an increase
435 in the number of cells with 1 to 4 Pard3ba spots (***Figure 4 – figure supplement 3C,*** second
436 to fifth panels), with more significance for the population with 2 spots (middle panel). Overall,
437 in either control or mutant conditions, we detected the presence of RNAscope spots in very
438 few hemogenic/EHT cells (15/115 for controls and 21/224 for dt-Runx1 mutants, with a
439 maximum for 2 spots for controls and 4 spots for dt-Runx1 mutants, see ***Figure 4E*** and ***Figure***
440 ***4 – figure supplement 3C***).

441 Again, we obtained a large variability in the number of Pard3ba RNAscope spots per aortic
442 segment (the number of spots per aortic segment ranged from 10 to 94 for controls and from
443 53 to 366 for the mutants, see ***Figure 4D***); this mirrors what was obtained by qRT-PCR,
444 particularly for dt-Runx1 mutants (***Figure 4B,*** right panel). This is not the case for Pard3aa and
445 Pard3ab (see RNAscope images and quantifications ***Figure 4 – figure supplement 4***), which
446 is also consistent with qRT-PCR results (***Figure 4B,*** right panel). Importantly, expression of dt-
447 Runx1 neither influenced the expression of Pard3aa, nor of Pard3ab (***Figure 4 – figure***
448 ***supplement 4).***
449 Finally and importantly, in wild-type embryos, the Pard3ba mRNAs are preferentially localized
450 in the direct vicinity of hemogenic/EHT cells (***Figure 4F, G***). Indeed, more than 50% of Pard3ba
451 spots are localized within 5 to 10 μm of hemogenic/EHT cells (***Figure 4G*** middle panel), and
452 more than 75% of spots are localized within a 5 to 20μm distance (***Figure 4G*** right panel).
453 Interestingly, the number of hemogenic/EHT cells does not correlate with the absolute number
454 of spots (***Figure 4F,*** left panel, R = 0.34), but rather it strongly correlates with the spatial
455 densification of spots around hemogenic/EHT cells: the shorter the distance of the majority of
456 spots are of hemogenic/EHT cells (***Figure 4F,*** middle and right panel, representing 50% and
457 75% of spots respectively), the higher the hemogenic/EHT cell count (R = -0.84 and R = -0.83
458 respectively). This shows that AECs expressing Pard3ba mRNAs are mostly in direct contact
459 with cells committed to undergo EHT and suggests a signalling crosstalk occurring between
460 them. This densification of spots in MERs is reinforced upon expression of dt-Runx1 (***Figure***
461 ***4F,*** left panel*)*: we found that virtually all Pard3ba spots are localized within a 10-15μm distance
462 from hemogenic/EHT cells.
463 Altogether, these results unveil the Runx1-dependent control of the Pard3ba isoform
464 specifically, during the EHT. In the aorta, AECs appear to be the main cell type that expresses
465 this Pard3 isoform and, unexpectedly, expression in these cells is sensitive to interference with
466 our dt-Runx1 mutant. One plausible explanation is that AECs respond to Runx1-mediated
467 signalling taking place in HE/EHT cells (see ***Discussion*** for other possibilities and further

468 details). This suggests that a specific signalling axis is taking place between these different
469 cell types that would control the expression of Pard3ba mRNAs and, consequently,
470 downstream apico-basal polarity associated features carried out by the Pard3ba protein
471 isoform (example: the recycling mode of junctional complexes between EHT pol+ cells and
472 endothelial neighbours, in comparison to EHT pol- cells, see beneath and ***Discussion***). This
473 potential intercellular signalling is supported by the proximity of Pard3ba mRNAs expressed in
474 AECs to HE/EHT cells in MERs. These results also strengthen the importance of the interplay
475 between HE/EHT cells and their direct endothelial neighbours (this interplay has been
476 highlighted in Lancino et al. 2018; and see also beneath).

477 **Junctional recycling between EHT cell types and endothelial neighbours is differentially**
478 **controlled**

479 To investigate the functional links between apicobasal polarity and the peculiarities of EHT
480 pol+ and EHT pol- emergence processes, we sought to follow the dynamics of Junctional
481 Adhesion Molecules (JAMs) that belong to tight junction complexes (Garrido-Urbani, Bradfield,
482 and Imhof 2014). During apicobasal polarity establishment in epithelial and endothelial tissues,
483 these molecules recruit the Pard3/aPKC complex, via a PDZ-binding peptide located in their
484 extreme carboxy-terminus (***Figure 5A,*** left cartoons and (Itoh et al. 2001; Ebnet et al. 2001;
485 2018)). In addition, JAMs are expressed in the vascular system and, in relation to this work,
486 JAM3b is expressed in the aorta of the zebrafish embryo and promotes endothelial
487 specification and hematopoietic development (Kobayashi et al. 2020).
488 We envisaged a scenario whereby EHT pol+ cells, whose longitudinal interface with
489 endothelial neighbours shrinks along the X axis of the X, Y 2D-plane, may have less mobile
490 junctional pools than EHT pol- cells whose entire junctional interface moves along the X, Y, Z
491 3D-axes (***Figure 5 - figure supplement 1)***. In the case of EHT pol- cells, the consumption of
492 the junctional interface with adjoining endothelial cells appears to result from the converging
493 migration of endothelial neighbours crawling over the luminal membrane, based on

494 interpretation of our time-lapse sequences (***Figure 1- video 3***). In this context, we favoured
495 the analysis of junctional pools localized at antero-posterior sites of emerging cells as we have
496 shown that they are enriched with tight junction components (Lancino et al., 2018). In addition
497 and in the case of EHT pol+ cells, it is conceivable that these adhesion pools – spatially
498 restricted owing to apicobasal polarity –, contribute to anchoring the emerging cell in the 2D-
499 plane (***Figure 5 - figure supplement 1,*** top panel*).*

500 To achieve our goal, we designed 2 constructs in which eGFP is introduced in the extracellular
501 domains of the two JAM2a and JAM3b molecules (***Figure 5A,*** right cartoons). To investigate
502 their localization and proper targeting at junctional interfaces, these constructs were expressed
503 transiently and ubiquitously, using the *Hsp70* heat shock promoter. We observed that the 2
504 fusion proteins are efficiently targeted at cellular contacts (***Figure 5 - figure supplement 2B,***
505 ***C*** and ***F***, orange and white arrows) as well as at the apical side of polarized epithelia such as
506 for example cells of the ependymal canal (***Figure 5 - figure supplement 2A, E***, white arrows).
507 They were also observed at protrusions of epithelial cells and at T-tubules of muscle fibres (for
508 JAM2a and JAM3b, respectively, see ***Figure 5 - figure supplement 2D***, ***G***). We then
509 established *Tg* fish lines expressing eGFP-Jam2a and eGFP-Jam3b under the control of the
510 vascular kdrl promoter (*Tg(kdrl:eGFP-Jam2a)* and *Tg(kdrl:eGFP-Jam3b)*). Using these fish
511 lines and spinning disk confocal microscopy, we observed a remarkable efficiency of targeting
512 to intercellular junctions, for both proteins (data not shown for eGFP-Jam2a; for eGFP-Jam3b,
513 see ***Figure 5B*** and ***C***; in the maximum z-projections, the green signal is enriched at
514 intercellular junctions; in single z-plane images, an EHT pol+ cell and 2 EHT pol- cells are
515 visible in the left and right panels, respectively). Deployment of the aortic wall into 2D
516 cartographies using an algorithm described previously (Lancino et al. 2018) allows to point
517 precisely at junctional pools established at the interface between endothelial and EHT cells.
518 This emphasizes on the enrichment of eGFP-Jam3b at antero-posterior poles of EHT pol+ and
519 EHT pol- cells (***Figure 5B, C*** bottom panels*,* EHT and aortic endothelial cells (red and black

520 numbers, respectively) are visualized as if the eye is located inside the aortic lumen; red arrows
521 point at junctional reinforcements located at antero-posterior poles of EHT cells, black arrows
522 in the left panel point at tri-cellular junctions and the blue arrow in the right panel points at
523 intercalation of endothelial cells 3 and 6 between the EHT pol- cell (cell 2) and the endothelial
524 neighbour 7).
525 Using double transgenic *Tg(kdrl:eGFP-Jam3b; kdrl:nls-mKate2)* embryos at 48 - 55 hpf, we
526 addressed the recycling capacity of junctional pools using Fluorescence Recovery After
527 Photobleaching (FRAP; for more details, see ***Methods***). The labelling of nuclei with nls-
528 mKate2 allowed to point at EHT pol+ and EHT pol- cells unambiguously because eGFP-Jam3b
529 is essentially targeted to junctional interfaces and not labelling luminal/abluminal membranes
530 (***Figure 6A, B***), except in few cases (***Figure 5B***, for an EHT pol+ cell); additionally, nuclei of
531 EHT pol+ cells have a crescent shape (see ***Figure 6A)***.
532 First and to set up our protocol, we spotted bi- and tri-junctional contacts between endothelial
533 cells (***Figure 6 – figure supplement 1***). Recycling parameters (fluorescence intensity
534 recovery with time and maximum recovery amplitude (that addresses the mobile pool), ***Figure***
535 ***6C***) showed that bi-junctional contacts are less mobile than tri-junctions, with a higher
536 dispersion of maximum recovery amplitude values for the latter (***Figure 6E***); this introduced a
537 clear limitation for statistical significance of the results, although clear tendencies were
538 observed for mean fluorescence intensity recovery ***(Figure 6C)*** and median values for
539 maximum recovery amplitude, when recycling reached its equilibrium ***(Figure 6E)***. We then
540 focused at antero-posterior sites of EHT pol+ and EHT pol- cells and more specifically in the
541 region of tricellular junctions (shared by 1 EHT cell and 2 endothelial neighbours (***Figure 6A,***
542 ***B***, 2D-cartographies, black arrows) and for more examples in 2D-cartographies, see ***Figure 6***
543 ***– figure supplement 1,*** black arrows) that are clearly the most enriched with eGFP-Jam3b. In
544 each experiment, eGFP-Jam3b pools at tricellular junctions between endothelial cells (EC-EC-
545 EC) were also spotted for a comparative analysis. Measurements of fluorescence recovery
546 intensities revealed a tendency of increase in the mobile fraction of eGFP-Jam3b at EHT pol+

547 – EC versus EHT pol- – EC junctional interfaces (see ***Figure 6D*** for fluorescence recovery
548 curves and ***Figure 6E*** for median values (50% and 39% maximum recovery amplitudes after
549 10 min, respectively)). Although smaller, differences in recovery were also measured between
550 EHT pol+ – EC and EHT pol- – EC junctional interfaces when focusing on the earliest time
551 points (the first 30 seconds, ***Figure 6F***), with the median value of early recovery slopes for the
552 EHT pol+ - EC versus EHT pol- – EC junctional interfaces increased by 128% (***Figure 6G***).

553 Altogether and unexpectedly regarding our initial scenario, these results indicate that tri-
554 junctional pools localized at antero-posterior poles of EHT cells and enriched with eGFP-
555 Jam3b molecules are significantly more dynamic for EHT pol+ cells in comparison to EHT pol-
556 cells. Since EHT pol+ cells - by virtue of apicobasal polarity establishment possibly assemble
557 an apical endosome -, this should favour a faster recycling of eGFP-Jam molecules (see
558 ***Discussion*** for more details).

559 **ArhGEF11/PDZ-Rho GEF plays essential functions during EHT progression**

560 Junctional maintenance and recycling are dependent on intracellular membrane trafficking,
561 supported by sub-cortical actin remodelling and actomyosin contractility, which are controlled
562 mainly by GTPases of the Rho family (Ridley 2006; Olayioye, Noll, and Hausser 2019). Owing
563 to the significance of apicobasal polarity control on EHT features, as suggested by our work,
564 we investigated which proteins may be essential for actin/actomyosin regulation and focused
565 on regulators of Rho GTPases, in particular Rho GEFs that catalyse exchange of GDP for GTP
566 to positively regulate their activity (Rossman, Der, and Sondek 2005). As for Pard3 proteins,
567 several of these Rho GEFs contain one or several PDZ domain(s) that target most proteins to
568 complexes acting at the apical side therefore interlinking actin/actomyosin regulation with cell
569 polarity (Mack and Georgiou 2014; Ebnet and Gerke 2022). We focused on 9 PDZ-domain
570 containing Rho GEFs, all encoded by different genes in the zebrafish (***Figure 7- figure***
571 ***supplement 1***): ArhGEF11/PDZ-RhoGEF (thereafter shortened as ArhGEF11), ArhGEF12a,
572 ArhGEF12b, PRex1, PRex2, Tiam1a, Tiam1b, Tima2a, Tiam2b. We first investigated their

573 expression by Whole mount In Situ Hybridization (WISH) and found that all 9 mRNAs are
574 detected in the aorta, and for the vast majority at 30-32 and 48-50 hpf (***Figure 7- figure***
575 ***supplement 2*)*.*** Then, using qRT-PCR (***Figure 7- figure supplement 1B***), we measured and
576 compared their expression levels in the trunk region (at 35 and 48 hpf), for dt-runx1 expressing
577 embryos and controls. We found that, in comparison to controls, ArhGEF11, ArhGEF12b,
578 Tiam1b and Tiam2a are significantly reduced upon dt-runx1 expression at 48 hpf, hence being
579 positively controlled in the wild type condition, when the emergence of EHT cells is peaking.
580 This is consistent with a functional link between these Rho-GEFs, actomyosin and the control
581 of junctional dynamics during EHT progression. We finally decided to focus on ArhGEF11 for
582 the following reasons: (i) in comparison to Tiams that act on Rac1, ArhGEF11 and ArhGEF12
583 (which are close relatives and can form heterodimers (Chikumi et al. 2004)), are mostly acting
584 on RhoA which is controlling apical constriction via the RhoA-Myosin II signalling axis; as we
585 have shown previously (Lancino et al. 2018), EHT progression requires the constriction of
586 circumferential actomyosin; (ii) ArhGEF11 was shown to regulate the integrity of epithelial
587 junctions by interacting directly with the scaffolding protein ZO-1, hence connecting inter-
588 cellular adhesion with RhoA-Myosin II (Itoh et al. 2012); (iii) ArhGEF11 mediated apical
589 constriction is essential during tissue morphogenesis such as, for example, the neural tube
590 formation in which epithelial cells, submitted to mediolateral contractile forces, constrict at their
591 apical side thus triggering inward bending of the neural plate which leads to the formation of
592 the neural tube (Nishimura, Honda, and Takeichi 2012). The EHT may share features with this
593 process, i.e the anisotropic distribution of contractile forces controlling the plane of emergence;
594 (iv) mammalian ArhGEF11 exhibits alternative splicing in its C-terminal region that controls
595 tight junction stability via the regulation of RhoA activity (Lee et al. 2018) as well as cell
596 migration and invasion (Itoh et al. 2017).
597 To confirm the potential function of ArhGEF11 at the junctional interface between HE/EHT and
598 endothelial cells, we first investigated its intracellular localization. We attempted to detect the
599 full-length form upon expression of a GFP fusion protein, in the vascular system, and failed to

600 do so. We then generated a truncated form that retains the N-terminal fragment encompassing
601 the PDZ and RGS domains (see ***Figure 7 – figure supplement 3A***) fused with eGFP in its C-
602 terminus. Upon transient expression in the vascular system, we visualized its localization at
603 the interface between endothelial and hemogenic cells progressing throughout the EHT, with
604 an apparent increase in density at antero-posterior regions between adjoining EHT cells
605 (***Figure 7 - figure supplement 3B***).

606 In line with the formerly described function of a splicing variant of ArhGEF11 in controlling tight
607 junction integrity, particularly during egression of cells from the skin epithelium in the mouse
608 (Lee et al. 2018), we questioned the potential role of such variant in EHT. This variant, referred
609 to as the mesenchymal form, results from the inclusion of a peptide encoded by exon 37 or
610 exon 38 in mouse and human, respectively (Shapiro et al. 2011; Itoh et al. 2017; Lee et al.
611 2018). This insertion locates in the degenerated C-terminal region of the protein, which is
612 predicted to be relatively poorly organized in its 3D structure. Upon amplifying the full-length
613 sequence of zebrafish ArhGEF11 for investigating its localization, we cloned fragments
614 encoding – or not – for the insertion of a peptide of 25 amino-acid residues (75 base pairs
615 corresponding to exon 38). Although variable when compared with other species (see ***Figure***
616 ***7 – figure supplement 4C,*** *bottom panel*), this peptide is inserted in the same region as it is
617 for mammals and may correspond to an ArhGEF11 variant functionally equivalent and involved
618 in the regulating of junctional stability (see ***Discussion***).

619 To investigate the function of ArhGEF11 on the junctional interface between HE/EHT and
620 endothelial cells, and more specifically of the isoform containing the exon 38 encoded peptide,
621 we used both morpholino (MO) and CRISPR-based strategies. We designed a splicing MO at
622 the 3-prime exon/intron boundary of exon 38 that interferes with its inclusion in the encoding
623 mRNA (***Figure 7 - figure supplement 4A***). This MO did not trigger any deleterious effect on
624 the gross morphology of zebrafish embryos (***Figure 7 – figure supplement 4B***) and blood
625 circulation was normal in comparison to control embryos. We attempted to generate CRISPR-

626 based genomic deletion mutants of exon 38, both using Cpf1 and Cas9 enzymes and failed
627 (see ***Methods***). However, using CRISPR/Cas9, we obtained a deletion mutant triggering a
628 frame shift downstream of exon 38 and introducing a premature stop codon few amino-acid
629 residues downstream thus leading to a sequence encoding for an ArhGEF11 C-terminal
630 deleted form (see ***Methods*** and ***Figure 7- figure supplement 4C***)). Unlike the variant skipping
631 exon 38 induced by the splicing MO, expression of the CRISPR/Cas9 C-ter deletion mutant
632 triggered, around 24 hpf, a severe retardation of blood circulation initiation in approximately
633 80% of the embryos obtained from incrossing ArhGEF11$^{CRISPR\text{-}Cterdel\text{-}/+}$ heterozygous mutant
634 fishes. From 24 to 48 hpf, approximately 50% of these embryos recovered a normal blood
635 circulation (suggesting that these embryos are probably heterozygous for the mutation),
636 approximately 35% remained with a severe phenotype (characterized by a large pericardiac
637 oedema) and approximately 15% died, see ***Figure 7 – figure supplement 4D*** and ***Methods***).
638 This indicates essential functions of the C-terminal region of ArhGEF11, in agreement with
639 previously published data on the mammalian protein (Chikumi et al. 2004).

640 We then characterized more in depth the MO and CRISPR phenotypes (***Figure 7***) and
641 performed a quantitative analysis of the number and morphology of HE, EHT and adjoining
642 endothelial cells, based on confocal images and subsequent segmentation of cell contours
643 (using 2D deployment of the aortic cylinder).

644 For the morphants, we found approximately a double amount of hemogenic cells in the aortic
645 floor in comparison to controls (altogether localized on the floor and on the lateral sides of the
646 aorta, see ***Figure 7A,*** panels in **(a)** for 2D-cartographies to visualize cell shapes, with the
647 accumulation of hemogenic cells delineated in yellow for one morphant on the right and panels
648 in **(a')** for cell counts of endothelial, hemogenic and EHT cells either in the entire aorta in trunks
649 (left) or, more precisely, the aortic floor and lateral aortic side and the roof (right)); see also
650 ***Figure 7 - figure supplement 5*** for additional examples). Increase in the number of
651 hemogenic cells in morphants in comparison to controls also concerned cells oriented more

652 perpendicularly to the blood flow axis (toward the Y-axis, ***Figure 7A,*** see panels in **(a'')**),
653 consistently with variation in emergence angle, as we have shown previously (Lancino et al.
654 2018). This is accompanied by a significant reduction in the number of morphologically
655 characterized EHT cells (***Figure 7A*** and ***Figure 7 – figure supplement 5***). Similar results
656 were obtained for the CRISPR homozygous deletion mutants, particularly regarding the
657 accumulation of hemogenic cells, although with a smaller amplitude (***Figure 7B***, with the
658 panels **(b - b'')** mirroring the presentations of results obtained for morphants and internal
659 controls in ***Figure 7A***); see also ***Figure 7 - figure supplement 6*** for additional examples).
660 Consistently, a significant increase in the aortic perimeter was found, at least for the morphants
661 (***Figure 7C***). Of notice also, hemogenic cells in morphants are on average less elongated in
662 comparison to control and to the CRISPR homozygous mutants (as well as less dispersed
663 according to this parameter, compare ***Figure 7A***, panel **(a''')** with ***Figure 7B***, panel **(b'''),** with
664 visualization of the dispersion on right panels). Importantly, we observed for the morphants an
665 accumulation of a less elongated cell population standing below the median value (***Figure 7A,***
666 panel **(a''')**; to some extent, this is reproduced as well when measuring hemogenic cell area,
667 compare ***Figure 7A***, panels in **(a'''')** with ***Figure 7B***, panels in **(b'''')** for morphants and CRIPR
668 mutants, respectively). Finally, the population of small cells in the morphants are of
669 uncharacterized morphology, which means that they appear neither as EHT pol+ nor as EHT
670 pol- cells and may represent abortive emergences (***Figure 7A*** and ***Figure 7 – figure***
671 ***supplement 5,*** cells in cyan boxes).
672 Additionaly, we assessed the impact of MO interference on ArhGEF11 exon38 splicing on
673 hematopoiesis using the *Tg(CD41:eGFP)* fish line. By performing live imaging on
674 *Tg(CD41:eGFP) X Tg(Kdrl:nls-mKate2)* outcrosses (see ***Figure 7 – figure supplement 7A***
675 and ***B*** for control embryos and morphants, respectively), we quantified the number of
676 hemogenic/EHT cells in the aortic floor, based on fluorescence intensities as well as the
677 number of newly generated hematopoietic stem and progenitor cells (HSPCs, that continue to
678 express the hematopoietic eGFP reporter but stopped to express the vascular mKate2

679 reporter, ***Figure 7 – figure supplement 7C***). We show that, in agreement with our
680 morphometric analysis, an increase in the number of hemogenic/EHT cells in the aortic floor
681 in morphants in comparison to control embryos (***Figure 7 – figure supplement 7D***, with
682 median values of 14.0 and 22.5 hemogenic/EHT cells for controls and morphants,
683 respectively). Additionally, we observe, despite the high variability in both controls and
684 morphants, a relative diminution in the number of newly generated HSPC precursors (***Figure***
685 ***7 – figure supplement 7E***, with median values of 22.0 and 16.5 HSPCs for controls and
686 morphants, respectively). This is consistent with our previous results showing an accumulation
687 of HE/EHT cells in aortic floors of morphants and highlights the negative impact of this
688 accumulation on the generation of HSPCs.
689 Altogether, the morphants and CRISPR mutant phenotypes show that the progression
690 throughout EHT is significantly impaired supporting the idea that ArhGEF11 exerts important
691 functions in the process. Increase in the frequency of elongated cells for the CRISPR mutants
692 in comparison to morphants suggests that interference triggered by the C-terminal deletion of
693 ArhGEF11 is more effective at early time points. Interference with inclusion of exon 38 in
694 morphants triggers an increase in the number of hemogenic cells of smaller area and reduced
695 elongation indicating a more efficient progression throughout emergence in comparison to the
696 CRISPR mutants, albeit with impairment at later stages. This may be due to alteration in the
697 dynamics of endothelial cell intercalation which is required for emergence completion (which
698 is also compatible with the accumulation of pairs of cells that may be post-mitotic and that do
699 not spread apart because this also requires aortic cell intercalation).
700
701 **ArhGEF11/PDZ-RhoGEF and its variant containing the exon 38 encoded sequence**
702 **control junctional dynamics to support reduction of the hemogenic/endothelial**
703 **interface and cell-cell intercalation**

704 To investigate how ArhGEF11 controls the dynamic interplay between HE/EHT and endothelial
705 cells, we characterized further the MO and CRISPR phenotypes, at the junctional level. To do
706 so, we performed FRAP experiments using the *Tg(Kdrl:eGFP-Jam3b)* fish line that was
707 injected at the one cell stage with the exon 38 splicing MO, or incrossing *(Kdrl:eGFP-Jam3b x*
708 ArhGEF11$^{CRISPR\text{-}Cterdel\text{-}/+}$) heterozygous fishes to obtaining homozygous mutants and wild type
709 alleles for control siblings.

710 FRAP experiments were focused on the hemogenic (HE)/endothelial (EC) membrane
711 interface, with the support of images obtained after 2D deployments of aortic segments (***Figure***
712 ***8A***). Pools of *eGFP-Jam3b* molecules localized at bi-junctional (HE-EC, green arrows in panel
713 **A**) and at tri-junctional interfaces (HE-EC-EC (magenta arrows in panel **A**) and HE-HE-EC
714 (black arrows in panel **A**)) were bleached and subsequently imaged for FRAP analysis. In the
715 case of the MO treatment (in which case HE cells accumulate on the aortic floor, see the 2D
716 cartography ***Figure 8A***)) we measured, in comparison to controls, an increase in FRAP
717 recovery parameters for *eGFP-Jam3b* pools at the tri-junctional HE-HE-EC interface, with a
718 prominent tendency for an increase in the recovery speed at early time points (***Figure 8B,***
719 panel **(b''')**, values obtained from fluorescence intensity recoveries whose mean values are
720 represented by curves in panel **(b'')**; compare with maximum recovery amplitudes **(b'),** with
721 values obtained from the plateaus of fluorescence recovery intensities whose mean values are
722 represented in panel **(b)**). Results are different for the ArhGEF11$^{CRISPR\text{-}Cterdel+/+}$ homozygous
723 mutants for which we did not observe any obvious effect at HE-HE-EC tri-junctions (***Figure***
724 ***8C,*** with the panels **(c - c''')** mirroring the presentations of results obtained for morphants and
725 internal controls in ***Figure 8B***) but, rather, a small tendency for an increase in the mobile pool
726 at HE-EC-EC tri-junctions (that has the particularity to concern 2 endothelial cells that contact
727 the longitudinal membrane of one HE cell, see ***Figure 8A, D***).

728 Altogether and including our results presented ***Figure 7***, these results reinforce the idea that
729 ArhGEF11 and its variant encoded by exon 38 are involved in critical steps of EHT progression,

730 partly by controlling the dynamics of junctional pools at the level of tri-junctions established
731 between adjoining hemogenic and endothelial cells (see the model ***Figure 8D*** and its legend
732 for a detailed analysis of mechanistic issues). The results also suggest that the +exon38
733 peptide encoding variant is prominently involved in controlling the HE-HE-EC interface and
734 more specifically during intercalation, consistently with the accumulation, upon MO
735 interference, of EHT cells having progressed throughout the emergence but appearing to be
736 slowed down when reaching completion (cells of smaller area and less elongated, see ***Figure***
737 ***7***). Finally, ArhGEF11 is controlling RhoA and, most probably, its function in EHT progression
738 also involves actin and acto-myosin activities that are involved in the contraction of HE and
739 EHT cells (see Lancino et al. 2018; this is coupled with the consumption of longitudinal and
740 transversal membrane interfaces, see also the model ***Figure 8D*** and its legend).
741

742 ## Discussion

743 Here, we bring new insight into the cell biology and mechanics of the EHT, using live confocal
744 microscopy, RNAscope (to reveal the expression of mRNAs at the cellular resolution), and
745 genetic interference. We show that the emergence of EHT cells is more complex than
746 previously shown, with two types of EHT cells of highly different morphodynamics and apico-
747 basal polarity status. We bring evidence suggesting that these differences take root in HE
748 maturation that is primarily characterized by loss of apico-basal polarity that is then tuned by
749 the activity of the transcription factor Runx1. This leads to two types of EHT cells whose
750 respective emergence characteristics appear to rely, partly at least, on controlling the recycling
751 of junctional complexes directly linked to apico-basal polarity features (the JAMs). Also, we
752 reveal essential aspects of the interplay between HE/EHT cells and adjoining aortic endothelial
753 cells. The first is based on a potential signalling cross talk, whose molecular components
754 remain to be identified, controlling apico-basal polarity and its associated features, in space
755 (and possibly also in time, because of EHT asynchrony over the EHT time-window). The

756 second involves the control of the dynamics of junctional interfaces to reduce contacting
757 surfaces between aortic and HE/EHT cells and to promote cell-cell intercalation for the ultimate
758 release of EHT cells and proper sealing of the aortic floor.

759 **EHT morphodynamics in the zebrafish embryo in comparison to amniotes**

760 EHT cell emergence in the zebrafish embryo is relatively unique; cells extrude from the aortic
761 floor toward the sub-aortic space and not in the aortic lumen, probably because of mechanical
762 constraints on the aortic wall (discussed in Lancino et al. 2018). However, as a common feature
763 in amniotes and the zebrafish, EHT cells appear to contain large vacuolar structures (which is
764 also the case for HE cells in the zebrafish embryo, as we show); recently, this has been
765 precisely described in chick and quail embryo models (Sato et al. 2023). In amniotes, in which
766 EHT cells are round, these vacuoles appear to emanate from the abluminal membrane (facing
767 the sub-aortic space) and not from the luminal membrane. In addition, these structures
768 disappear before EHT completion, based on water chase by aquaporin activity (Sato et al.
769 2023); it has been suggested that they contribute to exert mechanical force to initiate the
770 detachment of the cell from the endothelial layer. We do not know the membranes from which
771 the pseudo-vacuolar structures that we observe originate, particularly in the HE (they may be
772 formed by transcytosis from the basal membrane, by endocytosis from the luminal membrane,
773 or coming directly from the biosynthetic pathway). However, we can exclude that they
774 contribute to the rounding of EHT pol- cells, as is the case for avians, since we do not see
775 them during EHT pol- emergence. For EHT pol+ cells, according to our results (see ***Figure 2A***
776 and our hypothetical model ***Figure 2B***), the most plausible scenario is that the apical/luminal
777 membrane is established by fusion of cytosolic vacuolar structures or redistribution of internal
778 pseudo-vacuoles connected to the luminal membrane. Subsequently, the dynamic properties
779 of the EHT pol+ cell luminal/apical membrane allows its rapid evolution after EHT completion
780 (*see* ***Figure 2 – figure supplement 1***). We propose that this is compatible with the activity of
781 aquaporins in late EHT pol+ cells and/or shortly after their release, for water chase and

782 vacuolar regression as proposed in our hypothetical model (see ***Figure 1 – figure supplement***
783 ***1B*** and the legend for details). Water chase activity would then be a common theme controlling
784 the morphology and dynamics of EHT cells throughout vertebrates, although not for the same
785 purposes.

786 **Characteristics of the HE and complexity of pre-hematopoietic stem cell emergence**

787 Heterogeneity in the identity and hematopoietic potential of cells emerging from the HE in the
788 AGM has been recently shown in co-culture systems and *in vivo* in the mouse (Ganuza et al.
789 2017; Dignum et al. 2021) and in the zebrafish model (Tian et al. 2017; Xia et al. 2023);
790 however, knowledge on the fundamental cell biological and molecular events leading to this
791 complexity is still lacking. Here, we highlight functional aspects that may significantly contribute
792 to this complexity and that take root in the cellular plasticity of the HE. We bring evidence
793 suggesting that HE cells that become competent to initiate the EHT time-window (around 28-
794 30 hpf) tune their apicobasal polarity status which endows them with the ability to support two
795 emergence processes with radically different morphodynamic characteristics; eventually, this
796 would lead to differentially fated cells, which remains to be determined.

797 While the ability of the HE to regulate its polarity features may be inherited from molecular
798 cues involved in its upstream intra-aortic specification (such as for example NOTCH (Robert-
799 Moreno et al. 2008; Gama-Norton et al. 2015; Bonkhofer et al. 2019), TGFβ (Monteiro et al.
800 2016), Gata2 (Butko et al. 2015; Daniel et al. 2019)), or any other of the more upstream factors
801 involved in hemogenic specification (Zhao et al. 2022)), our results suggest that Runx1 is
802 taking part in this regulation, consistently with its hematopoietic and EHT-inducing activity (T.
803 North et al. 1999; Kalev-Zylinska et al. 2002; Kissa and Herbomel 2010; Lancrin et al. 2012).
804 Our experiments using an interfering form of Runx1 (dt-Runx1) that produces a relatively weak
805 and subtle phenotype in comparison to morpholino treatment that prevents aortic cells to
806 convert into HE cells (Bonkhofer et al. 2019) or genetic mutation and gene knockout abrogating
807 hematopoiesis (T. E. North et al. 2009; Sood et al. 2010; Gao et al. 2018), provided the

808 opportunity to observe that, at 30 hpf (the timing point at which a majority of HE cells are still
809 paving the aortic floor), elongated HE cells appear to be maintained and to exhibit apicobasal
810 polarity, with the absence of apparent cytosolic vacuolar structures (as has been described in
811 the mouse in Runx1 interfering condition (T. North et al. 1999)); this correlates with the
812 subsequent accumulation of EHT pol+ cells. This is in favour of the idea that the polarity status
813 of HE cells has a direct incidence on the cell type that will arise, with a stronger chance to
814 evolve as an EHT pol+ cell if apical and basal domains are already determined (which is the
815 case for HE cells upon dt-Runx1 expression) and a lesser chance if these domains are not
816 established and the pool of intracellular vacuoles/pseudo-vacuoles is reduced (see the
817 hypothetical model ***Figure 2B***).

818 A key question arising from our observations is what would control the balance orienting toward
819 an EHT pol+ or an EHT pol- type of emergence. Cell division may be orienting toward EHT
820 pol- emergence type (which would also be the reason why these cells have a round-shape
821 morphology in comparison to EHT pol + cells). The frequency of EHT pol+ versus EHT pol-
822 cells that we have estimated and that is of approximately 2/1 is not incompatible with this
823 possibility since divisions take place in the HE at a relatively high frequency. Indeed, it has
824 been estimated that 50% of HE cells that constitute the aortic floor at 28 hpf will divide and will
825 undergo emergence thereafter during the 28 - 72 hpf time window (Zhao et al. 2022). However,
826 we observe that both EHT pol+ and EHT pol- cells can divide during the emergence process
827 (see also our former work Lancino et al. 2018 for EHT pol+ cells), which is followed by the full-
828 recovery of their respective morphodynamic characteristics. Hence, this excludes the
829 possibility of a short term and purely mechanical effect of cell division on emergence
830 morphodynamics. In link with cell division however, there exists the possibility that the pool of
831 large vesicular structures potentially awaiting for exocytosis in HE cells having lost their
832 apicobasal polarity may become asymmetrically inherited after division. This would endow the
833 cell remaining with the largest pool to undergo EHT pol+ emergence after exocytosis and

834 expansion of the apical/luminal membrane. Our results ***Figure 2*** would support this possibility
835 but what controls this asymmetry would remain to be established.
836 Still, regarding the control of the balance orienting toward an EHT pol+ or an EHT pol- type of
837 emergence, the intrinsic nature of the HE, i.e. its acquaintance with the aortic differentiation
838 programme (Bonkhofer et al. 2019), raises the possibility of a partial recovery of an aortic cell
839 phenotype in the case of EHT pol+ emergence, thus supporting its very unique
840 mechanobiology. Therefore, the regulation of local signalling between aortic and HE cells may
841 tune the balance toward the one or the other fate; this could be the case, for example, for
842 adjoining HE cells in comparison to isolated ones that would then receive unequal signalling
843 cues owing to the difference in homotypic versus heterotypic contacting surfaces. In this
844 scenario, NOTCH signalling which is determinant for aortic and HE specification (Gama-Norton
845 et al. 2015) may play a significant role, particularly via the ratio of the Jag1/Dll4 ligands that is
846 fundamentally involved in HE versus aortic specification (Robert-Moreno et al. 2008;
847 Bonkhofer et al. 2019).
848 Finally, we cannot totally exclude that EHT pol+ and EHT pol- cells would originate from
849 different precursors. On this line, it has been shown that the aortic wall can home a transient
850 veinous-fated progenitor cell population that will lead to the underlying vein via selective
851 sprouting from 21 to 23 hpf (Herbert et al. 2009). This option would require a massive
852 expansion of a minor fraction of the cell population remaining in the aortic floor since it is
853 expected that most of it has been moving out toward the sub-aortic region, which is not in
854 favour of this possibility. In addition, recent scRNAseq analysis of floor and roof aortic cells at
855 21 and 28 hpf has led, for both timing points, to two well defined clusters defined only by aortic
856 and hematopoietic signatures (Zhao et al. 2022).

857 **Spatially restricted control of Pard3ba mRNAs by Runx1**

858 Recent work has identified Runx1 targets in the zebrafish embryo at 29 hpf (Bonkhofer et al.
859 2019); however, the results do not point at any of the conventional apicobasal polarity

860 organizers as being direct targets although Pard3 and Pard6 mRNAs are clearly
861 downregulated in the HE in comparison to aortic roof cells. Our work now strengthens the idea
862 that understanding the mechanisms underlaying the EHT may require more than simply
863 deducing from expression of mRNAs in the HE (including the corresponding proteins), as
864 exemplified by members of the Pard3 family. Also, annotation of protein isoforms in reference
865 databases needs to be improved so as to gain precise and accurate insight on mechanistic
866 processes.
867 Our results reveal the unique sensitivity of Pard3ba mRNAs expression to Runx1 interference,
868 in comparison to the Pard3aa and ab isoforms. Also, the dt-Runx1 mutant phenotype with
869 enhanced expression of Pard3ba mRNAs in MERs highlighted and strengthened the existence
870 of these specific aortic regions in wild type animals, which could not have been so obviously
871 pointed at because of its relatively low and variable expression. Importantly, the expression of
872 Pard3ba mRNAs is mainly detected in AECs and we cannot for sure say that hemogenic/EHT
873 cells also express this mRNA because very few spots are detected and those may be at the
874 limit of the technical background (although we measured a tendency to increase their detection
875 upon dt-Runx1 expression, indicating that they may indeed be expressed in HE/EHT cells but
876 at very low levels, in wild type embryos).
877 The sensitivity of AECs on Runx1 interference is somehow unexpected since Runx1 is rather
878 expected to be involved in HE maturation as well as during EHT. This raises the possibility of
879 a direct signaling cross talk between HE/EHT cells and aortic adjoining cells. In this scenario,
880 HE/EHT cells exposed to Runx1 signaling would instruct AECs that subsequently regulate their
881 apico-basal polarity features (via Pard3ba expression); this would then feedback on HE/EHT
882 cells. Another plausible explanation is that AECs have been exposed to interference on Runx1
883 activity upstream of the EHT time-window, at a timing point at which aortic and HE cell types
884 have been sharing a common ancestor, a possibility that has been debated and reinforced in
885 the zebrafish model (Bonkhofer et al. 2019; Zhao et al. 2022). Of notice, our dt-Runx1 mutant
886 is expressed under the vascular kdrl promoter that may be active sufficiently early (Liao et al.

887 1997) to allow efficient interference with endogenous Runx1 activity on a relatively long time
888 scale; this may take place in a more or less restricted population of precursor cells, according
889 to the spatially restricted localization of Pard3ba MERs.
890 The increase of Pard3ba mRNAs detection, upon dt-Runx1 mutant expression, suggests that
891 endogenous Runx1 negatively controls this specific mRNA in wild type embryos. This is
892 consistent with our results since there are two cell types/stages during the EHT process for
893 which we observe a negative regulation of apico-basal polarity, i.e the maturing HE and EHT
894 pol- cells, as visualized upon expression of eGFP-podxl2 and mKate2-podxl2 (the fluorescent
895 fusion proteins are partitioned equally between the luminal/apical and the basal membranes).
896 Altogether, this reinforces the idea that Runx1 negatively controls apico-basal polarity in HE
897 and EHT pol- cells; at least in part, it does so via the Pard3ba isoform that we hypothesize acts
898 as a tuner, consistently with the high sensibility of its mRNA expression to Runx1 activity and
899 the recurrent variability in expression that we are measuring. Owing to the apparent
900 stochasticity of the EHT process in time and space (emergence takes place asynchronously
901 during the time window of the EHT that ranges from approximately 28 to 72 hpf and proceeds
902 from place to place, all along the floor of the dorsal aorta), this may be what contributes to the
903 experimental variability that we are measuring at a given time using qRT-PCR and RNAscope
904 (for all determinations of Pard3ba mRNAs in comparison to other isoforms; of notice, variations
905 are even larger for the dt-Runx1 mutants, which is consistent with the high sensitivity to dt-
906 Runx1 expression levels that are expected to be relatively different from one transgenic
907 embryo to the other).
908 Altogether, our results are consistent with the hypothesis that the variability in expression of
909 Pard3ba mRNAs reflects the response to intrinsic fluctuations of the system over time and
910 space and reinforce the idea that these conditions, mediated by Runx1 and environmental
911 constraints imposed by the blood flow, tune apico-basal polarity. This tuning scenario would
912 also explain the specific case of EHT pol+ cells that would then proceed as such upon
913 exposition to positive apico-basal signaling when Runx1 activity is decreased, consistently with

914 the tendency to accumulate EHT pol+ cells upon expression of our dt-Runx1 mutant.
915 Unfortunately and presently, we cannot show a spatial proximity between EHT pol + cells and
916 Pard3ba MERs *in situ* (or the opposite for EHT pol- cells) owing to technical limitations with
917 fixed embryos that do not allow the maintenance of EHT cell shapes. Resolving this issue in
918 the future will be very informative, also to place cellular morphodynamics and gene expression
919 regulation throughout the EHT, with spatial and temporal resolution.

920 **The complexity of pre-HSC emergence and heterogeneity of hematopoietic stem cell**
921 **and progenitor populations**

922 Currently, we do not know what would be the features that would endow the two cell types to
923 behave differently after their release. Since post-EHT cells have to migrate in transient
924 developmental niches (i.e the CHT, the thymus, the pronephric region), these features may
925 provide them with more or less ability to migrate in the sub-aortic space and pass throughout
926 the wall of the underlying vein to conquest more distant niches (Murayama et al. 2006), or to
927 remain in a local AGM niche and be exposed to specific signalling there, in the proximity to the
928 aorta as it is the case for hematopoietic clusters in mammals and avians (Ciau-Uitz et al. 2014;
929 Jaffredo and Yvernogeau 2014). Beside their potential differences in colonizing different niches
930 which would impact on their subsequent fate, these cells may also contribute to more or less
931 transient waves of hematopoietic stem cells and progenitors that would be specific to the
932 developmental period such as, for example, a restricted sub-set of T-lymphocytes that was
933 described before (Tian et al. 2017). In the specific case of the Tian et al. work, the AGM was
934 shown to produces transient T-lymphocytes proposed to be independent of long-lived HSCs
935 according to a gradient that increases from the anterior to the posterior part of the trunk region,
936 as well as from the aorta in the tail (the posterior blood island in the tail region that was
937 proposed to give rise to hematopoietic precursors related to mammalian erythro-myeloid
938 progenitors, (Bertrand et al. 2007)). Since the EHT pol+ and EHT pol- cells that we describe in
939 our work are equally produced from the aorta in the trunk and in the tail regions (thus

940 irrespective of the antero-posterior axis of the aorta), the one or the other of the two EHT types
941 most probably does not directly relate to the first wave of T-lymphopoiesis arising from the
942 aortic endothelium described in Tian et al. 2017.

943 **The cell biology behind emergence control and morphodynamics**

944 The intrinsic capacity of the HE, that we show here to be able to support two highly distinct
945 emergence processes, in the zebrafish embryo, is very unique. Indeed, not only are they taking
946 place contemporarily, but also can the two cell types proceed throughout emergence at a
947 distance shorter than 50 μm, which accommodates the intercalation of a single adjoining
948 endothelial cell. This may reflect the remarkable properties of the vascular system that needs
949 to allow cellular extrusion and transmigration. The latter is particularly relevant in the context
950 of developmental hematopoiesis since hematopoietic precursors that travel via blood
951 circulation need to pass throughout the aortic wall to conquest their distant niches.

952 In the present work, we provide some of the mechanistic insights into the specificities of the
953 two emergence types and that rely on two fundamental aspects of cellular biology, i.e
954 apicobasal polarity establishment and junctional mobility. The establishment and maintenance
955 of apicobasal polarity in a cell extruding from its environment, as is the case for EHT pol+ cells,
956 is at odds with the fundamental mechanisms of cell extrusion irrespective of the context into
957 which the process is taking place (Nieto et al. 2016; Gudipaty and Rosenblatt 2017; Pei et al.
958 2019; Staneva and Levayer 2023); this places the emergence of EHT pol+ cells as an extreme
959 case of extrusion and it is somehow unexpected to observe this type of emergence when the
960 aortic wall can extrude EHT pol- cells that appear to emerge contemporarily, apparently
961 according to a more conventional mode. During the EHT time-window, Runx1 is directly
962 controlling the emergence programme by regulating Rho-dependent cytoskeletal functions in
963 HE cells derived from mouse ES lines (Lie-A-Ling et al. 2014) and inducing the expression of
964 Gfi1ab in the zebrafish (Bonkhofer et al. 2019) that belongs to the family of transcriptional
965 repressors of the arterial programme expressed in the HE (Gfi1 and Gfi1b in the mouse,

966 (Lancrin et al. 2012)). This programme downregulates key molecules involved in the
967 maintenance of the aortic endothelium among which Cdh5 (VE-Cadh) and the downregulation
968 of cadherins is a hallmark of extrusion. Thus, for EHT cells, and particularly EHT pol+ cells,
969 downregulation of VE-Cadh should be compensated by other mechanisms that allow for the
970 maintenance of aortic integrity. In this context of adhesion downregulation, the JAMs (that are
971 expressed endogenously in the vascular system and that were used in this study) appear to
972 be a well-suited substitute. As part of tight junction complexes, they can strengthen adhesion
973 and, in addition, since they are also involved in cell migration (in particular leukocyte trans-
974 endothelial migration, see (Ebnet 2017)), they could in theory support the extrusion of EHT
975 pol- cells that do so according to a seemingly migration-type emergence mode (inferred from
976 our time-lapse sequences) more or less related to trans-endothelial migration. In the case of
977 EHT pol+ cells, we propose that JAMs may significantly contribute to the re-establishment of
978 apicobasal polarity and to the strengthening of adhesion while EHT pol+ cells should undergo
979 strong mechanical tension (owing to cellular bending). Interestingly, Jam3b appears to be a
980 direct and positively regulated target of Runx1 (Bonkhofer et al. 2019), which is supporting its
981 aforementioned potential functions during EHT.
982 In regard to the different modes of junctional recycling between aortic and either EHT pol+ or
983 EHT pol- cells for which be bring evidence using FRAP, we hypothesize that differences take
984 root in the regulation of cell polarity features, such as for example the organization of an apical
985 endosome in the case of EHT pol+ cells (which may be why recycling of eGFP-Jam molecules
986 appears to be faster in EHT pol+ cells in comparison to EHT pol- cells, in relation to the
987 recycling pathways undertaken by JAM molecules). In addition, since JAMs interact with Pard3
988 (Ebnet et al. 2003) this recycling, that would provide renewed JAM/Pard3 complexes at
989 membrane junctions and sustained activation of the Pard3/Pard6/aPKC complex (Ebnet 2017),
990 may contribute to the maintenance/reinforcement of EHT pol+ cell polarity throughout the
991 entire emergence process. Also, the regime of recycling may be regulated by an adjacent aortic
992 endothelial cell that expresses Pard3ba and that controls trans-cellular JAMs pairing via

993 signalling involving apico-basal polarity features. Finally, this turnover may be adapted to the
994 mechanical tensions EHT pol+ cells are exposed to, in comparison to EHT pol- cells, owing to
995 their specific morphodynamic features (ex: cellular bending); these tensions may be sensed
996 by tri-cellular junctions which would be preferential sites for the renewal of junctional
997 components whose half-life is reduced owing to submission to mechanical forces.

998 **The cell biology behind emergence control and mechanics: the function of**
999 **ArhGEF11/PDZ-RhoGEF in the dynamic interface between aortic and HE cells**

1000 Finally, regarding inter-cellular junctions and the control of their dynamics all along the EHT
1001 process, we also addressed the dynamic interface between aortic and HE cells. As for EHT
1002 cells, we focused more specifically on tri-junctional interfaces that have been proposed to
1003 sense tension and transmit the information to other types of junctional complexes (Bosveld,
1004 Wang, and Bellaïche 2018); in the EHT context, the contracting hemogenic endothelium is
1005 additionally exposed to high mechanical tension owing to wall sheer stress imposed by the
1006 blood flow and that was proposed to regulate emergence efficiency (Lundin et al. 2020;
1007 Campinho et al. 2020; Chalin et al. 2021). In our work, we highlight one essential aspect of
1008 controlling junctional recycling which is during cell-cell intercalation which concerns either
1009 contacting HE cells lying on the aortic floor or HE/EHT cells after cytokinesis (as mentioned
1010 before, cell division is rather frequent during the EHT time window (Zhao et al. 2022)). In this
1011 context, we addressed the function of ArhGEF11/PDZ-RhoGEF which provides a functional
1012 link between cell polarity (with its PDZ-binding motif and its RGS domain that couples to G-
1013 protein coupled receptor signalling to regulate planar cell polarity (Nishimura, Honda, and
1014 Takeichi 2012)), cell adhesion (it binds to the tight junction associated regulatory protein ZO-
1015 1, (Itoh et al. 2012)), and cytoskeletal regulation/contraction (Itoh et al. 2012; Itoh 2013), all
1016 three essential mechanistic components of morphogenetic movements and tissue remodelling.
1017 Since morphodynamic events leading to cell extrusion and to the control of cell migration do
1018 not only rely on the regulation of mRNAs levels but also on alternative splicing (Pradella et al.

1019 2017) our interest for investigating the function of ArhGEF11 in EHT was raised by the fact that
1020 the protein undergoes changes in its biological properties via the alternative splicing of a small
1021 exon which leads to a modification of its C-terminus. We identified a splicing event in this region
1022 (concerning exon 38) for a potential zebrafish isoform ortholog. However, the precise function
1023 of this variant for the zebrafish protein, that was shown in the case of the mammalian isoform
1024 to induce cell migration and motility (Itoh et al. 2017) and to bind to the Pak4 kinase thus
1025 leading to the subsequent destabilization of tight junction complexes via loss of RhoA activation
1026 (Lee et al. 2018), remains to be established. On this line, our results consistently indicate that
1027 preventing exon 38 insertion interferes with EHT progression (as well as deleting the C-
1028 terminus of the protein as shown with our CRISPR mutant) and appears to impair intercalation
1029 of aortic cells between adjoining HE cells. Hence, the +exon 38 isoform, by regulating the
1030 dynamic interplay between HE and endothelial cells, would favour one of the essential steps
1031 of the EHT process leading to its completion and requiring the complete isolation of EHT cells
1032 to ensure the ultimate sealing of the aortic floor (see our former work (Lancino et al. 2018)). It
1033 remains to be established, as our measurements indicate, why the ArhGEF11 +exon 38
1034 isoform appears to slow down junctional recycling which is counterintuitive with increasing the
1035 HE/endothelial dynamic interface. However, upon interference, we have been following Jam3b
1036 recycling which is only a sub-population of tight junction components that should be at play in
1037 the system. Finally, the EHT process on its whole may be submitted to a complex regime of
1038 alternating contraction and stabilization phases as we have shown previously in the context of
1039 EHT pol+ emergence and that may reflect the necessity to adapt to mechanical constraints
1040 imposed by the environment as well as the rearrangements of the HE/EHT/aortic cellular
1041 interface (Lancino et al. 2018). In this context, back and forth regulatory mechanisms,
1042 particularly involved in the control of the RhoA-Myosin II signalling axis partially regulated by
1043 ArhGEF11, may locally and at specific timing points change the turnover of junctional
1044 molecules, thus blurring the correlation between gross phenotype (here the organization of the

1045 HE/aortic interface) and very local and dynamic molecular events (for a complement to the
1046 discussion, see also the legend of the model presented ***Figure 8C***).

1047 Overall, our work highlights the complexity of pre-hematopoietic stem cell emergence as well
1048 as some of the essential molecular and mechanistic aspects involved, at the interface with
1049 aortic endothelial neighbours. We show that the aorta, in the zebrafish embryo, produces two
1050 fundamentally different types of EHT cells and propose that this results from specific functional
1051 features of the HE regulated by the transcription factor Runx1. Among these features, apico-
1052 basal polarity and its regulation appear to be essential for the spatial and temporal control of
1053 EHT cell emergence which is an asynchronous process. This would support the production of
1054 cell types potentially endowed with different cell fate potential, subsequently reinforced by the
1055 type of niche into which these cells will establish homing. It now remains to be established if
1056 the different cell types that we describe are indeed leading to cells that will eventually hold
1057 specific hematopoietic fate and properties.

1058 # Materials and Methods

1059 ## Key Resources Table

1060 For the exhaustive list of all primers, see Materials and Methods - Supplementary Table.

Reagent type (species) or resource	Designation	Source or reference	Identifiers	Additional information
strain, strain background (zebrafish *Danio rerio*)	AB	Zebrafish International Resource Center (ZIRC)	ZFIN: ZDB-GENO-960809–7	
strain, strain background (zebrafish *Danio rerio*)	Tg(kdrl:HsHRAS -mCherry): s916Tg	(Chi et al. 2008)	ZFIN ID: ZDB-ALT-090506–2	referred to as Tg(kdrl:Ras-mCherry)
strain, strain background (zebrafish *Danio rerio*)	Tg(6.0itga2b:EGFP)	(Lin et al. 2005)	ZFIN ID: ZDB-ALT-051223–4	referred to as Tg(CD41:eGFP)
strain, strain background (zebrafish *Danio rerio*)	Tg(kdrl:eGFP)	(Jin et al. 2005)	ZFIN ID: ZDB-ALT-050916–14	
strain, strain background (zebrafish *Danio rerio*)	Tg(kdrl:nls-mKate2)	N/A	N/A	
strain, strain background (zebrafish *Danio rerio*)	Tg(kdrl:Gal4;UAS:RFP)	N/A	N/A	
strain, strain background (zebrafish *Danio rerio*)	Tg(kdrl:Gal4;UAS:RFP;4xNR:eGFP-Podxl2)	This paper	N/A	
strain, strain background (zebrafish *Danio rerio*)	Tg(kdrl:mKate2-Podxl2)	This paper	N/A	
strain, strain background (zebrafish *Danio rerio*)	Tg(kdrl:eGFP-Jam2a)	This paper	N/A	
strain, strain background (zebrafish *Danio rerio*)	Tg(kdrl:eGFP-Jam3b)	This paper	N/A	
strain, strain background (zebrafish *Danio rerio*)	Tg(kdrl:Gal4;UAS:RFP;4xNR:dt-runx1-eGFP)	This paper	N/A	
strain, strain background (zebrafish *Danio rerio*)	Tg(ArhGEF11$^{CRISPR\text{-}Cterdel\text{-}/+}$)	This paper	N/A	

Reagent type (species) or resource	Designation	Source or reference	Identifiers	Additional information
recombinant DNA reagent	pG1-flk1-MCS-tol2	(Jin et al. 2005)	N/A	
recombinant DNA reagent	pEGFP-C1	Clontech	N/A	
recombinant DNA reagent	Transposase pCS-zT2TP	(Suster et al. 2011)	N/A	
recombinant DNA reagent	pmKate2-f-mem	Evrogen	Cat# FP186	
antibody	goat anti-rabbit Alexa Fluor 488	Invitrogen	Cat# A11070	1/400
antibody	rabbit anti-GFP	MBL	Cat# 598	1/300
antibody	mouse anti-HA	Sigma	Cat# 12ca5	1/50
antibody	goat anti-mouse HRP-conjugated	Thermo Fisher Scientific	Cat# G-21040	1/300
sequence-based reagent	Morpholino sih	(Sehnert et al. 2002)	ZDB-MRPHLNO-060317-4	CATGTTTGCTCTGATCTGACACGCA
sequence-based reagent	Morpholino ArhGEF11 exon 38	This paper	N/A	GAAATAAATGAAGCCCCACCTCCGT
sequence-based reagent	Oligo for CRISPR: Alt-R® CRISPR-Cas12a (Cpf1) crRNAs -1	This paper	N/A	TATCACACACACATCACCTTCTA
sequence-based reagent	Oligo for CRISPR: Alt-R® CRISPR-Cas12a (Cpf1) crRNAs -2	This paper	N/A	TTTCTCAGCGCTCCTGACAGATG
sequence-based reagent	Oligo for CRISPR: Alt-R® CRISPR-Cas9 crRNAs	This paper	N/A	AGCCAATCGTCTGAGGACGG
sequence-based reagent	Oligo for CRISPR: Alt-R® tracrRNA	IDT	Cat# 1072532	
sequence-based reagent	Oligo for WISH: RNAscope™ Probe-Dr-myb-C3	ACD-Biotechne	Cat No. 558291-C3	Cat No. 558291-C2
sequence-based reagent	Oligo for WISH: RNAscope™ Probe-Dr-pard3ab-C3	ACD-Biotechne	Cat No. 1282521-C3	
sequence-based reagent	Oligo for WISH: RNAscope™ Probe-Dr-pard3ba-C2	ACD-Biotechne	Cat No. 1309581-C2	
sequence-based reagent	Oligo for WISH: RNAscope™ Probe-Dr-pard3aa-C2	ACD-Biotechne	Cat No. 1305321-C2	
software, algorithm	Imaris	Oxford Instruments	https://imaris.oxinst.com/	v10.1.0
software, algorithm	CRISPRscan	(Moreno-Mateos et al. 2015)		N/A

Reagent type (species) or resource	Designation	Source or reference	Identifiers	Additional information
software, algorithm	Zen Pro2 software	Zeiss	https://www.zeiss.com/microscopy/en/products/software/zeiss-zen.html	N/A
software, algorithm	QUANTSTUDIO™ DESIGN & ANALYSIS 2	Thermofisher	https://apps.thermofisher.com/apps/da2/	N/A
software, algorithm	MetaMorph software	Molecular Devices	https://www.moleculardevices.com/products/cellular-imaging-systems/acquisition-and-analysis-software/metamorph-microscopy	N/A
software, algorithm	Acquisition-Imaging analysis-LAS X	Leica	http://www.leica-microsystems.com	N/A
software, algorithm	Image Analysis-Fiji	NIH	https://imagej.net/Fiji	N/A
software, algorithm	Image Analysis Icy	(De Chaumont et al. 2012)	http://icy.bioimageanalysis.org/	N/A
software, algorithm	Image Analysis TubeSkinner plugin for Icy	(Lancino et al. 2018)	https://icy.bioimageanalysis.org/plugin/tubeskinner/	N/A
software, algorithm	Figures-Illustrator CC 2017.1.1	Adobe	http://www.adobe.com/cn/	N/A
software, algorithm	Active contour plugin	(Dufour et al. 2011)	https://icy.bioimageanalysis.org/plugin/active-contours/	N/A
software, algorithm	NIS software	Nikon	https://www.microscope.healthcare.nikon.com/en_EU/products/software/nis-elements	N/A
software, algorithm	Rstudio	RStudio Team (2020)	http://www.rstudio.com/}	N/A
software, algorithm	ggplot2	(Wickham 2016)	https://ggplot2.tidyverse.org.	N/A
software, algorithm	readr	(Wickham, Hester, and Bryan 2022)	https://github.com/tidyverse/readr	N/A
software, algorithm	cowplot	(Wilke 2020)	https://wilkelab.org/cowplot/	N/A
software, algorithm	dplyr	(Wickham et al. 2023)	https://github.com/tidyverse/dplyr	N/A
software, algorithm	wesanderson	(Ram and Wickham 2018)	https://github.com/karthik/wesanderson	N/A

Reagent type (species) or resource	Designation	Source or reference	Identifiers	Additional information
software, algorithm	matrixStats	(Bengtsson et al. 2023) 09/02/2024 14:57:00	https://github.com/HenrikBengtsson/matrixStats	N/A
software, algorithm	stringr	(Wickham 2022)	https://github.com/tidyverse/stringr	N/A
software, algorithm	ggsci	(Xiao 2018)	https://github.com/nanxstats/ggsci.	N/A
software, algorithm	ggpubr	(Kassambara 2020)	https://rpkgs.datanovia.com/ggpubr/	N/A
software, algorithm	ggstatsplot	(Patil 2022)	https://indrajeetpatil.github.io/ggstatsplot/index.html	N/A
software, algorithm	ggbeeswarm	(Clarke and Sherrill-Mix 2017)	https://github.com/eclarke/ggbeeswarm	N/A
software, algorithm	DT	(Xie, Cheng, and Tan 2022)	https://github.com/rstudio/DT	N/A
software, algorithm	SciViews	(Grosjean 2019)	https://www.sciviews.org/SciViews/	N/A
software, algorithm	nls.multstart	(Padfield and Matheson 2020)	https://github.com/padpadpadpad/nls.multstart	N/A

Contact for reagent and resource sharing

Further information and requests for resources and reagents should be directed to and will be fulfilled by the corresponding Author, Anne A. Schmidt (anne.schmidt@pasteur.fr).

Zebrafish husbandry

Zebrafish (Danio rerio) of the AB background and transgenic fish carrying the following transgenes *Tg(kdrl:ras-mCherry)* (Chi et al. 2008); *Tg(kdrl:nls-mKate2)*; *Tg(kdrl:Gal4;UAS:RFP); Tg(kdrl:eGFP) (Jin et al. 2005); Tg(CD41:eGFP) (Lin et al. 2005); and the fish lines generated in this study: Tg(kdrl:Gal4;UAS:RFP;4xNR:eGFP-podxl2); Tg(kdrl:mKate2-Podxl2); Tg(kdrl:eGFP-Jam2a); Tg(kdrl:eGFP-Jam3b)*; *Tg(kdrl:Gal4;UAS:RFP;4xNR:dt-runx1-eGFP); Tg(ArhGEF11$^{CRISPR\text{-}Cterdel\text{-}/+}$)* were raised and staged as previously described (Kimmel et al. 1995). Adult fish lines were maintained on a 14

1074 hr light/10-hr dark cycle. Embryos were collected and raised at either 28.5 or 24°C in N-
1075 Phenylthiourea (PTU, Sigma Aldrich, Cat# P7629)/Volvic source water (0.003% final) to
1076 prevent pigmentation complemented with 280 μg/L methylene blue (Sigma Aldrich, Cat#
1077 M4159). Embryos used for imaging, extracting mRNA, or for WISH ranged from developmental
1078 stages 28-to-60 hpf and larvae used for imaging were of 3-5 dpf, precluding sex determination
1079 of the animals. The fish maintenance at the Pasteur Institute follows the regulations of the
1080 2010/63 UE European directives and is supervised by the veterinarian office of Myriam Mattei.

1081 **mRNA extraction and cDNA synthesis**

1082 Total RNA was extracted from whole 48 hpf embryos for cDNA cloning or from pooled trunks
1083 at the desired developmental stages (30-32 hpf, 48-50 hpf time windows for qRT-PCR
1084 experiments) (~30 individuals per tube). Briefly, embryos were anesthetized using balneation
1085 in embryo medium supplemented with tricaine methanesulfonate (MS-222, Sigma-Aldrich Cat#
1086 A5040), at a final concentration of 160 μg/ml. RNA was extracted via organic extraction using
1087 TRIzol reagent (Invitrogen Cat# 15596026) according to the manufacturer's guideline. gDNA
1088 contaminant was removed using TURBO™ DNase (Invitrogen Cat# AM2238) treatment
1089 according to the manufacturer's guideline. Total RNA was stored at -80°C. Reverse
1090 transcription of mRNA was performed using SuperScriptIV (Invitrogen Cat# 18090010) with
1091 OligodT primer. cDNA samples were stored at -20°C until further processing (for quantitative
1092 real-time PCR, PCR, cloning and sequencing).

1093 **Transient and stable transgenesis**

1094 The *kdrl* promoter (*flk*) (Jin et al. 2005) was used to drive endothelial expression of mKate2-
1095 podxl2, eGFP-Jam2a and eGFP-Jam3b, with eGFP (Clontech) and mKate2 (Evrogen) cDNAs
1096 amplified using overlapping primers for Gibson cloning. eGFP-podxl2, ArhGEF11(PDZ-PRD-
1097 RGS-eGFP) and dt-runx1-eGFP were amplified for cloning into a pG1-4XNR vector (built from
1098 the 4XNR (non-repetitive) 4X UAS sequence less susceptible to methylation than the 14X UAS

1099 described in (Akitake et al. 2011)). For the sequence of all the designed cloning primers, see
1100 the Key Resources Table.

1101 Podocalyxin-like 2 (Podxl2), ArhGEF11/PDZ-RhoGEF, JAM2a and JAM3b full length
1102 sequences were amplified from pools of 48 hpf whole embryo cDNA (see before for mRNA
1103 extraction and cDNA synthesis methodologies). All constructs generated in this study were
1104 obtained using the Gibson assembly assay (NEB, Cat # E2611S).

1105 For eGFP-Jam2a and eGFP-Jam3b cloning, we used the JAM2a signaling peptide sequence
1106 (included in the 5-prime amplification primers and encoding for the signal peptide:
1107 mlvcvsllilihsvpvspvtvssr) and, for both constructs, the eGFP sequence was inserted in frame
1108 upstream of the sequence encoding for the transmembrane domain; for the eGFP-Jam2a
1109 construct, the eGFP was inserted upstream of amino-acid D221 (DLNVAA) of the NCBI
1110 Reference Sequence: NP_001091734.1; for the eGFP-Jam3b construct, the eGFP was
1111 inserted upstream of amino-acid D243 (DINIAG) of the NCBI Reference Sequence:
1112 NP_001076332.2. For transient ubiquitous and inducible expression, the eGFP-Jam2a and
1113 eGFP-Jam3b fusion constructs were inserted into a KpnI pre-digested pG1 plasmid containing
1114 tol2 sites and the HSP70-4 promoter. For stable transgenesis using the *kdrl* (*flk1*) promoter,
1115 constructs cloned into the pG1-HSP70 plasmids were extracted using XhoI/NotI restriction
1116 enzymes and inserted into the XhoI/NotI pre-digested pG1-flk1 vector using DNA T4 ligation
1117 (NEB, Cat # M0202S).

1118 For the Podxl2 N-ter deletion mutant that has been used for establishing stable *Tg* fish lines,
1119 the cDNA encoding for the peptide sequence starting with amino-acid G341 (GGTEYL;
1120 fragment 341-587) of the NCBI Reference Sequence: XP_692207.6 was fused with either
1121 eGFP or mKate2 cDNAs. The sequence encoding for the signal peptide of the human CD8
1122 (malpvtalllplalllhaarpsqfrvs) was introduced upstream (5-prime) of the eGFP or mKate2
1123 sequences (included in the 5-prime primers designed for the Gibson cloning strategy). For the
1124 construct designed to obtain the *Tg(kdrl:Gal4;UAS:RFP;4xNR:eGFP-podxl2)* fish line, 2

1125 overlapping fragments were amplified for cloning into a pG1-tol2_4xNR vector after digestion
1126 with NcoI, with the following couples of primers: 4XNR_CD8-eGFP_fw and
1127 delPodxl2_eGFP_rev; delPodxl2_fw and Podxl2_pG1-4XNR_rev. For the construct designed
1128 to obtain the *Tg(kdrl:mKate2-Podxl2)* fish line 2 overlapping fragments were amplified for
1129 cloning into a pG1-flk1 vector after digestion with EcoR1, with the following couples of primers:
1130 pG1-flk1_CD8_mKate2_fw and delPodxL2-mKate2_rev; mKate2-delPodxL2_fw and
1131 Podxl2_PG1-flk1_rev.
1132 For the ArhGEF11(PDZ-PRD-RGS-eGFP) construct, the cDNA encoding for the peptide
1133 ending upstream of the DH domain at Valine 709 of the amino-acid sequence (GenBank:
1134 AY295347.1; PALDEDV; fragment 1-709) was fused upstream of the sequence encoding for
1135 eGFP, for expression using the pG1-4xNR vector. The cDNA was amplified using the
1136 GB_4xUAS-gef11_fw; GB_eGFP-RGS_rev couple of primers.
1137 For the construct designed to obtain the *Tg(kdrl:Gal4;UAS:RFP;4xNR:dt-runx1-eGFP)* fish
1138 line, the Runx1 sequence amplified omits the ATG (replaced by an nls) and ends downstream
1139 of the Runt domain (ending at amino-acid sequence PAHSQIP). The construct allows for the
1140 expression of the dt-runx1 protein under the control of the 4xNR driver using the same strategy
1141 as for the above PodxL2 constructs. The dt-runx1 cDNA construct was amplified from the
1142 zebrafish Runx1 cDNA sequence (Kalev-Zylinska et al. 2002) using the couple of primers GB-
1143 4xnr-nlsRunx1_fw; GB-eGFP-T2A-2xHA-delRunx1_rev. The sequence of these primers each
1144 allowed for the introduction, in the protein sequence, of a nls (encoded by the fw primer) and
1145 of a 2xHA-T2A peptide (encoded by the rev primer that overlaps with the 5-prime sequence of
1146 eGFP).
1147 For all constructs, cloning reactions were used to transform NEB 5-alpha Competent E. coli
1148 (NEB, Cat # C2987) and resistant clones then used for miniprep plasmid preparations
1149 (Nucleospin plasmid, Macherey-Nagel, Cat # 740588.50), followed by sequencing. Plasmid
1150 DNA from clones containing correct insertions where then used to transform E. coli TOP10
1151 competent cells (Invitrogen, Cat # C404010) and purified using the endotoxin free NucleoBond

1152 Xtra Midi kit (Macherey Nagel, Cat# 740420.10). Transgenesis was then performed by co-
1153 injecting 1 nl of plasmid (at 25 ng/μl) mixed with tol2 transposase mRNA (at 25 ng/μl)
1154 transcribed from linearized pCS-zT2TP plasmid using the mMESSAGE mMACHINE SP6 kit
1155 (Ambion, Cat# AM1340). For stable transgenesis, embryos were screened for fluorescence
1156 between 24 hpf and 48 hpf and raised to adulthood. Founders with germline integration were
1157 then isolated by screening for fluorescence after outcrossing with AB adults and for
1158 establishment of the F1 generation.
1159

1160 **CRISPR methodology and GEF11 mutant transgenic line screening**

1161 *CRISPR/Cas9 mutagenesis and isolation of founders*

1162 A sgRNA was designed against the splice donor site at the end of exon 38 with the aim to
1163 interfere with the production of the splicing variant including its encoding sequence, using the
1164 CRISPRscan web tool (Moreno-Mateos et al. 2015). The sgRNA was obtained by annealing
1165 for 5 min at 95°C equal volumes of 100μM specific Alt-R® crRNAs (IDT, Cat# sequence:
1166 AGCCAATCGTCTGAGGACGG) with 100μM Alt-R® generic tracrRNA (IDT, Cat# 1072532).
1167 Cas9 Nuclease Reaction Buffer (NEB Cat# B0386A) was added to obtain a final 45μM sgRNA
1168 stock solution. For the generation of the sgRNAs–Cas9 complex, a mix containing 18μM
1169 sgRNA and 12μM Cas9 protein (EnGen™ Spy Cas9-NLS S. pyogenes, NEB Cat# M0646T)
1170 was incubated for 10 min at room temperature. For mutagenesis, 1 nl of the sgRNA-Cas9
1171 complex was injected into one-cell stage embryos, that were subsequently raised until 48 hpf.
1172 Bulk genomic DNA (gDNA) was extracted from 60 injected and 60 non-injected control
1173 embryos. gDNA extraction proceeded as follows: pooled samples were incubated for 3 hrs at
1174 55°C in lysis buffer (100mM NaCl, 20mM Tris-HCl pH 8, 25mM EDTA, 0.5% SDS and 2 μg/μl
1175 proteinase K), purified using phenol:chloroform. Precipitation was done in 0.1 volume of 3M
1176 NaAc and 2.5 volume of 100% ethanol for 20 min at -20°C. Samples were centrifuged for 30
1177 min at 4°C before washing with 70% ethanol and resuspension in water. gDNA was used for
1178 PCR, using DNA polymerase Platinum™ SuperFi™ (Invitrogen Cat# 12351010) and the

1179 SM31-SM32bis couple of primers (TTTCACTTTCTCTCTGCCTCTTACA;
1180 AACTCTGTCCAGATGATTGAGGAGC) flanking the targeted region. PCR products were run
1181 on gel electrophoresis before gel extraction of bands of interest (with sizes corresponding to
1182 either a wild-type allele or a deleted allele) (Nucleospin gel and PCR clean-up, Macherey-
1183 Nagel Cat# 740609.50). Fragments were cloned into blunt-end TOPO vector (Invitrogen Cat#
1184 45024), transformed into E. coli TOP10 competent cells and grown on selective medium. 12
1185 colonies for each PCR product were sent for sequencing. Mutant sequences contained either
1186 a 7 nucleotides deletion, or a mix of 1,4 or 7 nucleotides deletions located at the same site (at
1187 the end of exon 38, see ***Figure 7 - figure supplement 4A*** for the 7 nucleotides deletion),
1188 attesting of the proper functioning of our guide.

1189 A stable homogeneous mutant line was generated by injecting the sgRNA:Cas9 complex into
1190 one-cell stage *Tg(kdrl:Gal4;UAS:RFP)* embryos similarly to what was described above. 100
1191 embryos were raised until adulthood. Adult founders were identified by crossing adult F0 with
1192 AB fishes, and single embryo genotyping was performed on their progeny (10 embryos per
1193 adult fish). Briefly, single embryos were incubated in 40*µ*l 25mM NaOH 0.2mM EDTA and
1194 heated for 10 min at 95°C, before cooling for 10 min at 4°C and addition of 40*µ*l 40mM Tris-
1195 HCl pH5 to stop the reaction. PCR was performed using 5*µ*l of template and specific primers
1196 (couple SM31-SM34 –TTTCACTTTCTCTCTGCCTCTTACA;
1197 ATAAATGAAGCCCCACCTCCGTCC – for wild-type (WT) allele and couple SM31-SM40 –
1198 TTTCACTTTCTCTCTGCCTCTTACA; ATGAAGCCCCACCTCAGACGATTGGC– for mutant
1199 allele). Presence of WT or mutant allele for each single embryo was assessed by the
1200 presence/absence of amplification band on gel electrophoresis. Four F0 founders were
1201 isolated, that had a transmission rate in the germline ranging from 20% to 80%. Progeny of the
1202 F0 founders and subsequent generations were raised separately until adulthood, and
1203 genotyped. After complete anesthesia (in fish water supplemented with 160*µ*g/ml tricaine
1204 methanesulfonate), a small tissue sample was collected from the caudal fin, placed into DNA

1205 extraction buffer (10mM Tris pH8.2, 10mM EDTA, 200mMNaCl, 0.5% SDS, 200μg/ml
1206 proteinase K) and incubated 3 hrs at 50°C. DNA precipitation and resuspension was performed
1207 as described above. 7μL gDNA was used as template for PCR amplification using the primer
1208 couple SM31-SM32bis. Sequenced PCR products showed that all founders harbored the same
1209 7 nucleotides deletion (see ***Figure 7 - figure supplement 4A***). All experiments relative to
1210 ***Figure 7*** *and* ***Figure 8*** were performed using the progenies of one heterozygous mutant F3
1211 couple. For these experiments, genotyping on single embryos was performed on gDNA as
1212 mentioned above. Only WT homozygous and mutant homozygous embryos were kept for
1213 analysis.

1214 *Alternative Cpf1 approach*

1215 As an alternative approach to the CRISPR/Cas9 deletion, we attempted to generate a second
1216 mutant line, using to CRISPR/Cpf1(Cas12a) system to delete a 315 nucleotides region
1217 encompassing exon 38 (with specific guides located in the introns before and after exon 38).
1218 The sequence of guides that have been tested are: TATCACACACACATCACCTTCTA and
1219 TTTCTCAGCGCTCCTGACAGATG. However, due to the structure of the intronic regions
1220 (repeat rich) and the necessary presence of specific PAM sequence, we only generated off-
1221 target deletions of intronic regions, without deletions of exon 38, leading us to focus on the
1222 CRISPR/Cas9 approach.

1223

1224 **Morpholinos and injections**

1225 Morpholinos were obtained from GeneTools (see Key Resources Table for sequences). The
1226 *sih* Tnnt2 translation start codon and flanking 5-prime sequence MO (Sehnert et al. 2002) as
1227 well as the ArhGEF11 exon 38 splice blocking MO (overlapping the exon 38/intron 38-39
1228 boundary) were resuspended in ddH2O to obtain stock solutions at 2mM and 1mM,
1229 respectively. The *sih* MO (1.5ng) and ArhGEF11 exon 38 MO (3ng) were injected into 1-cell
1230 stage zebrafish embryos, after dilution in ddH2O. For *sih* morphants, embryos that were used

1231 in the experiments were checked for absence of heart beating 24 hrs after injection as well as
1232 before being used for dissection and RNA extractions at the 30-32 and 48-50 hpf time-
1233 windows. For measuring the efficiency of the ArhGEF11 exon 38 MO, total RNA was extracted
1234 from pools of injected and control embryos followed by mRNA reverse transcription. PCR on
1235 cDNA flanking the exon 38 was performed using DNA polymerase Platinum™ SuperFi™
1236 (Invitrogen Cat# 12351010) and analyzed on gel electrophoresis before extraction, cloning and
1237 sequencing to verify the absence of the DNA sequence encoded by exon 38 (see ***Figure 7 -***
1238 ***figure supplement 4A***).
1239
1240 **Whole mount single molecule fluorescent in situ hybridization (RNAscope)**
1241 48 hpf *Tg(kdrl:eGFP)* and *Tg(kdrl:Gal4;UAS:RFP;4xNR:dt-Runx1-eGFP)* embryos were fixed
1242 in 4% formaldehyde (Electron Microscopy Sciences, Cat#15712) diluted in PBS/0.1% tween20
1243 (PBST) for 2.5 hrs at room temperature, rinsed with PBST and kept in 100% methanol at -20°C
1244 until use. On the day of the experiment, embryos were rehydrated upon sequential incubations
1245 in 75%/50%/25% MeOH/ddH20 (each for 10 min at room temperature (RT)). Embryos were
1246 then incubated for 10 min in PBST. In subsequent steps of the RNAscope procedure, the
1247 Multiplex Fluorescent Reagent Kit v2 was used (Cat# 323100), that included H2O2; probe
1248 diluent (PD); wash buffer (WB); AMP1, AMP2, AMP3 buffers; HRP-C1, HRP-C2, HRP-C3
1249 reagents; TSA buffer; HRP blocker. All incubations were performed in Eppendorf tubes, with a
1250 maximum of 20 embryos/tube, in a dry heating block. Embryos were then incubated with H2O2
1251 for 10 min at RT, washed for 15 min in PBST at RT, incubated for 7 min at 37°C with proteinase
1252 K in PBST (1/2000 from a glycerol stock at 20mg/ml, Ambion, Cat#10259184), washed in
1253 PBST for 2x10 min at RT, and incubated for at least 2 hrs at 40°C in PD. Embryos were then
1254 incubated overnight at 40°C with the Pard3aa-C2, Pard3ab-C3, Pard2ba-C2 RNAscope
1255 probes.
1256 Next morning, embryos were washed for 2x10 min in WB. From that step on, extreme caution
1257 should be taken because embryos will become totally transparent, owing to the harsh

1258 conditions of the WB (we recommend that all washing steps, upon buffer removal, are
1259 performed under a binocular loupe). Embryos were then incubated sequentially with AMP
1260 buffers during 30 min for AMP1 and AMP2 and 15 min for AMP3, at 40°C, with 10 min washes
1261 at RT between each AMP buffer incubation. Embryos were then incubated for 15 min at 40°C
1262 with RNAscope Multiplex FL v2 HRP-C2 for Pard3aa and Pard2ba probes, HRP-C3 for the
1263 Pard3ab probe, washed for 10 min at RT with TSA buffer, incubated for 30 min at 40°C with
1264 OPAL-570 (PNFP1488001KT) in TSA buffer (dilution 1/500), washed 2x10 min at RT in WB,
1265 incubated for 15 min at 40°C in HRP blocker and finally washed 2x10 min in WB and 2x10 min
1266 in PBST at RT. Embryos were then embedded in 1% agarose and imaged by confocal
1267 microscopy, ideally immediately and no more than 2 days after mounting. Since eGFP can
1268 maintain its fluorescence property after fixation, Pard3 RNAscope spots could be relatively
1269 easily superposed to the fluorescence of eGFP expressed in endothelial cells.
1270 Images need to be analyzed with 3D-rendering (for example, with Imaris) to ensure the
1271 localization of RNAscope spots in a given cells.
1272
1273 **Whole mount chromogenic in situ hybridization**
1274 For the sequence of all the primers used to amplify probes (relative to PDZ-RhoGEFs, ***Figure***
1275 ***7 – figure supplement 2***), see the Key Resources Table. Whole-mount chromogenic in situ
1276 hybridization was performed as described in Lancino et al. 2018. Probes were synthetized
1277 using the manufacturer recommendation (T7 RNA polymerase, Promega, Cat# P2075, DIG-
1278 nucleotides, Jena Bioscence, Cat# NU-803-DIGX).
1279 Images were captured with the Zeiss Axio ZOOM V16 microscope with the Zen Pro2 software,
1280 with a brightfield transmitted light optics. Post-processing steps were performed using the
1281 Extended-Depth Focus method to combine in focus regions from multiple z-planes and convert
1282 into in a transmitted light z-stack to generate a unique in-focus image.
1283
1284 **Immunofluorescence detection of the HA-tagged dt-runx1 deletion mutant**

1285 Whole mount immunostaining was performed on hand-dechorionated 48 hpf *Tg(dt-runx1)*
1286 embryos to assess the localization of the 2XHA-tagged dt-runx1 protein in aortic cells. Briefly,
1287 embryos were fixed in 4% methanol free PFA (Polysciences Cat# 040181) for 3 hrs at room
1288 temperature (RT) and washed in PBS/0.1% tween20 (PBT). Embryos were treated in
1289 successive baths of milliQ water supplemented with 0.1% tween20, then in cold acetone for
1290 10 min at -20°C and again in milliQ water plus 0.1% tween20. They were then washed in 1X
1291 HBSS (Invitrogen Cat# 14025), and permeabilized for 45 min at RT in 1X HBSS, 0.1%
1292 tween20, 5mM CaCl2 and 0.1mg/ml collagenase (Sigma-Aldrich Cat# C9891). Embryos were
1293 then rinsed in PBSDT and incubated in blocking solution 1× sheep serum (SS, Sigma Cat#
1294 S2263) for at least 4 hrs at RT. They were then incubated overnight at 4°C with primary
1295 antibodies in blocking solution: rabbit anti-GFP (MBL Cat# 598; 1/300) and mouse anti-HA
1296 (Sigma, Cat# 12ca5; 1/50). On the next day, embryos were washed several times in PBSDT
1297 and endogenous peroxidase activity was inactivated by treatment with 6%H2O2 (Sigma-
1298 Aldrich, Cat# H1009) for 1 hr at 4°C. Embryos were then incubated in the NGS for at least 4
1299 hrs and incubated overnight at 4°C with secondary antibodies: goat anti-rabbit Alexa Fluor 488
1300 (Invitrogen Cat# A11070; 1/400) and goat anti-mouse HRP-conjugated (Thermo Fisher
1301 Scientific Cat# G-21040; 1/300). Finally, embryos were rinsed several times first in PBSDT and
1302 after in PBT before HRP fluorescent revelation. Embryos were incubated for 45 min at RT in
1303 the dark in imidazole buffer (0.1 M imidazole (Sigma-Aldrich, Cat# I5513) in PBT supplemented
1304 with 1% H2O2) with Cy3 Tyramide Reagent (Cy3 NHS sigma Cat# PA13101, tyramide sigma
1305 Cat# T-2879, dimethyl formamide sigma Cat# T-8654 and triethylamine sigma Cat# T-0886).
1306 Final washes in PBT and in 6% H2O2 for POD inactivation were performed before embryos
1307 were mounted in low-melting agarose in 1X PBT for fluorescence confocal imaging.
1308
1309 **Quantitative real-time PCR gene expression analysis**
1310 *Preparation of samples*

1311 In a first line of experiments, expression of pard3 family genes by qRT-PCR as well as of some
1312 hematopoietic markers myb and runx1 was evaluated in our tissue of interest at 48 - 50hpf.
1313 Total RNA was obtained from FACS sorted vascular cells of control embryo using an incross
1314 of *Tg(Kdrl:gal4;UAS:RFP)* as well as non-vascular cells (as described below). Cells were
1315 collected from either whole embryos or from dissected trunks. Subsequently, to determine the
1316 impact of runx1 interference on pard3 family genes, total RNA was obtained from dissected
1317 trunk regions of 48-50hpf embryos from either incross of control *Tg(Kdrl:gal4;UAS:RFP)* or
1318 mutant *Tg(Kdrl:dt-runx1-eGFP*) fish lines. Analyses were carried on 3 biological replicates.
1319 *Cell dissociation and Fluorescent Activated Cell Sorting*
1320 Single cell suspension for FACS sorting was prepared using an optimized protocol adapted
1321 from multiple sources (Manoli and Driever 2012; Samsa et al. 2016; Bresciani, Broadbridge,
1322 and Liu 2018). All steps were performed with cooled solutions (4°C), and samples were kept
1323 on ice throughout the processing to preserve the viability of the cells. Briefly, embryos were
1324 anesthetized using balneation in embryo medium supplemented with tricaine
1325 methanesulfonate (MS-222, Sigma-Aldrich ref #A5040), at a final concentration of 640 *µ*g/ml.
1326 Embryos were placed into a petri dish, rinsed in PBS supplemented with tricaine, and a majority
1327 of the medium was removed to prevent movement. Embryos were cut using a needle, and
1328 were then pooled in tubes and placed on ice until cell dissociation. Embryos trunks or whole
1329 embryos (around 120 or 60 respectively) were washed twice in PBS before centrifugation (300
1330 x g for 1 min @4°C) and the supernatant was discarded. Embryos were incubated in 1ml
1331 TrypLE medium (Life Technologies ref #12605-010) for 10 min on ice, with gentle pipetting
1332 every 3 mins, first with a P1000 pipette and subsequently with a P200 pipette. Samples were
1333 then centrifugated for 7 min at 300g to remove the TrypLE and the cells were resuspended in
1334 500*µ*l FACSmax medium (Genlantis ref#T200100). Ultimately, samples were passed through
1335 a 40µm cell strainer moistened with FACSmax buffer onto a 35 mm cell culture dish using a
1336 syringe plunger. The cell strainer and the dish were washed with 300*µ*l of FACS max and the
1337 flow-through was transferred to a FACS tube and kept on ice until sorting.

1338 Cell sorting was performed on a BD FACS AriaIII cell sorter. For all samples, gating was done
1339 on SSC-A vs. FSC-A to collect cells, and then on FSC-A vs. FSC-H to keep only single cells.
1340 For control embryos, RFP positive cells as well as RFP negative cells were collected. For dt-
1341 runx1 expressing mutant, all GFP positive cells (both RFP positive and RFP negatives) were
1342 collected, as well as RFP single positives cells (not used for qPCR) and double negative cells
1343 as internal controls. FASC sorted RFP single positives cells from dt-runx1 expressing mutants
1344 were not used as control for the study of gene expression for 2 reasons. First, due to the
1345 mosaicism of the line, very few cells were RFP single positive compared to the GFP positive
1346 cells. Second, RFP single-positive cells from dt-runx1 mutant embryos would have been
1347 indirectly exposed to runx1 interference (they would have been potentially in direct contact with
1348 their neighbouring endothelial cells that express the dt-runx1 mutant) and thus would not be a
1349 true no interference condition.

1350 *RNA extraction from FACS-sorted cells*

1351 Total RNA was extracted from sorted cell fractions using the RNeasy Qiagen kit (Qiagen, Cat
1352 # 74104). Briefly, cells were sorted directly into 100µl lysis buffer, and RNA extraction was
1353 done immediately according to the manufacturer's instructions. RNA was eluted twice with 15µl
1354 RNA free H2O. Reverse transcription of mRNA was performed using SuperScriptIV (Invitrogen
1355 Cat# 18090010) with OligodT primer. cDNA samples were stored at -20°C until further
1356 processing (for quantitative real-time PCR).

1357 *Real-Time qPCR*

1358 For the sequence of all the designed qRT-PCR primers, see the Key Resources Table. Primer
1359 couples were individually tested to assess their specificity as well as their efficiency. qRT-PCR
1360 was performed using Takyon Rox SYBR 2x Master mix blue dTTP kit (Eurogentec Cat# UF-
1361 RSMT-B0701), with starting concentrations of template of around 10ng/µl and primer
1362 concentrations of 0.5µM, on a QuantStudio3 system (Applied Biosystems). Each reaction was
1363 performed in technical triplicates and in 3 biological replicates. Ct was determined
1364 automatically by the QUANTSTUDIO™ DESIGN & ANALYSIS 2 software on the Thermofisher

1365 cloud and exported to be analyzed manually. Standard deviation was calculated within the
1366 technical triplicates, and when superior to 0.3, obvious outliers were removed (Dixon's Q test).
1367 The delta-delta-Ct method (double normalization to endogenous control — zebrafish
1368 elongation factor ef1α — and to control sample) was used to compare gene expression in
1369 control and altered conditions. The delta-Ct method (normalization to endogenous control ef1
1370 α) was used to investigate expression of genes of interest in whole embryo and trunk vascular
1371 cells versus non-vascular cells.
1372

1373 **In vivo confocal imaging**

1374 Embryos, dechorionated manually, were anesthetized using tricaine (Sigma Aldrich, Cat#
1375 A5040). They were then embedded on the side position in 1% low melting agarose (Promega,
1376 Cat# V2111) in a glass bottom 60µ-Dish (35mm high; Ibidi, Cat# 81156). To avoid movements
1377 and pigmentation during image acquisitions, 1x tricaine /1x PTU Volvic water was incorporated
1378 to the low melting agarose and, after solidification, 1ml of 1x tricaine /1x PTU Volvic water was
1379 added before sealing the dish.
1380 Embryos were imaged with 2 confocal microscope systems. For the results presented Figure
1381 1, z-stacks and time-lapse sequences were obtained using a Leica TCS SP8 inverted confocal
1382 microscope as described in Lancino et al 2018.
1383 For all the other confocal microscopy results, embryos were imaged using an Andor (Oxford
1384 Instruments) spinning disk confocal system (CSU-W1 Dual camera with 50µm Disk pattern
1385 and single laser input (445/488/561/642nm), LD Quad 405/488/561/640 and Tripl 445/561/640
1386 dichroic mirrors), equipped with a Leica DMi8 fluorescence inverted microscope and CMOS
1387 cameras (Orca Flash 4.0 V2+ (Hamamatsu)). Imaging was performed using a 40x water
1388 immersion objective (HC PL APO 40x/1.10 Water CORR CS2), a LEDs light source (CoolLED
1389 pE-4000 16 wavelength LED fluorescence system), and the acquisitions were piloted with the
1390 support of the MetaMorph software.

1391 RNAscope is situ hybridization were imaged similarly to live sample, using a spinning disk
1392 confocal microscope (see in vivo confocal imaging paragraph above) after embedding the
1393 embryos in 1% low-melting agarose (Promega, Cat# V2111) in PBS 1X in a glass bottom 60µ-
1394 Dish (35mm high; Ibidi, Cat# 81156).
1395
1396 **Morphological and morphometric analysis of aortic and hemogenic cells**
1397 For the morphometric analysis of the aorta and aortic cells, large z-stack of 48-55 hpf
1398 Tg(kdrl:eGFP-JAM3b; kdrl:nls-mKate2) or Tg(kdrl:eGFP-JAM2a; kdrl:nls-mKate2)
1399 encompassing the whole aortic depth were acquired with optimal z-resolution (0.3μm z-step).
1400 For each embryo, 3 contiguous z-stacks of 330μm width were acquired, allowing us to image
1401 the entirety of the AGM region, from the anterior to the posterior end of the elongated yolk.
1402 *Samples*
1403 For ArhGEF11 splicing morpholino experiment, 3 splicing morpholino injected embryos and 2
1404 control non injected siblings were kept for the analysis.
1405 For ArhGEF11 CRISPR Cter deletion and when performing the experiments, imaging was
1406 done, for putative mutants, on embryos that had shown a delay in initiation of circulation at 24
1407 hpf, regained circulation at 48 hpf albeit with a clearly visible oedema in the cardiac region
1408 (non-altered embryos were kept as sibling controls). All imaged embryos whose signal allowed
1409 us to generate segmentable 2D-cartography from the whole length of the aorta were kept and
1410 processed further for genotyping. Genotyping confirmed that the circulation problems at 24 hpf
1411 and the remaining oedema at 48 hpf corresponded to embryos bearing the mutation.
1412 For CRISPR mutant phenotype analyses, 2 mutant embryos and 2 wild type siblings were kept,
1413 after genotyping.
1414 *Image analysis*
1415 The following image analysis was performed on Icy software.
1416 For each segment, we generated a 2D-cartography of the eGFP-Jam signals at intercellular
1417 contacts of aortic cells, using the Tubeskinner plugin, according to the protocol described in

1418 Lancino et al 2018. Briefly, the aorta was rotated to face the lumen, a circular ROI fitting the
1419 interior of the aorta was initialized by the experimenter on the first plane, and for each plane
1420 sequentially, the algorithm will more accurately fit the ROI to the aortic perimeter and collect
1421 the fluorescence intensity all along its longitudinal axis. The collected intensity was then
1422 projected on a 2D-plane, where the Y-axis of the 2D-cartography corresponds to the perimeter
1423 of the aorta, and the X-axis corresponds to the X-axis of the original z-stack.
1424 Before further processing, a metadata table recapitulating the dates and conditions of
1425 experiments for each embryo was generated, and a random label was assigned to rename
1426 each acquisition. This allowed for the later part of the analysis, that involves semi-automated
1427 segmentation and classification by the user, to be blind and avoid potential bias.
1428 Each 2D-cartography was then manually pre-segmented using the ROI Polygon tool to draw
1429 the contour of each aortic cell, using the original 3D z-stack as reference. Due to technical
1430 limitation (decreased fluorescence signal collection on the farthest lateral side of the aorta),
1431 only about 2/3 of the 2D-cartographies could be segmented (comprising the floor, the right
1432 lateral side of the aorta and the roof). The manual segmentation was then improved using the
1433 “Active Contour” plugin, that improved the fit of the cellular contour to the fluorescence signal
1434 and slightly dilated the cell contours until the ROIs formed a joint paving. All morphometric
1435 descriptors were extracted for each cell. The number of neighbours was automatically
1436 generated for each cell by counting the number of touching adjacent ROIs.
1437 Additionally, cells were manually classified into cell types according to morphometric
1438 parameters using as reference the original 3D z-stack and in particular the nls-mKate2 nuclear
1439 signal. EHT-undergoing cells were positioned on the floor of the aorta, have reduce antero-
1440 posterior axis length, luminal membrane inward bending for EHT pol+ cells and luminal
1441 membrane outward bending for EHT pol- cells, and a thickened nucleus. Hemogenic cells
1442 whose criteria were established in Lancino et al 2018 (elongated in the antero-posterior axis,
1443 with lateral membranes not trespassing the equatorial plane of the aortic wall), are positioned
1444 on the floor of the aorta, systematically have a reduced width perpendicular to the blood flow

1445 and, importantly, a thickened nucleus that protrudes out of the aortic plane. Finally, endothelial
1446 cells have a flattened nucleus positioned high on the lateral side or on the roof of the aorta.
1447
1448 **Measurement of the aortic perimeter**
1449 An accurate measurement of the aortic perimeter was obtained using the z-stack generated
1450 for the aortic cells' morphometric analysis. Briefly, the z-stack was rotated to face the lumen of
1451 the aorta and a ROI fitting the aortic perimeter was drawn by the user and optimized by the
1452 "Cell Contour" plugin. The length of the perimeter was then extracted from the ROI statistics.
1453
1454 **Fluorescence Recovery After Photobleaching (FRAP) measurements and analysis**
1455 Measurement of junctional turn-over was performed on 48-55 hpf *Tg(kdrl:eGFP-JAM3b;*
1456 *kdrl:nls-mKate2)* embryos using a Nikon Ti2e spinning disk microscope equipped with a
1457 sCMOS camera (Photometrics, Prime 95B, pixel size 11μm, 1200×1200 pixels, QE 95%) and
1458 a 40x water objective (Numerical Aperture 1.15, Working Distance 0.6mm, xy pixel size of
1459 0.27μm). Embryos were mounted as previously described.
1460 *Samples*
1461 For ArhGEF11 splicing morpholino phenotypic analysis, 10 different embryos (injected with the
1462 splicing morpholino) obtained from 3 separate experiments and 30 control embryos (non-
1463 injected siblings or control morpholino injected siblings) obtained from 6 separate experiments
1464 were analyzed.
1465 For EHT analysis, 16 embryos over 4 separate experiments were analyzed.
1466 For ArhGEF11 CRISPR/Cas9 Cter deletion phenotypic analysis, 8 mutant embryos and 12
1467 wild type siblings over 3 separate experiments were analyzed.
1468 Overall, the exact number of interfaces analyzed is written on each figure panel.
1469 *Acquisitions*
1470 For each acquisition, a wide two channels z-stack of the aorta was generated to capture the
1471 whole aortic volume and generate a 2D-cartography of the aortic environment (Icy, plugin

1472 Tubeskinner). This 2D-cartography of the cellular contours and the z-stack with the cellular
1473 contours and nuclei were used jointly to identify un-ambiguously cellular and junctional types
1474 and define one or multiple single point regions of interest (ROIs) for subsequent bleaching and
1475 fluorescence recovery measurement.
1476 The sequence of acquisitions before/after bleach focused only on the eGFP-Jam3b signal to
1477 speed up the acquisition and improve the temporal resolution. The 5 steps of the acquisition
1478 can be recapitulated as follows and we obtained/performed: (1) a single z-stack of 20μm
1479 centered on the plane of focus, (2) a 30 sec time-lapse acquisition on the plane of focus to
1480 measure average pre-bleach intensity with an image every second, (3) a high intensity
1481 stimulation of the ROIs (25% 300ms 488 FRAP laser exposure, leading to the bleaching of the
1482 Jam3b-eGFP signal), (4) a 3 min time-lapse acquisition on the plane of focus to measure fast
1483 post-bleach recovery with an image every second, and (5) a 7 min time lapse acquisition of
1484 8μm z-stack centered around focus plane with a 20 sec time interval to measure slow post-
1485 bleach recovery. Each step was save separately as .nd2 files.
1486 *Signal quantification and recovery analysis*
1487 File were converted from .nd2 to .tiff using FIJI batch converter, scale factor 1.00, bilinear
1488 interpolation, no average when downsizing, images read using bioformat.
1489 To collect fluorescence intensity, ROIs for each stimulation point was manually drawn using
1490 Fiji and named with an individual label using Fiji ROI manager. A metadata table was manually
1491 curated with all information for each ROI (junction type, condition, date of experiment, embryo
1492 number). An additional ROI was created to collect background intensity for subsequent
1493 corrections. Acquisitions with clear embryo movement or drifting were either completely
1494 removed from the dataset (~5% of the acquisitions) or only kept for early recovery analysis
1495 (see below) if the drift only occurred in the last step (fifth) of the acquisition.
1496 Fluorescence intensity for each ROI was collected and saved automatically as a .csv file for
1497 each acquisition using a homemade Fiji macro.
1498 All further analysis were performed using R for automatization.

1499 Briefly, for each ROI: the fluorescent signal was normalized to the background signal ($I_{background}$

1500 $_{normalized} = I_{roi} - I_{background}$), then normalized to mean intensity pre-bleach

1501 ($I_{normalized} = I_{background\ normalized\ ROI\ post\text{-}bleach} / I_{background\ normalized\ ROI\ pre\text{-}bleach}$), and finally scaled

1502 ($I_{full\ scaled\ normalized} = (I_{normalized} - \min(I_{normalized}))/(1 - \min(I_{normalized}))$).

1503 A single exponential equation was used to fit the data using the nls:multistart package for

1504 parameter optimization:

1505 $F(t) = A*(1-e^{-t*\tau})$

1506 With A the maximum amplitude of the curve, t the time, and τ a constant defining the growth

1507 rate of the curve.

1508 The fitted curve allowed to extract quantitative information describing the recovery of each type

1509 of junction in different conditions: the mobile fraction of the bleached pool (corresponding to A,

1510 the amplitude of recovery) and the time of half recovery, related to the speed of recovery, that

1511 can be extracted from τ:

1512 $T_{half\text{-}recovery} = \ln(0.5)/(-\tau)$

1513 A more precise description of the recovery speed was extracted from the observation of the

1514 early time period (until 30s post bleach), were the fluorescence intensity increases uniformly.

1515 A first-degree polynomial equation was fitted to the data (using lm() function from the stats

1516 package), and the coefficient corresponding to the slope of the fitted curve was used as a

1517 metric for speed of fluorescence recovery.

1518

1519 **RNAscope image analysis**

1520 *Myb*

1521 Phenotypic analysis of the impact of the dt-runx1 mutant on hematopoiesis was evaluated by

1522 investigating the *in situ* expression of myb, using the single-molecule *in situ* hybridization RNA-

1523 scope method, performed in control *Tg(Kdrl:eGFP*) and dt-runx1 mutant embryos

1524 *Tg(Kdrl:Gal4;UAS:RFP;4xNR:dt-runx1-eGFP)* (analysis was performed on 4 and 3 biological

1525 replicates (embryos) for control and mutants respectively). For each embryo, 2 consecutive

1526 aortic segments were analyzed (each spanning over 5-6 intersegmentary vessels). It is roughly
1527 equivalent to the length to 3 consecutive aortic segments that we use for our live analysis (each
1528 spanning over 3-4 intersegmentary vessel. Discrepancies between live and fixed samples are
1529 probably due to the morphological alterations caused by the fixation and permeabilization
1530 steps of the RNAscope protocol. 3D-rendering of the aorta and the sub-aortic space were
1531 generated using the Imaris Software (Oxford Instruments, version 10.1.0). Both cell volume
1532 (GFP signal) and RNAscope spots were simultaneously and automatically segmented using
1533 the "Cells" tool from Imaris, that segment individual cells (generates an outer surface) as well
1534 as RNA-scope signal within cells. Cells were subsequently manually classified, based on their
1535 localization and the shape of the cell. Roof endothelial cells are located dorsally to the aortic
1536 floor, and are flat and elongated. Due to morphological alteration of the tissues and the
1537 impossibility to discriminate EHT pol-, EHT pol+ cells and the uncharacterized hemogenic cells
1538 we observed *in vivo*, our hemogenic / EHT cells category comprises both characterized
1539 hemogenic cells (elongated cells with thick nuclei, located on the aortic floor), uncharacterized
1540 hemogenic cells and putative EHT-undergoing cells. Sub-aortic cells were classified based on
1541 their localization, and they comprise a mix of endothelial cells from the underlying posterior
1542 cardinal vein (visible only in the control embryos and not in the dt-runx1 mutant embryos, in
1543 which arterial structures are more specifically labelled compared to veinous structures) as well
1544 as newly generated hematopoietic cells. Finally, the "Statistics" tool from Imaris allowed us to
1545 extract cell and RNA spots count information. The data plotting and statistical analysis was
1546 performed using R software.

1547 *Pard3*

1548 Pard3 isoforms (Pard3ba, Pard3ab, Pard3aa) *in situ* expression analysis was done similarly to
1549 that of myb, except that a second RNAscope signal segmentation was performed
1550 independently of the "Cells" segmentation, using the "spots" tool. This allowed to capture the
1551 majority of the Pard3 signal, that is expressed in aortic cells, but with a discrepancy in the intra-
1552 cellular localization of RNA transcript, that could not be detected when restricting the

1553 segmentation of RNAscope spots to spots located inside the GFP signal. After RNAscope
1554 segmentation using the “Spots” tool, manual curation allowed us to select specifically
1555 RNAscope spots located in aortic tissues for subsequent analysis. The “Statistics” and “object-
1556 object Statistics” tools were used to extract relevant spatial and count information for
1557 subsequent analysis. A key information that we used for the spatial analysis was the average
1558 distance of Pard3ba spots to Hemogenic / EHT cells, as well as the cumulative number of
1559 spots within a distance from Hemogenic / EHT cells, to investigation spatial correlation
1560 between Hemogenic / EHT cells and Pard3ba expression. Analysis was performed in control
1561 *Tg(Kdrl:eGFP*) and dt-runx1 mutant embryos *Tg(Kdrl:Gal4;UAS:RFP;4xNR:dt-runx1-eGFP)* (5
1562 and 6 biological replicates (embryos) for control and mutants respectively, with 2 consecutive
1563 aortic segments analyzed per embryo).
1564
1565 **Dt-runx1 phenotype analysis – cell count**
1566 For the live dt-runx1 phenotype analysis, large z-stack of 48-55 hpf dt-runx1 expressing mutant
1567 (eGFP positive) and siblings control (eGFP negative) *Tg(Kdrl:Gal4;UAS:RFP;4xNR:dt-runx1-*
1568 *eGFP)* embryos, encompassing the whole aortic depth were acquired with optimal z-resolution
1569 (0.3μm z-step). 3 and 7 biological replicates (embryos) for control and mutants respectively
1570 were analyzed. For each embryo, 3 contiguous z-stacks of 330μm width were acquired,
1571 allowing us to image the entirety of the AGM region. The resulting phenotype was assessed
1572 by manually counting EHT pol+ and pol- cells (taking into account their position, ventral or
1573 lateral) as well as hemogenic cells. Classification was done manually, based on morphological
1574 criterias. EHT pol+ cells presented the typical EHT pol+ morphology, with clear luminal
1575 membrane invagination, that could be observed even in laterally emerging cells. EHT pol- cells
1576 displayed a clear rounded ovoid, with a clear shortening of the antero-posterior axis.
1577 Hemogenic cells correspond to endothelial cells located on the aortic floor, that are elongated
1578 along the antero-posterior axis, have a narrowed left-right axis and a thickened nucleus. Non
1579 characterized hemogenic cells were also included in this category: they correspond to cells

1580 that had potentially already advanced in the emerging process but whose morphology did not
1581 fit any of the typical EHT pol- and pol+ characteristics (no clear invagination nor clear concave
1582 protrusion in the aortic lumen).

1583 *Thymus phenotype analysis*

1584 To question one aspect of the hematopoietic phenotype of our dt-runx1 mutant, dt-runx1
1585 expressing mutants (GFP+ RFP-) as well as control siblings (RFP+ GFP-) were imaged at 5dpf
1586 to analyze their developing thymus *in vivo* (analysis was performed on 5 mutant and 5 control
1587 larvae). Subsequent image analysis was performed using the Imaris software (Oxford
1588 Instruments). Individual thymic cells were automatically segmented using the "Surface" tool.
1589 Cell count per thymus as well as morphometric information for each cell (volume) was
1590 automatically retrieve using the Imaris "Statistics" tool, allowing us to compare the distribution
1591 of cell volume in mutant versus control embryos, as well as the total cellular volume of the
1592 thymus (sum of individual cell volumes) for each larva.

1593

1594 **Impact of ArhGEF11 exon38 splicing morpholino on hematopoiesis**

1595 After morpholino injection at the one cell stage, double transgenic *Tg(CD41:eGFP; kdrl:nls-*
1596 *mKate2)* embryos were raised until 48hpf and imaged using spinning disk confocal
1597 microscopy. The integrality of the dorsal aorta was imaged (corresponding to 3 contiguous
1598 segments), on 8 and 6 biological replicates (embryos) for controls and morphants respectively.
1599 Quantification of the number of hemogenic cells (double CD41:eGFP and kdrl:nls-mKate2
1600 positive cells) as well as of hematopoietic cells (simple positive CD41:eGFP and kdrl:nls-
1601 mKate2 negative cells) was performed using a in house Fiji/R script. For the segmentation,
1602 only the eGFP channel is handled. An issue with the *Tg(CD41:eGFP)* background is the
1603 presence of circulating thrombocytes, that move faster than the speed of acquisition and thus
1604 generate multiple artefactual 2D objects (only presents in single Z-planes, compared to non-
1605 moving cells whose depth spans over 15-20 z-sections). These artefactual objects are
1606 removed during the pre-processing steps, by using a Faster Temporal Median algorithm

1607 (Jabermoradi et al. 2022). This algorithm, by calculating median value over rolling windows of
1608 20 frames approximate cell depth) and substracting it to the pixel values, removes the 2D
1609 outliers. The rest of the pre-processing steps consists of fluorescent signal filters to ease the
1610 subsequent segmentation (contrast enhancement, background substraction, 3D gaussian
1611 blur). The cells are segmented using a TopHat algorithm and touching objects are separated
1612 using a 3D distance Watershed (Legland, Arganda-Carreras, and Andrey 2016). Once the
1613 objects are segmented, the total fluorescence intensity in both channels as well as the
1614 background fluorescence intensities are collected using the raw images (without any signal
1615 filters). The data are subsequently processed using R for plotting, threshold selection for
1616 classification as well as statistical comparisons.
1617
1618 **Statistical analysis**
1619 Statistical tests used are described for each figure panel in the legend. Since our samples are
1620 usually small, the test used is an unpaired two samples non-parametrical Wilcoxon mean
1621 comparison test, without a priori knowledge on sample distribution or homoscedasticity. In the
1622 context of FRAP experiments (relative to ***Figure 6*** and ***Figure 8***), for which we had larger
1623 sample size, we still decided not to assume that our data were normally distributed, because
1624 of the inherent variability of the biological events that are observed. Indeed, the EHT process
1625 is heterogeneous in time, with successive phases of contraction and stabilization, during which
1626 we can imagine that the dynamics of junctional recycling could vary. The distribution of speed
1627 and amplitude of recovery could thus correspond to a normal distribution, a bi- or multi-modal
1628 distribution, or a uniform distribution. In this case, the use of non-parametrical tests and the
1629 large variability we observed in the data reduces the power of statistical tests and our ability to
1630 confidently detect significant differences. In some cases, when our p-values were larger than
1631 the arbitrary threshold of 0.05, we refer to tendencies whose significance is legitimated by the
1632 overall consistency of the data (see for example between the results presented ***Figure 7*** and
1633 ***Figure 8***).

1634 Correlation analysis (relative ***to Figure 4F***) was performed by calculating Pearson correlation
1635 coefficient and associated p-value (Student T-test) using R.
1636
1637 **Data and software availability**
1638 All graphics and plots were generated using RStudio and packages including: ggplot2
1639 (Wickham 2016), readr (Wickham, Hester, and Bryan 2022), dplyr (Wickham et al. 2023),
1640 stringr (Wickham 2022), ggstatsplot (Patil 2022), ggpubr (Kassambara 2020), wesanderson
1641 (Ram and Wickham 2018), cowplot(Wilke 2020), ggsci (Xiao 2018), ggbeeswarm (Clarke and
1642 Sherrill-Mix 2017), viridis (Garnier 2021), DT (Xie, Cheng, and Tan 2022), SciViews (Grosjean
1643 2019), nls.multstart (Padfield and Matheson 2020), matrixStats (Bengtsson 2022).
1644
1645
1646 **Acknowledgments**
1647 We wish to warmly thank Philippe Herbomel for his encouragements and for ensuring the
1648 funding of this study.
1649 We thank our fish facility members Y. Rolin and K. Sebastien for their daily help and
1650 commitment. We thank Sandrine Schmutz and Gaëlle Letort for their expertise and invaluable
1651 assistance. We acknowledge the help of the Cytometry and Biomarkers (UTechS CB) service
1652 platform for expert assistance with FACS analysis, of the Image Analysis Hub, and of the
1653 Photonic BioImaging (UTechS PBI) service platform of the Institut Pasteur for their respective
1654 contributions.
1655 We wish to thank R. Patient (University of Oxford) for the Hsp70 promoter. This work was
1656 supported by Institut Pasteur, CNRS, grants to P. Herbomel from the Fondation pour la
1657 Recherche Médicale (#DEQ20160334881), the Fondation ARC pour la Recherche sur le
1658 Cancer, and the Agence Nationale de la Recherche Laboratoire d'Excellence Revive
1659 (Investissement d'Avenir, ANR-10-LABX-73), and a grant to AS from the Institut Pasteur (PTR

439-2021). LT was recipient of a PhD fellowship from the Collège Doctoral, Sorbonne Université, and from the Labex Revive (ANR-10-LABX-73).

Authors contributions

LT designed, performed and analyzed experiments, and wrote the Method section and the Figure legends. SM designed and conducted experiments. CV conducted experiments. AS conceived the project, designed, performed and analyzed experiments, wrote the manuscript with input from LT, and obtained funding.

Declaration of interests

The authors declare no competing interests.

1671 ## Figure legends

1672

1673 **Figure 1: Tracing the evolution of the luminal membrane using the polarity marker**
1674 **Podocalyxin points at the biological significance of apicobasal polarity establishment**
1675 **in EHT cell emergence complexity. A**, cartoons depicting the early and late steps of EHT
1676 cells emerging from the aortic floor (steps 1 and 2, as previously described in the zebrafish
1677 embryo, see (Kissa and Herbomel 2010; Lancino et al. 2018)) and with hypothetical evolution
1678 of the luminal membrane (in green) before (3 and 4) and after the release (2', the cell detaches
1679 from the endothelial layer via junction downregulation leading to exposure of the luminal
1680 membrane with le extracellular milieu; 3', the luminal membrane is consumed via endocytic
1681 recycling (E) and/or lysosomal degradation (Lys) prior to detachment; 4', the luminal
1682 membrane in 4 is released inside the cell (twisted arrow) before detachment. Grey area=
1683 nucleus. **B**, PodocalyxinL2 (Podxl2) construct designed to establish transgenic fish lines.
1684 Cartoons representing full length (top drawing) and deleted Podxl2 (amino-acid sequence 341-
1685 587) in which the mucin domain (serine/threonine-rich O-glycosylation domain) is replaced by
1686 either eGFP or mKate2. The tetracystein-containing globular domain (subjected to N-
1687 glycosylation) was kept as favoring apical membrane retention. TMD, transmembrane domain;
1688 DTHL, C-terminal peptidic motif involved in partnership with PDZ domain containing proteins.
1689 **C-D**, EHT performing cells visualized using *Tg(Kdrl:Gal4;UAS:RFP;4xNR:eGFP-podxl2)*
1690 embryos and time-lapse sequences initiated at 55 hpf obtained with spinning disk confocal
1691 microscopy (imaging was performed at the boundary between the most downstream region of
1692 the AGM and the beginning of the caudal hematopoietic tissue). Top grey panels show the
1693 green, eGFP channels for eGFP-podxl2 only. Bottom panels show the merge between green
1694 and red (soluble RFP, in magenta) channels. Bars: 8μm. **C**, single plane images of 2 EHT pol+
1695 cells extracted from a time-lapse sequence at t = 0 and t = 45 min, with the right cell (eht cell
1696 2) more advanced in the emergence process than the left one (eht cell1). Note the enrichment

1697 of eGFP-podxl2 at the luminal membrane (surrounding the cavity labelled with an asterisk) in
1698 comparison to the basal membrane (white arrow). Note also the evolution of the luminal
1699 membranes with time, with the aortic and eht cell 1 lumens still connecting at t = 0 (green
1700 arrow), the apparent fragmentation of the cytosolic vacuole (2 asterisks for eht cell 1 at t = 45
1701 min) and the compaction of Podxl2-containing membranes for eht cell 2 at t = 45 min. More
1702 details on the evolution of the connection between the aortic/eht cell lumens are shown in
1703 ***Figure 1 – figure supplement 1A***. **D**, single plane images of 2 EHT pol- cells extracted from
1704 a time-lapse sequence at t = 30 min and t = 210 min (see ***Figure 1 – video 3*** for the full-time
1705 lapse sequence), with the right cell (eht cell 2) slightly more advanced in the emergence than
1706 the left one (eht cell 1, with the latest attachment point between the emerging cell and the
1707 aortic floor (pink arrow)). Note, in comparison with the cells in panel C, the ovoid shapes of
1708 cells, the absence of enrichment of eGFP-podxl2 at luminal membranes (green arrows) and
1709 the accumulation of eGFP-podxl2 at basal membrane rounded protrusions (white arrows).
1710
1711 **Figure 2: Immature HE is not polarized and controls membrane delivery of intra-**
1712 **cytosolic vesicular pools**. **A**, *Tg(Kdrl:Gal4;UAS:RFP;4xNR:eGFP-podxl2)* embryo imaged
1713 using spinning disk confocal microscopy. Black and white images show eGFP-podxl2 only.
1714 Images (single z-planes) were obtained from a time-lapse sequence (initiated at 35 hpf) lasting
1715 for 435 min (7.25 hrs), with intervals of 15 min between each z-stack. Example of an HE cell
1716 with equal partitioning of eGFP-podxl2 between luminal and abluminal membranes (at t = 0
1717 min), with eGFP-podxl2 containing intra-cytosolic vesicles (one labelled with a green asterisk)
1718 and undergoing mitosis at t = 30 min (HE cell 1' and HE cell 1'' are daughter cells). Note the
1719 inheritance of the largest micropinocytic-like vacuole by HE cell 1' and its maintenance over
1720 time until EHT emergence initiation at t = 180 min (green asterisk in 1.5x magnified areas at t
1721 = 60 and 90 min). At t = 360 min (green box) EHT is proceeding and both fluorescence
1722 channels are shown; bottom panel: green (eGFP-podxl2), magenta (soluble RFP). The

1723 magenta arrow points at the basal side of the EHT pol + cell (EHT cell 1', on the right) that
1724 does not contain any detectable eGFP-podxl2; on the contrary, eGFP-podxl2 is enriched at
1725 the luminal/apical membrane (note that exocytosis of the large vacuolar structure may have
1726 contributed to increase the surface of the apical/luminal membrane (the green asterisk is
1727 surrounded by the apical/luminal membrane of the EHT pol + cell)). The green arrow points at
1728 the abluminal membrane of the EHT cell derived from HE cell 1'' (EHT cell 1'') and that contains
1729 eGFP-podxl2 (with no evidence of a significant expansion of a luminal/apical membrane); this
1730 indicates that this cell is more likely to be an EHT pol- cell that did not sort the vesicular cargo
1731 to the luminal/apical membrane. Bar = 10μm. **B**, hypothetical model summarizing the evolution
1732 of HE cells involving the tuning of apicobasal polarity to lead to cells competent for giving birth
1733 to either EHT pol+ or EHT pol- cells (including the release of large vesicular macropinocytic-
1734 like vacuoles preferentially toward the luminal membrane of future EHT pol + cells). The
1735 polarity status of HE cells is proposed to evolve asynchronously throughout the entire EHT
1736 time window, leading to place-to-place ability to give birth to EHT cells (emergence of EHT
1737 pol+ and EHT pol- cells are both observed until 72 hpf, see main text).
1738
1739 **Figure 3: Interference with Runx1 function alters emergence efficiency and induces a**
1740 **bias toward EHT pol+ cells. A,** *Tg(kdrl:Gal4;UAS:RFP;4xNR:dt-runx1-eGFP)* mutant
1741 embryos imaged using spinning disk confocal microscopy and analyzed in the AGM/trunk
1742 region. Z-projections of the dorsal aorta obtained from 52 - 55 hpf embryos. **Top panel:**
1743 fluorescence from the red channel is shown for the *Tg(Kdrl:Gal4;UAS:RFP)* control. **Bottom**
1744 **panels:** fluorescence in the green channel only is shown for the mutants (eGFP, released from
1745 the dt-runx1-eGFP cleavage). The black asterisks point at emerged cells that are in close
1746 contact with the aortic floor. Green arrows: EHT pol+ cells on aortic floor; magenta arrows:
1747 EHT pol+ cells in the lateral aortic wall; blue arrows: uncharacterized emerging cells; he:
1748 hemogenic cells. **B,** quantitative analysis of the dt-runx1 mutant phenotype. The analysis was
1749 carried out on *Tg(Kdrl:Gal4;UAS:RFP)* control embryos (n = 3) and on

1750 Tg*(kdrl:Gal4;UAS:RFP;4xNR:dt-runx1-eGFP)* mutant embryos (n = 7). **Left top**: hemogenic
1751 cell count (comprising hemogenic cells, labelled by "he" on panel **A**, as well as uncharacterized
1752 emerging cells, labelled by blue arrows on panel **A**). **Left center**: EHT pol+ cell count (sum of
1753 EHT pol+ cells emerging ventrally and laterally, respectively labelled by green and magenta
1754 arrows on panel **A**). **Left bottom**: EHT pol- cell count (not shown on panel **A**). **Right**:
1755 percentage of cell types in control and dt-runx1 embryos (proportions relative to total number
1756 of hemogenic and EHT undergoing cells). Statistical comparisons have been performed using
1757 two-sided unpaired Wilcoxon tests, all p-values are displayed. **C**, **top:** cartoons representing
1758 the zebrafish full-length runx1a amino-acid sequence and the dt-runx1 mutant deleted from
1759 the trans-activation domain and of the C-terminus (note that the construct encodes for a C-
1760 terminal fusion with eGFP that is released upon expression via a cleavable T2A peptide
1761 (introduced between the 2xHA tag and the N-terminus of eGFP, to prevent from potential steric
1762 hindrance). nls, nuclear localization signal. **Bottom:** image of an anti-HA tag
1763 immunofluorescence obtained after z-projection of the dorsal aorta of a 50 hpf *Tg(dt-runx1)*
1764 embryo. Note the localization of the 2xHA-tagged dt-runx1 protein in nuclei (some of them are
1765 pointed by red arrowheads) and of eGFP in nuclei and the cytosol of aortic cells. Bar: 25μm.
1766

1767 **Figure 4. Pard3ba expression is highly sensitive to interference with Runx1 activity. A,**
1768 Pard3aa, ab, ba and bb zebrafish isoforms, with their accession numbers. The cartoon
1769 represents the common structures of the 4 isoforms, with the 3 sequential PDZ domains
1770 (PDZ1-3), and the CR1 and CR3 conserved regions involved in oligomerization and atypical
1771 protein kinase C (aPKC) binding, respectively. The magenta arrows show the positioning of
1772 qRT-PCR primers, located in the PDZ1 domain (see ***Methods*** for primer sequences). **B**, qRT-
1773 PCR analysis of genes expression levels of (**left**) the hematopoietic markers myb and runx1,
1774 (**right**) the 4 isoforms of Pard3 proteins (Pard3aa, ab, ba and bb) in cell populations isolated
1775 from FACS-sorted trunk vascular cells of 48 - 50 hpf control and mutant embryos (see ***Figure***
1776 ***4 - figure supplement 1***, ***Figure 4 - figure supplement 2*** and ***Methods*** for cell isolation

1777 procedures). Graphs show the measured mean fold changes relative to the expression of ef1α
1778 and to the expression in RFP+ control cells. Statistical tests: two sided unpaired two samples
1779 Wilcoxon test, all p-values are displayed. Analysis was carried out on n = 3 for control and
1780 mutant conditions. **C**, representatives images (Imaris 3D-rendering) of RNAscope *in situ*
1781 hybridizations for Pard3ba in 48 - 50hpf *Tg(Kdrl:eGFP)* control embryos and
1782 *Tg(Kdrl:Gal4;UAS:RFP;4xNR:dt-runx1-eGFP)* mutant embryos. The aorta is outlined with the
1783 white dashed lines. The RNAscope signal was segmented into spots and classified based on
1784 its localization: in aortic endothelial and hemogenic cells (magenta spots) or in extra-aortic
1785 tissues (grey spots, essentially residing in the sub-aortic space). Magenta dashed boxes
1786 delineate examples of mRNA Enriched Regions (MERs) in control and mutant embryos. Scale
1787 bars: 10*µ*m. **D**, Pard3ba spots count per aortic segment. **E**, Pard3ba spots count per
1788 hemogenic/EHT cells. **F**, cumulative Pard3ba spots count relative to hemogenic/EHT cell
1789 distance, averaged for each aortic segment, in control embryos (grey) and dt-runx1 mutant
1790 embryos (orange). **G**, HE/EHT cell count relative to number of spots, all expressed per aortic
1791 segment (**left**), 50% Pard3ba spots attraction distance (in *µ*m) (**middle**) or 75% Pard3ba spots
1792 attraction distance (in *µ*m) (**right**). 50%/75% spots attraction distance corresponds to the
1793 distance from hemogenic/EHT cells within which 50%/75% of Pard3ba spots are located. Grey
1794 dash lines correspond to regression lines and light grey background correspond to the
1795 confidence interval (95%) of the regression model. Linear correlation coefficient (R, Pearson
1796 correlation) is displayed for each condition. For **D** and **E**, statistical tests: two sided unpaired
1797 two samples Wilcoxon test, all p-values are displayed. Analysis was carried out on n = 5 control
1798 embryos and n = 6 mutant embryos, 2 aortic segments per embryos. For **G**, p-values were
1799 calculated using a t-test.
1800
1801 **Figure 5: eGFP-Jam3b localization is reinforced at antero-posterior sites of the**
1802 **endothelial/EHT interface and at tri-cellular junctions. A**, cartoons representing
1803 homodimers of full-length JAMs with the C-terminal cytosolic part interacting with Pard3 (JAMs

1804 interact with the first PDZ domain of Pard3) as well as the constructs generated in this study
1805 and containing eGFP inserted between the Immunoglobulin-like (Ig) domains and the trans-
1806 membrane region (TMD). The constructs were obtained for zebrafish JAM2a and JAM3b. **B,**
1807 **C**, 52 hpf *Tg(kdrl:eGFP-Jam3b; kdrl:nls-mKate2)* embryos were imaged in the trunk region
1808 (AGM) using spinning disc confocal microscopy. The panels are either maximum z-projections
1809 (top two) or single plane z-sections (bottom two, focusing on the aortic floor) of aortic
1810 segments, with either the merged nls-mkate2 and eGFP-Jam3b fluorescence signals
1811 (magenta and green) or the eGFP-Jam3b signal only (black and white images). Bottom of the
1812 Figure: 2D-cartographies obtained after deploying aortic cylinders and showing the eGFP-
1813 Jam3b signals only. The white/black vertical dashed lines show the correspondence of the
1814 antero-posterior junctional reinforcements in the single z-sections (white arrows) on the
1815 respective 2D-cartographies resulting from the deployment of the aortic walls (obtained from
1816 the z-stacks). **B**, example of an EHT pol+ cell (cell 1, white arrows point at reinforcement of
1817 signal at antero-posterior junctions). On the 2D cartography, cell 1 (red) is contacting
1818 endothelial cells 2 and 3; note the reinforcement of eGFP-Jam3b signals along antero-
1819 posterior membrane interfaces perpendicular to blood flow (red arrows) as well as at the two
1820 tri-cellular junctions visible between cells 1, 2 and 3 (black arrows). **C**, example of two EHT
1821 pol- cells (cells 1 and 2, white arrows point at reinforcement of signal at antero-posterior
1822 junctions). On the 2D cartography, cells 1 and 2 (red) are contacting endothelial cells 3, 4, 6
1823 and 3, 6 respectively; note the reinforcement of eGFP-Jam3b signals along antero-posterior
1824 membrane interfaces perpendicular to blood flow (red arrows) and endothelial cell 6 that has
1825 intercalated between endothelial cell 7 and EHT pol- cell 2 (blue arrow). In right margins,
1826 magenta and green arrowheads designate the aortic floor and roof, respectively. Bars = 10μm.
1827

1828 **Figure 6: Junctional recycling at tri-cellular contacts is differentially controlled between**
1829 **the two EHT types.** 48-55 hpf *Tg(kdrl:eGFP-Jam3b; kdrl:nls-mKate2)* embryos were imaged
1830 using spinning disc confocal microscopy and illuminated for Fluorescence Recovery After

1831 Photobleaching (FRAP) in the trunk region (AGM, Aorta Gonad Mesonephros). **A, B**, panels
1832 are either maximum z-projections (top left) or single plane z-sections (bottom left and top right,
1833 focusing on the aortic floor) of aortic segments, with either the merged nls-mkate2 and eGFP-
1834 Jam3b fluorescence signals (magenta and green) or the eGFP-Jam3b signal only (black and
1835 white images). White arrows point at reinforcement of signal at antero-posterior junctional
1836 pools of an EHT pol+ cell (**A**) or of an EHT pol- cell (**B**), both marked by asterisks. Bottom right:
1837 2D-cartographies obtained after deploying aortic cylinders and showing the eGFP-Jam3b
1838 signals only. Black arrows point at antero-posterior junctional pools, in particular at tri-
1839 junctional regions that exhibit increase in signal density (well visible in **A,** black arrows). 2 and
1840 3 endothelial cells are contacting the EHT pol+ cell (**A**) and the EHT pol- cell (**B**), respectively.
1841 In right margins, magenta and green arrowheads designate the aortic floor and roof,
1842 respectively. Bars = 20μm. **C - G,** FRAP analyses. EGFP-Jam3b junctional pools
1843 corresponding to the brightest spots inside junctional regions of interest were bleached for
1844 FRAP measurements (these high intensity pools were localized at the level of bi- and tri-
1845 junctions for endothelial cells (EC) and in tri-junctional regions for EHT pol+ and EHT pol- cells;
1846 all these junctional pools were systematically visualized by deploying each aortic segment
1847 before bleaching as shown in the 2D-cartographies in A and B as well as in ***Figure 6 – figure***
1848 ***supplement 1***, see also ***Methods***). FRAP analysis concerned 3 types of junctional interfaces:
1849 between endothelial cells (EC – EC, black and grey), EHT pol- and endothelial cells (pol- –
1850 EC, brown), EHT pol+ and endothelial cells (pol+ – EC, blue). **C, D**, evolution of mean
1851 fluorescence intensity for each type of junctional interface over time (10 min), after
1852 photobleaching (t = 0s). **E**, median maximum amplitude of recovery of all determinations and
1853 for each type of junctional interface (maximum of simple exponential fitted curves). **F, G**, early
1854 fluorescence recovery. Early evolution (over the first 30s) of the mean fluorescence intensity
1855 for each type of junctional interface over time after photobleaching (t = 0s). **F**, the fitted lines
1856 correspond to linear regressions of mean fluorescence intensities. **G**, median values of
1857 fluorescence recovery slopes (linear regressions) of all determinations and for each type of

1858 junctional interface. **E, G**, the number of biological replicate (n) is stated on the plots. Statistical
1859 tests: two sided unpaired two samples Wilcoxon test.
1860
1861 **Figure 7: Interfering with ArhGEF11/PDZ-RhoGEF function leads to the accumulation of**
1862 **hemogenic cells and impairs EHT progression. A-C,** numeration and morphometric
1863 analyses of aorta and cell types for *Tg(kdrl:eGFP-Jam3b; kdrl:nls-mKate2)* ArhGEF11 exon
1864 38 splicing morpholino-injected and control embryos (**A**), or for *(Kdrl:eGFP-Jam3b;*
1865 *kdrl:*ArhGEF11$^{\text{CRISPR-Cterdel+/+}}$) homozygous ArhGEF11 C-ter deletion mutants and control
1866 siblings (**B**). 48-55 hpf embryos were imaged using spinning disk confocal microscopy. **Aa,**
1867 **Bb**, 2D-cartographies obtained after deploying aortic cylinders and showing the eGFP-Jam3b
1868 signals only with cell contours delineated either in blue (endothelial cells), yellow (hemogenic
1869 cells, see ***Methods*** for their morphological definition), red (morphologically characterized EHT
1870 cells, for controls), and small cells delineated by cyan boxes (morphologically uncharacterized
1871 EHT cells and putative post-mitotic cells remaining as pairs, included in the numeration as
1872 hemogenic cells). Cellular contours have been semi-automatically segmented along the
1873 cellular interfaces labelled with eGFP-Jam3b (see ***Methods***). Scale bars: 10μm. **Aa', Bb'**, **left:**
1874 numeration of endothelial, hemogenic and EHT-undergoing cells according to the position of
1875 their geometrical center (either on the aortic floor, or on the roof, or on the lateral side), for
1876 each condition; **right**: number of endothelial, hemogenic and EHT-undergoing cells in each
1877 condition calculated from the segmentation of 3 x 2D-projections per embryo and covering the
1878 entire aortic regions in the trunk. **Aa'', Bb''**, **left**: length of hemogenic cells (in the longest axis)
1879 in function of their orientation (°) relative to the blood flow axis (0 – 180°); **right**: distribution of
1880 the orientation of hemogenic cells relative to the blood flow axis, displayed as a mean
1881 distribution of cells per embryo. **Aa''', Bb'''**, hemogenic cell elongation factors in arbitrary Units
1882 (scale factor given by the ratio between the first- and the second-best fitting ellipse diameters,
1883 the minimum value being 1 for a non-elongated object) represented as boxplot distribution of

1884 all segmented cells (**left**) or as the distribution of cell elongation factor per embryo (**right**), for
1885 controls and for interfering conditions as indicated. **Aa'''', Bb''''**, hemogenic cell area
1886 represented as boxplot distribution of all segmented cells (**left**) or as the distribution of cell
1887 area per embryo (**right**), for controls and for interfering conditions as indicated. **C**, aortic
1888 perimeter (in μm) for controls and mutant conditions as indicated. Statistical tests: two sided
1889 unpaired two samples Wilcoxon test. For the ArhGEF11 exon 38 splicing morpholino
1890 condition, analysis was performed on 2 x control (non-injected embryos) and 3 x embryos
1891 injected at the one-cell stage; for the CRISPR mutant condition, analysis was performed on 2
1892 x wild-type siblings for control and 2 x homozygous mutant embryos whose DNA mutation was
1893 confirmed by sequencing. 3 consecutive aortic segments per embryo were analyzed to cover
1894 the whole length of the dorsal aorta, in the trunk region (covering a distance of 990μm per
1895 embryo).
1896
1897 **Figure 8: Interfering with the function of ArhGEF11/PDZ-RhoGEF suggests an activity**
1898 **at the interface between endothelial and hemogenic cells that relies on restricting the**
1899 **mobility of junctional pools at tri-cellular junctions, with a prominent role of the +exon**
1900 **38 variant during endothelial cell intercalation. A**, 2D-cartography of an aortic segment of
1901 a *Tg(kdrl:eGFP-Jam3b; kdrl:nls-mkate2)* embryo injected at the one cell stage with the
1902 ArhGEF11 exon 38 splicing morpholino. All the arrows pointing at reinforced junctional
1903 contacts between cells were bleached and imaged for FRAP analysis (the bleached areas
1904 correspond to the spots of highest intensities in the regions of interest, as visualized at the
1905 fluorescent confocal microscope, see ***Methods***). Black and Magenta arrows point at he-he-ec
1906 and he-ec-ec tri-cellular junctions, respectively (he: hemogenic cell; ec: endothelial cell). Green
1907 arrows point at he-ec bi-cellular junctions. ec: endothelial cell, he: hemogenic cell. Bar = 20μm.
1908 **B, C**, FRAP analysis of bleached eGFP-Jam3b localized in regions of interest in controls (grey)
1909 and ArhGEF11 exon 38 splicing morpholino injected embryos (blue) or homozygous

1910 ArhGEF11$^{CRISPR\text{-}Cterdel+/+}$ mutants (green)). The number of biological replicates (n) is stated on
1911 the plots. Statistical tests: two sided unpaired two samples Wilcoxon test. Bb, Cc, evolution,
1912 after photobleaching (at t = 0s), of the mean fluorescence intensity per condition at HE-EC,
1913 HE-EC-EC and HE-HE-EC bi- and tri-junctions over time (10 min). Bb', Cc', median values for
1914 maximum amplitude of recovery (maximum of simple exponential fitted curves, see ***Methods***).
1915 Bb'', Cc'', early evolution, after photobleaching (at t = 0s), of the mean fluorescence intensity
1916 per condition over time (for the first 30 seconds). The fitted lines correspond to the linear
1917 regression of the mean fluorescence intensities. Bb''', Cc''', median fluorescence recovery
1918 slopes (linear regression). **D**, Model (2D deployment of the aortic wall) representing the
1919 endothelial/hemogenic dynamic interplay and the proposed function of ArhGEF11 and of its
1920 +exon 38 peptide encoding variant at junctional and membrane interfaces. This interplay
1921 involves 2 essential dynamic events requiring junctional remodeling: **1** (left cartoon, magenta
1922 arrows), the mobility of he-ec-ec tri-junctional contacts accompanying the movement of
1923 endothelial cells (ex: for ec1 and ec2) along lateral sides of hemogenic cells which is required
1924 to decrease the number of adjoining cells (see Lancino et al. 2018). This takes place
1925 contemporarily to - or in alternance with -, the contraction of HE and EHT cells as they are
1926 progressing throughout the emergence and reducing contacting membrane surfaces along the
1927 longitudinal axis (the reduction in contacting membrane surfaces also involves membrane
1928 retrieval, hypothetically via endocytosis). Our data obtained with the CRISPR deletion mutants
1929 (a slight tendency to increase, on average, the turnover and mobile pool of these he-ec-ec
1930 junctions) suggest that ArhGEF11, in the wild type condition, should be slowing down the
1931 recycling of junctional components at tri-junctions, which hypothetically should contribute to
1932 increase adhesion strength. This may be required also to stabilize the junction-cytoskeleton
1933 interface involved in controlling the contraction/shrinkage of HE cells along the longitudinal
1934 axis, a hypothesis that is compatible with the mutant phenotype observed in this study, i.e the
1935 increase in frequency of more elongated HE cells and the decrease in HE cell progression
1936 throughout EHT (see ***Figure 7***); **2** (right cartoon, cyan arrow and bottom cartoons a-c), the

1937 intercalation of an endothelial cell to isolate 2 adjacent hemogenic cells or 2 daughter cells
1938 after mitosis (not depicted). This is mandatory for EHT progression and completion which
1939 requires adjoining endothelial cells to protrude membrane extensions that will anastomose to
1940 seal the aortic floor (see Lancino et al. 2018). The accumulation of adjoining cells of rather
1941 small length and apparently impaired in EHT progression that we describe in ***Figure*** 7 upon
1942 MO interference (that may also indicate impairment in abscission completion) suggests that
1943 the ArhGEF11 +exon 38 peptide encoding variant is more specifically involved in controlling
1944 the remodeling of the he/he interface that leads to endothelial cell intercalation (bottom
1945 cartoons, the remodeling of he-he-ec junctions is leading to he-ec-ec junctions and takes place
1946 between b and c). The increase in the recycling parameters that we measure in this interfering
1947 condition (mobile pool and early speed of recovery) indicates that the activity of ArhGEF11,
1948 and in particular of its +exon 38 peptide encoding variant, negatively controls junctional
1949 recycling. Hypothetically, the junctional adhesion strengthening triggered by reducing the
1950 recycling of junctional components at the he/he interface may be required during the early
1951 phase and progression of intercalation to support increase in membrane tension and
1952 environmental constraints (intercalation contributes to reducing the length/surface of the he/he
1953 membrane interface preceding junctional remodeling (cartoons b and c); this reducing
1954 membrane interface is in addition submitted to the shear stress imposed by blood flow).
1955

1956

1957

1958

References

Adamo, Luigi, Olaia Naveiras, Pamela L. Wenzel, Shannon McKinney-Freeman, Peter J. Mack, Jorge Gracia-Sancho, Astrid Suchy-Dicey, et al. 2009. "Biomechanical Forces Promote Embryonic Haematopoiesis." *Nature* 459 (7250): 1131–35. https://doi.org/10.1038/nature08073.

Akitake, Courtney M., Michelle Macurak, Marnie E. Halpern, and Mary G. Goll. 2011. "Transgenerational Analysis of Transcriptional Silencing in Zebrafish." *Developmental Biology* 352 (2): 191–201. https://doi.org/10.1016/j.ydbio.2011.01.002.

Barone, Cristiana, Roberto Orsenigo, Raffaella Meneveri, Silvia Brunelli, and Emanuele Azzoni. 2022. "One Size Does Not Fit All: Heterogeneity in Developmental Hematopoiesis." *Cells* 11 (6): 1061. https://doi.org/10.3390/cells11061061.

Bayless, Kayla J., and George E. Davis. 2002. "The Cdc42 and Rac1 GTPases Are Required for Capillary Lumen Formation in Three-Dimensional Extracellular Matrices." *Journal of Cell Science* 115 (6): 1123–36. https://doi.org/10.1242/jcs.115.6.1123.

Bengtsson, Henrik. 2022. *matrixStats: Functions That Apply to Rows and Columns of Matrices (and to Vectors)*. https://github.com/HenrikBengtsson/matrixStats.

Bengtsson, Henrik, Constantin Ahlmann-Eltze, Hector Corrada Bravo, Robert Gentleman, Jan Gleixner, Peter Hickey, Ola Hossjer, et al. 2023. "matrixStats: Functions That Apply to Rows and Columns of Matrices (and to Vectors)." https://cran.rstudio.com/web/packages/matrixStats/index.html.

Bertrand, Julien Y., Neil C. Chi, Buyung Santoso, Shutian Teng, Didier Y. R. Stainier, and David Traver. 2010. "Haematopoietic Stem Cells Derive Directly from Aortic Endothelium during Development." *Nature* 464 (7285): 108–11. https://doi.org/10.1038/nature08738.

Bertrand, Julien Y., Albert D. Kim, Emily P. Violette, David L. Stachura, Jennifer L. Cisson, and David Traver. 2007. "Definitive Hematopoiesis Initiates through a Committed Erythromyeloid Progenitor in the Zebrafish Embryo." *Development* 134 (23): 4147–56. https://doi.org/10.1242/dev.012385.

Boisset, Jean-Charles, Wiggert van Cappellen, Charlotte Andrieu-Soler, Niels Galjart, Elaine Dzierzak, and Catherine Robin. 2010. "In Vivo Imaging of Haematopoietic Cells Emerging from the Mouse Aortic Endothelium." *Nature* 464 (7285): 116–20. https://doi.org/10.1038/nature08764.

Bonkhofer, Florian, Rossella Rispoli, Philip Pinheiro, Monika Krecsmarik, Janina Schneider-Swales, Ingrid Ho Ching Tsang, Marella de Bruijn, Rui Monteiro, Tessa Peterkin, and Roger Patient. 2019. "Blood Stem Cell-Forming Haemogenic Endothelium in Zebrafish Derives from Arterial Endothelium." *Nature Communications* 10 (1): 3577. https://doi.org/10.1038/s41467-019-11423-2.

Bosveld, Floris, Zhimin Wang, and Yohanns Bellaïche. 2018. "Tricellular Junctions: A Hot Corner of Epithelial Biology." *Current Opinion in Cell Biology*, Cell Dynamics, 54 (October): 80–88. https://doi.org/10.1016/j.ceb.2018.05.002.

Bresciani, Erica, Elizabeth Broadbridge, and Paul P. Liu. 2018. "An Efficient Dissociation Protocol for Generation of Single Cell Suspension from Zebrafish Embryos and Larvae." *MethodsX* 5: 1287–90. https://doi.org/10.1016/j.mex.2018.10.009.

Bruijn, Marella F. T. R de, Xiaoqian Ma, Catherine Robin, Katrin Ottersbach, Maria-Jose Sanchez, and Elaine Dzierzak. 2002. "Hematopoietic Stem Cells Localize to the Endothelial Cell Layer in the Midgestation Mouse Aorta." *Immunity* 16 (5): 673–83. https://doi.org/10.1016/S1074-7613(02)00313-8.

Bryant, David M., Julie Roignot, Anirban Datta, Arend W. Overeem, Minji Kim, Wei Yu, Xiao Peng, et al. 2014. "A Molecular Switch for the Orientation of Epithelial Cell Polarization." *Developmental Cell* 31 (2): 171–87. https://doi.org/10.1016/j.devcel.2014.08.027.

Buckley, Clare E., and Daniel St Johnston. 2022. “Apical–Basal Polarity and the Control of Epithelial Form and Function.” *Nature Reviews Molecular Cell Biology* 23 (8): 559–77. https://doi.org/10.1038/s41580-022-00465-y.

Burns, Caroline Erter, Tony DeBlasio, Yi Zhou, Jin Zhang, Leonard Zon, and Stephen D Nimer. 2002. “Isolation and Characterization of Runxa and Runxb, Zebrafish Members of the Runt Family of Transcriptional Regulators.” *Experimental Hematology* 30 (12): 1381–89. https://doi.org/10.1016/S0301-472X(02)00955-4.

Butko, Emerald, Martin Distel, Claire Pouget, Bart Weijts, Isao Kobayashi, Kevin Ng, Christian Mosimann, et al. 2015. “Gata2b Is a Restricted Early Regulator of Hemogenic Endothelium in the Zebrafish Embryo.” *Development* 142 (6): 1050–61. https://doi.org/10.1242/dev.119180.

Campinho, Pedro, Paola Lamperti, Francesco Boselli, Andrej Vilfan, and Julien Vermot. 2020. “Blood Flow Limits Endothelial Cell Extrusion in the Zebrafish Dorsal Aorta.” *Cell Reports* 31 (2): 107505. https://doi.org/10.1016/j.celrep.2020.03.069.

Chalin, Dmitrii, Charlotte Bureau, Andrea Parmeggiani, Sergei Rochal, Karima Kissa, and Ivan Golushko. 2021. “Modeling and Live Imaging of Mechanical Instabilities in the Zebrafish Aorta during Hematopoiesis.” *Scientific Reports* 11 (1): 9316. https://doi.org/10.1038/s41598-021-88667-w.

Chi, Neil C., Robin M. Shaw, Sarah De Val, Guson Kang, Lily Y. Jan, Brian L. Black, and Didier Y. R. Stainier. 2008. “Foxn4 Directly Regulates Tbx2b Expression and Atrioventricular Canal Formation.” *Genes & Development* 22 (6): 734–39. https://doi.org/10.1101/gad.1629408.

Chikumi, Hiroki, Ana Barac, Babak Behbahani, Yuan Gao, Hidemi Teramoto, Yi Zheng, and J. Silvio Gutkind. 2004. “Homo- and Hetero-Oligomerization of PDZ-RhoGEF, LARG and p115RhoGEF by Their C-Terminal Region Regulates Their in Vivo Rho GEF Activity and Transforming Potential.” *Oncogene* 23 (1): 233–40. https://doi.org/10.1038/sj.onc.1207012.

Ciau-Uitz, Aldo, Rui Monteiro, Arif Kirmizitas, and Roger Patient. 2014. “Developmental Hematopoiesis: Ontogeny, Genetic Programming and Conservation.” *Experimental Hematology*, Genomics and Model Organisms: New Horizons for Experimental Hematology, 42 (8): 669–83. https://doi.org/10.1016/j.exphem.2014.06.001.

Clarke, Erik, and Scott Sherrill-Mix. 2017. *Ggbeeswarm: Categorical Scatter (Violin Point) Plots*. https://github.com/eclarke/ggbeeswarm.

Cumano, Ana, Françoise Dieterlen-Lievre, and Isabelle Godin. 1996. “Lymphoid Potential, Probed before Circulation in Mouse, Is Restricted to Caudal Intraembryonic Splanchnopleura.” *Cell* 86 (6): 907–16. https://doi.org/10.1016/S0092-8674(00)80166-X.

Daniel, Michael G., David Sachs, Jeffrey M. Bernitz, Yesai Fstkchyan, Katrina Rapp, Namita Satija, Kenneth Law, et al. 2019. “Induction of Human Hemogenesis in Adult Fibroblasts by Defined Factors and Hematopoietic Coculture.” *FEBS Letters* 593 (23): 3266–87. https://doi.org/10.1002/1873-3468.13621.

Davis, George E., Kayla J. Bayless, and Anil Mavila. 2002. “Molecular Basis of Endothelial Cell Morphogenesis in Three-Dimensional Extracellular Matrices.” *The Anatomical Record* 268 (3): 252–75. https://doi.org/10.1002/ar.10159.

De Chaumont, Fabrice, Stéphane Dallongeville, Nicolas Chenouard, Nicolas Hervé, Sorin Pop, Thomas Provoost, Vannary Meas-Yedid, et al. 2012. “Icy: An Open Bioimage Informatics Platform for Extended Reproducible Research.” *Nature Methods* 9 (7): 690–96. https://doi.org/10.1038/nmeth.2075.

Dignum, Tessa, Barbara Varnum-Finney, Sanjay R. Srivatsan, Stacey Dozono, Olivia Waltner, Adam M. Heck, Takashi Ishida, et al. 2021. “Multipotent Progenitors and Hematopoietic Stem Cells Arise Independently from Hemogenic Endothelium in the Mouse Embryo.” *Cell Reports* 36 (11): 109675. https://doi.org/10.1016/j.celrep.2021.109675.

Dufour, Alexandre, Roman Thibeaux, Elisabeth Labruyere, Nancy Guillen, and Jean-Christophe Olivo-Marin. 2011. "3-D Active Meshes: Fast Discrete Deformable Models for Cell Tracking in 3-D Time-Lapse Microscopy." *IEEE Transactions on Image Processing* 20 (7): 1925–37. https://doi.org/10.1109/TIP.2010.2099125.

Ebnet, Klaus. 2017. "Junctional Adhesion Molecules (JAMs): Cell Adhesion Receptors With Pleiotropic Functions in Cell Physiology and Development." *Physiological Reviews* 97 (4): 1529–54. https://doi.org/10.1152/physrev.00004.2017.

Ebnet, Klaus, Michel Aurrand-Lions, Annegret Kuhn, Friedemann Kiefer, Stefan Butz, Kerstin Zander, Maria-Katharina Meyer Zu Brickwedde, Atsushi Suzuki, Beat A. Imhof, and Dietmar Vestweber. 2003. "The Junctional Adhesion Molecule (JAM) Family Members JAM-2 and JAM-3 Associate with the Cell Polarity Protein PAR-3: A Possible Role for JAMs in Endothelial Cell Polarity." *Journal of Cell Science* 116 (19): 3879–91. https://doi.org/10.1242/jcs.00704.

Ebnet, Klaus, and Volker Gerke. 2022. "Rho and Rab Family Small GTPases in the Regulation of Membrane Polarity in Epithelial Cells." *Frontiers in Cell and Developmental Biology* 10. https://www.frontiersin.org/articles/10.3389/fcell.2022.948013.

Ebnet, Klaus, Daniel Kummer, Tim Steinbacher, Amrita Singh, Masanori Nakayama, and Maja Matis. 2018. "Regulation of Cell Polarity by Cell Adhesion Receptors." *Seminars in Cell & Developmental Biology*, Cell Polarity and Planar Cell Polarity Proteins, 81 (September): 2–12. https://doi.org/10.1016/j.semcdb.2017.07.032.

Ebnet, Klaus, Atsushi Suzuki, Yosuke Horikoshi, Tomonori Hirose, Maria-Katharina Meyer zu Brickwedde, Shigeo Ohno, and Dietmar Vestweber. 2001. "The Cell Polarity Protein ASIP/PAR-3 Directly Associates with Junctional Adhesion Molecule (JAM)." *The EMBO Journal* 20 (14): 3738–48. https://doi.org/10.1093/emboj/20.14.3738.

Eilken, Hanna M., Shin-Ichi Nishikawa, and Timm Schroeder. 2009. "Continuous Single-Cell Imaging of Blood Generation from Haemogenic Endothelium." *Nature* 457 (7231): 896–900. https://doi.org/10.1038/nature07760.

Farrell, Jeffrey A., Yiqun Wang, Samantha J. Riesenfeld, Karthik Shekhar, Aviv Regev, and Alexander F. Schier. 2018. "Single-Cell Reconstruction of Developmental Trajectories during Zebrafish Embryogenesis." Science 360 (6392): eaar3131. https://doi.org/10.1126/science.aar3131.

Frame, Jenna M., Katherine H. Fegan, Simon J. Conway, Kathleen E. McGrath, and James Palis. 2016. "Definitive Hematopoiesis in the Yolk Sac Emerges from Wnt-Responsive Hemogenic Endothelium Independently of Circulation and Arterial Identity." *Stem Cells* 34 (2): 431–44. https://doi.org/10.1002/stem.2213.

Gama-Norton, Leonor, Eva Ferrando, Cristina Ruiz-Herguido, Zhenyi Liu, Jordi Guiu, Abul B. M. M. K. Islam, Sung-Uk Lee, et al. 2015. "Notch Signal Strength Controls Cell Fate in the Haemogenic Endothelium." *Nature Communications* 6 (1): 8510. https://doi.org/10.1038/ncomms9510.

Ganuza, Miguel, Brandon Hadland, Ashley Chabot, Chen Li, Guolian Kang, Irwin Bernstein, and Shannon McKinney-Freeman. 2017. "Murine Hemogenic Endothelial Precursors Display Heterogeneous Hematopoietic Potential Ex Vivo." *Experimental Hematology* 51 (July): 25-35.e6. https://doi.org/10.1016/j.exphem.2017.04.006.

Gao, Long, Joanna Tober, Peng Gao, Changya Chen, Kai Tan, and Nancy A. Speck. 2018. "RUNX1 and the Endothelial Origin of Blood." *Experimental Hematology* 68 (December): 2–9. https://doi.org/10.1016/j.exphem.2018.10.009.

Garcia-Porrero, Juan A., Isabelle E. Godin, and Françoise Dieterlen-Lièvre. 1995. "Potential Intraembryonic Hemogenic Sites at Pre-Liver Stages in the Mouse." *Anatomy and Embryology* 192 (5): 425–35. https://doi.org/10.1007/BF00240375.

Garnier, Simon. 2021. *Viridis: Colorblind-Friendly Color Maps for R*. https://CRAN.R-project.org/package=viridis.

Garrido-Urbani, S., P. F. Bradfield, and B. A. Imhof. 2014. “Tight Junction Dynamics: The Role of Junctional Adhesion Molecules (JAMs).” *Cell and Tissue Research* 355 (3): 701–15. https://doi.org/10.1007/s00441-014-1820-1.

Ghosn, Eliver, Momoko Yoshimoto, Hiromitsu Nakauchi, Irving L. Weissman, and Leonore A. Herzenberg. 2019. “Hematopoietic Stem Cell-Independent Hematopoiesis and the Origins of Innate-like B Lymphocytes.” *Development* 146 (15): dev170571. https://doi.org/10.1242/dev.170571.

Grosjean, Philippe. 2019. *SciViews: SciViews - Main Package*. https://CRAN.R-project.org/package=SciViews.

Gudipaty, Swapna Aravind, and Jody Rosenblatt. 2017. “Epithelial Cell Extrusion: Pathways and Pathologies.” *Seminars in Cell & Developmental Biology*, Extracellular Vesicles, 67 (July): 132–40. https://doi.org/10.1016/j.semcdb.2016.05.010.

Hadland, Brandon, and Momoko Yoshimoto. 2018. “Many Layers of Embryonic Hematopoiesis: New Insights into B-Cell Ontogeny and the Origin of Hematopoietic Stem Cells.” *Experimental Hematology* 60 (April): 1–9. https://doi.org/10.1016/j.exphem.2017.12.008.

Herbert, Shane P., Jan Huisken, Tyson N. Kim, Morri E. Feldman, Benjamin T. Houseman, Rong A. Wang, Kevan M. Shokat, and Didier Y. R. Stainier. 2009. “Arterial-Venous Segregation by Selective Cell Sprouting: An Alternative Mode of Blood Vessel Formation.” *Science* 326 (5950): 294–98. https://doi.org/10.1126/science.1178577.

Herwig, Lukas, Yannick Blum, Alice Krudewig, Elin Ellertsdottir, Anna Lenard, Heinz-Georg Belting, and Markus Affolter. 2011. “Distinct Cellular Mechanisms of Blood Vessel Fusion in the Zebrafish Embryo.” *Current Biology* 21 (22): 1942–48. https://doi.org/10.1016/j.cub.2011.10.016.

Itoh, Masahiko. 2013. “ARHGEF11, a Regulator of Junction-Associated Actomyosin in Epithelial Cells.” *Tissue Barriers* 1 (2): e24221. https://doi.org/10.4161/tisb.24221.

Itoh, Masahiko, Derek C. Radisky, Masaaki Hashiguchi, and Hiroyuki Sugimoto. 2017. “The Exon 38-Containing ARHGEF11 Splice Isoform Is Differentially Expressed and Is Required for Migration and Growth in Invasive Breast Cancer Cells.” *Oncotarget* 8 (54): 92157–70. https://doi.org/10.18632/oncotarget.20985.

Itoh, Masahiko, Hiroyuki Sasaki, Mikio Furuse, Harunobu Ozaki, Toru Kita, and Shoichiro Tsukita. 2001. “Junctional Adhesion Molecule (JAM) Binds to PAR-3.” *Journal of Cell Biology* 154 (3): 491–98. https://doi.org/10.1083/jcb.200103047.

Itoh, Masahiko, Sachiko Tsukita, Yuji Yamazaki, and Hiroyuki Sugimoto. 2012. “Rho GTP Exchange Factor ARHGEF11 Regulates the Integrity of Epithelial Junctions by Connecting ZO-1 and RhoA-Myosin II Signaling.” *Proceedings of the National Academy of Sciences* 109 (25): 9905–10. https://doi.org/10.1073/pnas.1115063109.

Ivanovs, Andrejs, Stanislav Rybtsov, Elizabeth S. Ng, Edouard G. Stanley, Andrew G. Elefanty, and Alexander Medvinsky. 2017. “Human Haematopoietic Stem Cell Development: From the Embryo to the Dish.” *Development* 144 (13): 2323–37. https://doi.org/10.1242/dev.134866.

Ivanovs, Andrejs, Stanislav Rybtsov, Lindsey Welch, Richard A. Anderson, Marc L. Turner, and Alexander Medvinsky. 2011. “Highly Potent Human Hematopoietic Stem Cells First Emerge in the Intraembryonic Aorta-Gonad-Mesonephros Region.” *Journal of Experimental Medicine* 208 (12): 2417–27. https://doi.org/10.1084/jem.20111688.

Jabermoradi, Abbas, Suyeon Yang, Martijn I. Gobes, John P. M. van Duynhoven, and Johannes Hohlbein. 2022. “Enabling Single-Molecule Localization Microscopy in Turbid Food Emulsions.” *Philosophical Transactions of the Royal Society A: Mathematical, Physical and Engineering Sciences* 380 (2220): 20200164. https://doi.org/10.1098/rsta.2020.0164.

Jaffredo, Thierry, Rodolphe Gautier, Anne Eichmann, and Françoise Dieterlen-Lièvre. 1998. “Intraaortic Hemopoietic Cells Are Derived from Endothelial Cells during Ontogeny.” *Development* 125 (22): 4575–83. https://doi.org/10.1242/dev.125.22.4575.

Jaffredo, Thierry, and Laurent Yvernogeau. 2014. “How the Avian Model Has Pioneered the Field of Hematopoietic Development.” *Experimental Hematology*, Genomics and Model Organisms: New Horizons for Experimental Hematology, 42 (8): 661–68. https://doi.org/10.1016/j.exphem.2014.05.009.

Jin, Suk-Won, Dimitris Beis, Tracy Mitchell, Jau-Nian Chen, and Didier Y. R. Stainier. 2005. “Cellular and Molecular Analyses of Vascular Tube and Lumen Formation in Zebrafish.” *Development* 132 (23): 5199–5209. https://doi.org/10.1242/dev.02087.

Kalev-Zylinska, Maggie L., Julia A. Horsfield, Maria Vega C. Flores, John H. Postlethwait, Maria R. Vitas, Andrea M. Baas, Philip S. Crosier, and Kathryn E. Crosier. 2002. “Runx1 Is Required for Zebrafish Blood and Vessel Development and Expression of a Human RUNX1-CBF2T1 Transgene Advances a Model for Studies of Leukemogenesis.” *Development* 129 (8): 2015–30. https://doi.org/10.1242/dev.129.8.2015.

Kamei, Makoto, W. Brian Saunders, Kayla J. Bayless, Louis Dye, George E. Davis, and Brant M. Weinstein. 2006. “Endothelial Tubes Assemble from Intracellular Vacuoles in Vivo.” *Nature* 442 (7101): 453–56. https://doi.org/10.1038/nature04923.

Kassambara, Alboukadel. 2020. *Ggpubr: Ggplot2 Based Publication Ready Plots*. https://rpkgs.datanovia.com/ggpubr/.

Kataoka, Hiroko, Mitsuo Ochi, Koh-ichi Enomoto, and Akira Yamaguchi. 2000. “Cloning and Embryonic Expression Patterns of the Zebrafish Runt Domain Genes, Runxa and Runxb.” *Mechanisms of Development* 98 (1): 139–43. https://doi.org/10.1016/S0925-4773(00)00445-7.

Kimmel, Charles B., William W. Ballard, Seth R. Kimmel, Bonnie Ullmann, and Thomas F. Schilling. 1995. “Stages of Embryonic Development of the Zebrafish.” *Developmental Dynamics* 203 (3): 253–310. https://doi.org/10.1002/aja.1002030302.

Kissa, Karima, and Philippe Herbomel. 2010. “Blood Stem Cells Emerge from Aortic Endothelium by a Novel Type of Cell Transition.” *Nature* 464 (7285): 112–15. https://doi.org/10.1038/nature08761.

Kobayashi, Isao, Jingjing Kobayashi-Sun, Yuto Hirakawa, Madoka Ouchi, Koyuki Yasuda, Hiroyasu Kamei, Shigetomo Fukuhara, and Masaaki Yamaguchi. 2020. “Dual Role of Jam3b in Early Hematopoietic and Vascular Development.” *Development* 147 (1): dev181040. https://doi.org/10.1242/dev.181040.

Lagendijk, Anne Karine, Alpha S Yap, and Benjamin M Hogan. 2014. “Endothelial Cell–Cell Adhesion during Zebrafish Vascular Development.” *Cell Adhesion & Migration* 8 (2): 136–45. https://doi.org/10.4161/cam.28229.

Lancino, Mylene, Sara Majello, Sebastien Herbert, Fabrice De Chaumont, Jean-Yves Tinevez, Jean-Christophe Olivo-Marin, Philippe Herbomel, and Anne Schmidt. 2018. “Anisotropic Organization of Circumferential Actomyosin Characterizes Hematopoietic Stem Cells Emergence in the Zebrafish.” *eLife* 7 (August): e37355. https://doi.org/10.7554/eLife.37355.

Lancrin, Christophe, Milena Mazan, Monika Stefanska, Rahima Patel, Monika Lichtinger, Guilherme Costa, Özge Vargel, et al. 2012. “GFI1 and GFI1B Control the Loss of Endothelial Identity of Hemogenic Endothelium during Hematopoietic Commitment.” *Blood* 120 (2): 314–22. https://doi.org/10.1182/blood-2011-10-386094.

Lee, SungKyoung, Benjamin Cieply, Yueqin Yang, Natoya Peart, Carl Glaser, Patricia Chan, and Russ P. Carstens. 2018. “Esrp1-Regulated Splicing of Arhgef11 Isoforms Is Required for Epithelial Tight Junction Integrity.” *Cell Reports* 25 (9): 2417-2430.e5. https://doi.org/10.1016/j.celrep.2018.10.097.

Legland, David, Ignacio Arganda-Carreras, and Philippe Andrey. 2016. “MorphoLibJ: Integrated Library and Plugins for Mathematical Morphology with ImageJ.” *Bioinformatics* 32 (22): 3532–34. https://doi.org/10.1093/bioinformatics/btw413.

Liao, Wayne, Brent W. Bisgrove, Holly Sawyer, Barbara Hug, Bridgit Bell, Kevin Peters, David J. Grunwald, and Didier Y. R. Stainier. 1997. “The Zebrafish Gene Cloche Acts

Upstream of a Flk-1 Homologue to Regulate Endothelial Cell Differentiation." *Development* 124 (2): 381–89. https://doi.org/10.1242/dev.124.2.381.

Lie-A-Ling, Michael, Elli Marinopoulou, Yaoyong Li, Rahima Patel, Monika Stefanska, Constanze Bonifer, Crispin Miller, Valerie Kouskoff, and Georges Lacaud. 2014. "RUNX1 Positively Regulates a Cell Adhesion and Migration Program in Murine Hemogenic Endothelium Prior to Blood Emergence." *Blood* 124 (11): e11–20. https://doi.org/10.1182/blood-2014-04-572958.

Lin, Hui-Feng, David Traver, Hao Zhu, Kimberly Dooley, Barry H. Paw, Leonard I. Zon, and Robert I. Handin. 2005. "Analysis of Thrombocyte Development in CD41-GFP Transgenic Zebrafish." *Blood* 106 (12): 3803–10. https://doi.org/10.1182/blood-2005-01-0179.

Lundin, Vanessa, Wade W. Sugden, Lindsay N. Theodore, Patricia M. Sousa, Areum Han, Stephanie Chou, Paul J. Wrighton, et al. 2020. "YAP Regulates Hematopoietic Stem Cell Formation in Response to the Biomechanical Forces of Blood Flow." *Developmental Cell* 52 (4): 446-460.e5. https://doi.org/10.1016/j.devcel.2020.01.006.

Mack, Natalie Ann, and Marios Georgiou. 2014. "The Interdependence of the Rho GTPases and Apicobasal Cell Polarity." *Small GTPases* 5 (2): e973768. https://doi.org/10.4161/21541248.2014.973768.

Manoli, Martha, and Wolfgang Driever. 2012. "Fluorescence-Activated Cell Sorting (FACS) of Fluorescently Tagged Cells from Zebrafish Larvae for RNA Isolation." *Cold Spring Harbor Protocols* 2012 (8): pdb.prot069633. https://doi.org/10.1101/pdb.prot069633.

Marshall, Caroline J., and Adrian J. Thrasher. 2001. "The Embryonic Origins of Human Haematopoiesis." *British Journal of Haematology* 112 (4): 838–50. https://doi.org/10.1046/j.1365-2141.2001.02537.x.

Meder, Doris, Anna Shevchenko, Kai Simons, and Joachim Füllekrug. 2005. "Gp135/Podocalyxin and NHERF-2 Participate in the Formation of a Preapical Domain during Polarization of MDCK Cells." *Journal of Cell Biology* 168 (2): 303–13. https://doi.org/10.1083/jcb.200407072.

Medvinsky, Alexander, and Elaine Dzierzak. 1996. "Definitive Hematopoiesis Is Autonomously Initiated by the AGM Region." *Cell* 86 (6): 897–906. https://doi.org/10.1016/S0092-8674(00)80165-8.

Medvinsky, Alexander L., Nina L. Samoylina, Albrecht M. Müller, and Elaine A. Dzierzak. 1993. "An Early Pre-Liver Intraembryonic Source of CFU-S in the Developing Mouse." *Nature* 364 (6432): 64–67. https://doi.org/10.1038/364064a0.

Monteiro, Rui, Philip Pinheiro, Nicola Joseph, Tessa Peterkin, Jana Koth, Emmanouela Repapi, Florian Bonkhofer, Arif Kirmizitas, and Roger Patient. 2016. "Transforming Growth Factor β Drives Hemogenic Endothelium Programming and the Transition to Hematopoietic Stem Cells." *Developmental Cell* 38 (4): 358–70. https://doi.org/10.1016/j.devcel.2016.06.024.

Moreno-Mateos, Miguel A., Charles E. Vejnar, Jean-Denis Beaudoin, Juan P. Fernandez, Emily K. Mis, Mustafa K. Khokha, and Antonio J. Giraldez. 2015. "CRISPRscan: Designing Highly Efficient sgRNAs for CRISPR-Cas9 Targeting in Vivo." *Nature Methods* 12 (10): 982–88. https://doi.org/10.1038/nmeth.3543.

Müller, A. M., A. Medvinsky, J. Strouboulis, F. Grosveld, and E. Dzierzak. 1994. "Development of Hematopoietic Stem Cell Activity in the Mouse Embryo." *Immunity* 1 (4): 291–301. https://doi.org/10.1016/1074-7613(94)90081-7.

Murayama, Emi, Karima Kissa, Agustin Zapata, Elodie Mordelet, Valérie Briolat, Hui-Feng Lin, Robert I. Handin, and Philippe Herbomel. 2006. "Tracing Hematopoietic Precursor Migration to Successive Hematopoietic Organs during Zebrafish Development." *Immunity* 25 (6): 963–75. https://doi.org/10.1016/j.immuni.2006.10.015.

Nielsen, Julie S., and Kelly M. McNagny. 2008. "Novel Functions of the CD34 Family." *Journal of Cell Science* 121 (22): 3683–92. https://doi.org/10.1242/jcs.037507.

Nieto, M. Angela, Ruby Yun-Ju Huang, Rebecca A. Jackson, and Jean Paul Thiery. 2016. "EMT: 2016." *Cell* 166 (1): 21–45. https://doi.org/10.1016/j.cell.2016.06.028.

Nishimura, Tamako, Hisao Honda, and Masatoshi Takeichi. 2012. "Planar Cell Polarity Links Axes of Spatial Dynamics in Neural-Tube Closure." *Cell* 149 (5): 1084–97. https://doi.org/10.1016/j.cell.2012.04.021.

North, Trista E., Marella F. T. R. de Bruijn, Terryl Stacy, Laleh Talebian, Evan Lind, Catherine Robin, Michael Binder, Elaine Dzierzak, and Nancy A. Speck. 2002. "Runx1 Expression Marks Long-Term Repopulating Hematopoietic Stem Cells in the Midgestation Mouse Embryo." *Immunity* 16 (5): 661–72. https://doi.org/10.1016/S1074-7613(02)00296-0.

North, Trista E., Wolfram Goessling, Marian Peeters, Pulin Li, Craig Ceol, Allegra M. Lord, Gerhard J. Weber, et al. 2009. "Hematopoietic Stem Cell Development Is Dependent on Blood Flow." *Cell* 137 (4): 736–48. https://doi.org/10.1016/j.cell.2009.04.023.

North, Trista, Ting-Lei Gu, Terryl Stacy, Qing Wang, Louisa Howard, Michael Binder, Miguel Marín-Padilla, and Nancy A. Speck. 1999. "*Cbfa2* Is Required for the Formation of Intra-Aortic Hematopoietic Clusters." *Development* 126 (11): 2563–75. https://doi.org/10.1242/dev.126.11.2563.

Olayioye, Monilola A., Bettina Noll, and Angelika Hausser. 2019. "Spatiotemporal Control of Intracellular Membrane Trafficking by Rho GTPases." *Cells* 8 (12): 1478. https://doi.org/10.3390/cells8121478.

Orkin, Stuart H., and Leonard I. Zon. 2008. "Hematopoiesis: An Evolving Paradigm for Stem Cell Biology." *Cell* 132 (4): 631–44. https://doi.org/10.1016/j.cell.2008.01.025.

Padfield, Daniel, and Granville Matheson. 2020. *Nls.Multstart: Robust Non-Linear Regression Using AIC Scores*. https://CRAN.R-project.org/package=nls.multstart.

Patil, Indrajeet. 2022. *Ggstatsplot: Ggplot2 Based Plots with Statistical Details*. https://CRAN.R-project.org/package=ggstatsplot.

Pei, Duanqing, Xiaodong Shu, Ama Gassama-Diagne, and Jean Paul Thiery. 2019. "Mesenchymal–Epithelial Transition in Development and Reprogramming." *Nature Cell Biology* 21 (1): 44–53. https://doi.org/10.1038/s41556-018-0195-z.

Pradella, Davide, Chiara Naro, Claudio Sette, and Claudia Ghigna. 2017. "EMT and Stemness: Flexible Processes Tuned by Alternative Splicing in Development and Cancer Progression." *Molecular Cancer* 16 (1): 8. https://doi.org/10.1186/s12943-016-0579-2.

Ram, Karthik, and Hadley Wickham. 2018. *Wesanderson: A Wes Anderson Palette Generator*. https://github.com/karthik/wesanderson.

Ridley, Anne J. 2006. "Rho GTPases and Actin Dynamics in Membrane Protrusions and Vesicle Trafficking." *Trends in Cell Biology*, Membrane Dynamics, 16 (10): 522–29. https://doi.org/10.1016/j.tcb.2006.08.006.

Robert-Moreno, Àlex, Jordi Guiu, Cristina Ruiz-Herguido, M. Eugenia López, Julia Inglés-Esteve, Lluis Riera, Alex Tipping, et al. 2008. "Impaired Embryonic Haematopoiesis yet Normal Arterial Development in the Absence of the Notch Ligand Jagged1." *The EMBO Journal* 27 (13): 1886–95.

Rodriguez-Boulan, Enrique, Anne Müsch, and Andre Le Bivic. 2004. "Epithelial Trafficking: New Routes to Familiar Places." *Current Opinion in Cell Biology* 16 (4): 436–42. https://doi.org/10.1016/j.ceb.2004.06.013.

Román-Fernández, Alvaro, and David M. Bryant. 2016. "Complex Polarity: Building Multicellular Tissues Through Apical Membrane Traffic." *Traffic* 17 (12): 1244–61. https://doi.org/10.1111/tra.12417.

Rossman, Kent L., Channing J. Der, and John Sondek. 2005. "GEF Means Go: Turning on RHO GTPases with Guanine Nucleotide-Exchange Factors." *Nature Reviews Molecular Cell Biology* 6 (2): 167–80. https://doi.org/10.1038/nrm1587.

Samsa, Leigh Ann, Nicole Fleming, Scott Magness, Li Qian, and Jiandong Liu. 2016. "Isolation and Characterization of Single Cells from Zebrafish Embryos." *Journal of Visualized Experiments*, no. 109 (March): 53877. https://doi.org/10.3791/53877.

Sato, Yuki, Mugiho Shigematsu, Maria Shibata-Kanno, Sho Maejima, Chie Tamura, and Hirotaka Sakamoto. 2023. “Aquaporin Regulates Cell Rounding through Vacuole Formation during Endothelial-to-Hematopoietic Transition.” *Development* 150 (11): dev201275. https://doi.org/10.1242/dev.201275.

Sehnert, Amy J., Anja Huq, Brant M. Weinstein, Charline Walker, Mark Fishman, and Didier Y. R. Stainier. 2002. “Cardiac Troponin T Is Essential in Sarcomere Assembly and Cardiac Contractility.” *Nature Genetics* 31 (1): 106–10. https://doi.org/10.1038/ng875.

Shapiro, Irina M., Albert W. Cheng, Nicholas C. Flytzanis, Michele Balsamo, John S. Condeelis, Maja H. Oktay, Christopher B. Burge, and Frank B. Gertler. 2011. “An EMT–Driven Alternative Splicing Program Occurs in Human Breast Cancer and Modulates Cellular Phenotype.” *PLOS Genetics* 7 (8): e1002218. https://doi.org/10.1371/journal.pgen.1002218.

Sood, Raman, Milton A. English, Christiane L. Belele, Hao Jin, Kevin Bishop, Rebecca Haskins, Mary Cathleen McKinney, et al. 2010. “Development of Multilineage Adult Hematopoiesis in the Zebrafish with a Runx1 Truncation Mutation.” *Blood* 115 (14): 2806–9. https://doi.org/10.1182/blood-2009-08-236729.

Staneva, Ralitza, and Romain Levayer. 2023. “Chapter Five - Cell Polarity and Extrusion: How to Polarize Extrusion and Extrude Misspolarized Cells?” In *Current Topics in Developmental Biology*, edited by ULRICH Tepass, 154:131–67. Cell Polarity in Development and Disease. Academic Press. https://doi.org/10.1016/bs.ctdb.2023.02.010.

Strilić, Boris, Jan Eglinger, Michael Krieg, Martin Zeeb, Jennifer Axnick, Pavel Babál, Daniel J. Müller, and Eckhard Lammert. 2010. “Electrostatic Cell-Surface Repulsion Initiates Lumen Formation in Developing Blood Vessels.” *Current Biology* 20 (22): 2003–9. https://doi.org/10.1016/j.cub.2010.09.061.

Strilić, Boris, Tomáš Kučera, Jan Eglinger, Michael R. Hughes, Kelly M. McNagny, Sachiko Tsukita, Elisabetta Dejana, Napoleone Ferrara, and Eckhard Lammert. 2009. “The Molecular Basis of Vascular Lumen Formation in the Developing Mouse Aorta.” *Developmental Cell* 17 (4): 505–15. https://doi.org/10.1016/j.devcel.2009.08.011.

Sur, Abhinav, Yiqun Wang, Paulina Capar, Gennady Margolin, Morgan Kathleen Prochaska, and Jeffrey A. Farrell. 2023. “Single-Cell Analysis of Shared Signatures and Transcriptional Diversity during Zebrafish Development.” Developmental Cell 58 (24): 3028-3047.e12. https://doi.org/10.1016/j.devcel.2023.11.001.

Suster, Maximiliano L., Gembu Abe, Anders Schouw, and Koichi Kawakami. 2011. “Transposon-Mediated BAC Transgenesis in Zebrafish.” *Nature Protocols* 6 (12): 1998–2021. https://doi.org/10.1038/nprot.2011.416.

Swiers, Gemma, Claudia Baumann, John O’Rourke, Eleni Giannoulatou, Stephen Taylor, Anagha Joshi, Victoria Moignard, et al. 2013. “Early Dynamic Fate Changes in Haemogenic Endothelium Characterized at the Single-Cell Level.” *Nature Communications* 4 (1): 2924. https://doi.org/10.1038/ncomms3924.

Tian, Ye, Jin Xu, Shachuan Feng, Sicong He, Shizheng Zhao, Lu Zhu, Wan Jin, et al. 2017. “The First Wave of T Lymphopoiesis in Zebrafish Arises from Aorta Endothelium Independent of Hematopoietic Stem Cells.” *Journal of Experimental Medicine* 214 (11): 3347–60. https://doi.org/10.1084/jem.20170488.

Weijts, Bart, Laurent Yvernogeau, and Catherine Robin. 2021. “Recent Advances in Developmental Hematopoiesis: Diving Deeper With New Technologies.” *Frontiers in Immunology* 12. https://www.frontiersin.org/articles/10.3389/fimmu.2021.790379.

Wickham, Hadley. 2016. *Ggplot2: Elegant Graphics for Data Analysis*. Springer-Verlag New York. https://ggplot2.tidyverse.org.

Wickham, Hadley. 2022. *Stringr: Simple, Consistent Wrappers for Common String Operations*. https://CRAN.R-project.org/package=stringr.

Wickham, Hadley, Romain François, Lionel Henry, Kirill Müller, and Davis Vaughan. 2023. *Dplyr: A Grammar of Data Manipulation*. https://CRAN.R-project.org/package=dplyr.

Wickham, Hadley, Jim Hester, and Jennifer Bryan. 2022. *Readr: Read Rectangular Text Data*. https://CRAN.R-project.org/package=readr.

Wilke, Claus O. 2020. *Cowplot: Streamlined Plot Theme and Plot Annotations for Ggplot2*. https://wilkelab.org/cowplot/.

Wu, Yinyu, and Karen K. Hirschi. 2021. "Regulation of Hemogenic Endothelial Cell Development and Function." *Annual Review of Physiology* 83 (February): 17–37. https://doi.org/10.1146/annurev-physiol-021119-034352.

Xia, Jun, Mengyao Liu, Caiying Zhu, Shicheng Liu, Lanlan Ai, Dongyuan Ma, Ping Zhu, Lu Wang, and Feng Liu. 2023. "Activation of Lineage Competence in Hemogenic Endothelium Precedes the Formation of Hematopoietic Stem Cell Heterogeneity." *Cell Research*, April, 1–16. https://doi.org/10.1038/s41422-023-00797-0.

Xiao, Nan. 2018. *Ggsci: Scientific Journal and Sci-Fi Themed Color Palettes for Ggplot2*. https://CRAN.R-project.org/package=ggsci.

Xie, Yihui, Joe Cheng, and Xianying Tan. 2022. *DT: A Wrapper of the JavaScript Library DataTables*. https://github.com/rstudio/DT.

Yoshimoto, Momoko, Encarnacion Montecino-Rodriguez, Michael J. Ferkowicz, Prashanth Porayette, W. Christopher Shelley, Simon J. Conway, Kenneth Dorshkind, and Mervin C. Yoder. 2011. "Embryonic Day 9 Yolk Sac and Intra-Embryonic Hemogenic Endothelium Independently Generate a B-1 and Marginal Zone Progenitor Lacking B-2 Potential." *Proceedings of the National Academy of Sciences* 108 (4): 1468–73. https://doi.org/10.1073/pnas.1015841108.

Yoshimoto, Momoko, Prashanth Porayette, Nicole L. Glosson, Simon J. Conway, Nadia Carlesso, Angelo A. Cardoso, Mark H. Kaplan, and Mervin C. Yoder. 2012. "Autonomous Murine T-Cell Progenitor Production in the Extra-Embryonic Yolk Sac before HSC Emergence." *Blood* 119 (24): 5706–14. https://doi.org/10.1182/blood-2011-12-397489.

Zhao, Shizheng, Shachuan Feng, Ye Tian, and Zilong Wen. 2022. "Hemogenic and Aortic Endothelium Arise from a Common Hemogenic Angioblast Precursor and Are Specified by the Etv2 Dosage." *Proceedings of the National Academy of Sciences* 119 (13): e2119051119. https://doi.org/10.1073/pnas.2119051119.

Zhu, Qin, Peng Gao, Joanna Tober, Laura Bennett, Changya Chen, Yasin Uzun, Yan Li, et al. 2020. "Developmental Trajectory of Prehematopoietic Stem Cell Formation from Endothelium." *Blood* 136 (7): 845–56. https://doi.org/10.1182/blood.2020004801.

Figure 1

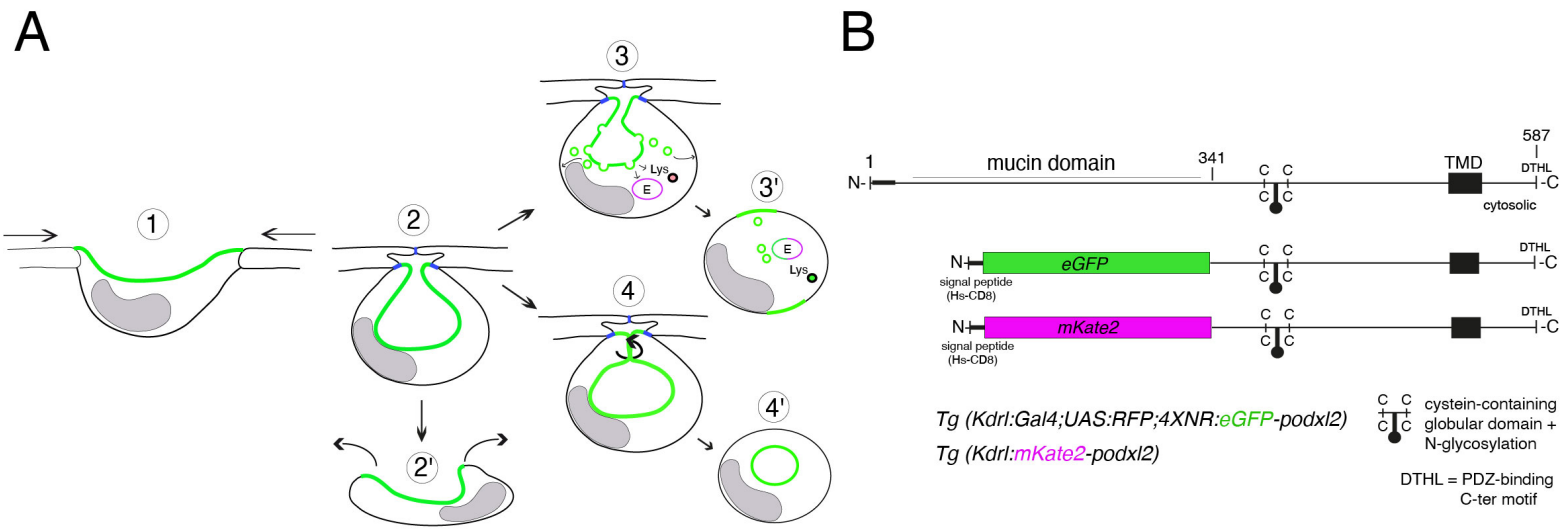
A
1
2
2'
3
3'
4
4'
Lys
E
B
1
N-
mucin domain
341
C C
C C
TMD
587
DTHL
-C
cytosolic
N-
eGFP
signal peptide
(Hs-CD8)
mKate2
Tg (Kdrl:Gal4;UAS:RFP;4XNR:eGFP-podxl2)
Tg (Kdrl:mKate2-podxl2)
cystein-containing
globular domain +
N-glycosylation
DTHL = PDZ-binding
C-ter motif

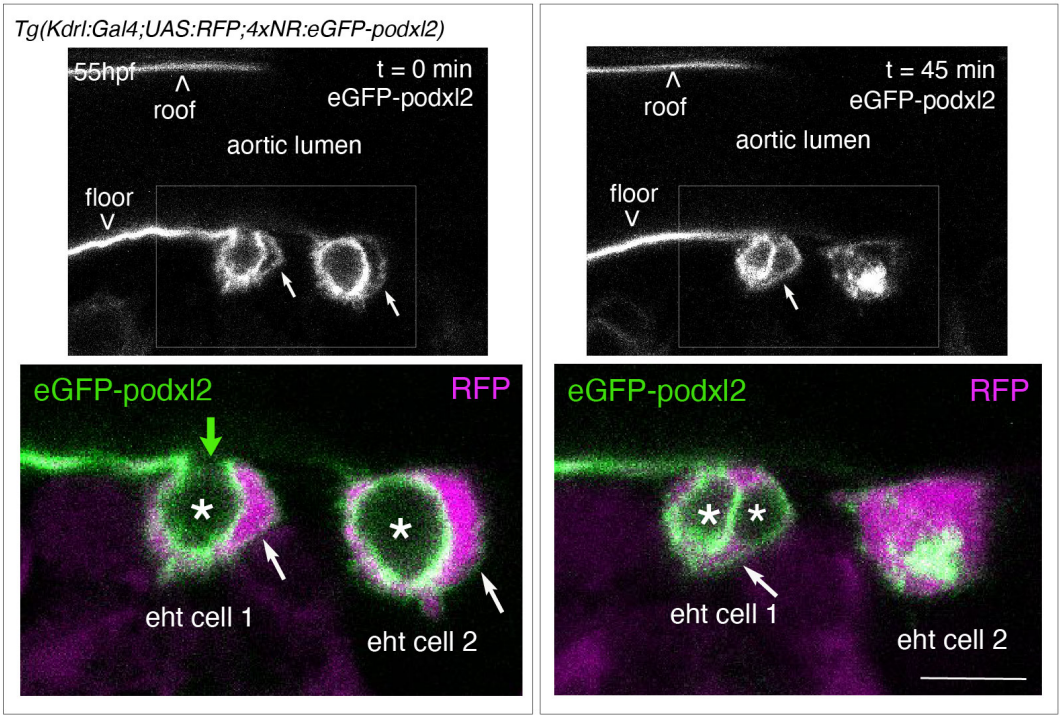
C
Tg(Kdrl:Gal4;UAS:RFP;4xNR:eGFP-podxl2)
55hpf
t = 0 min
eGFP-podxl2
roof
aortic lumen
floor
t = 45 min
eGFP-podxl2
eGFP-podxl2
RFP
eht cell 1
eht cell 2

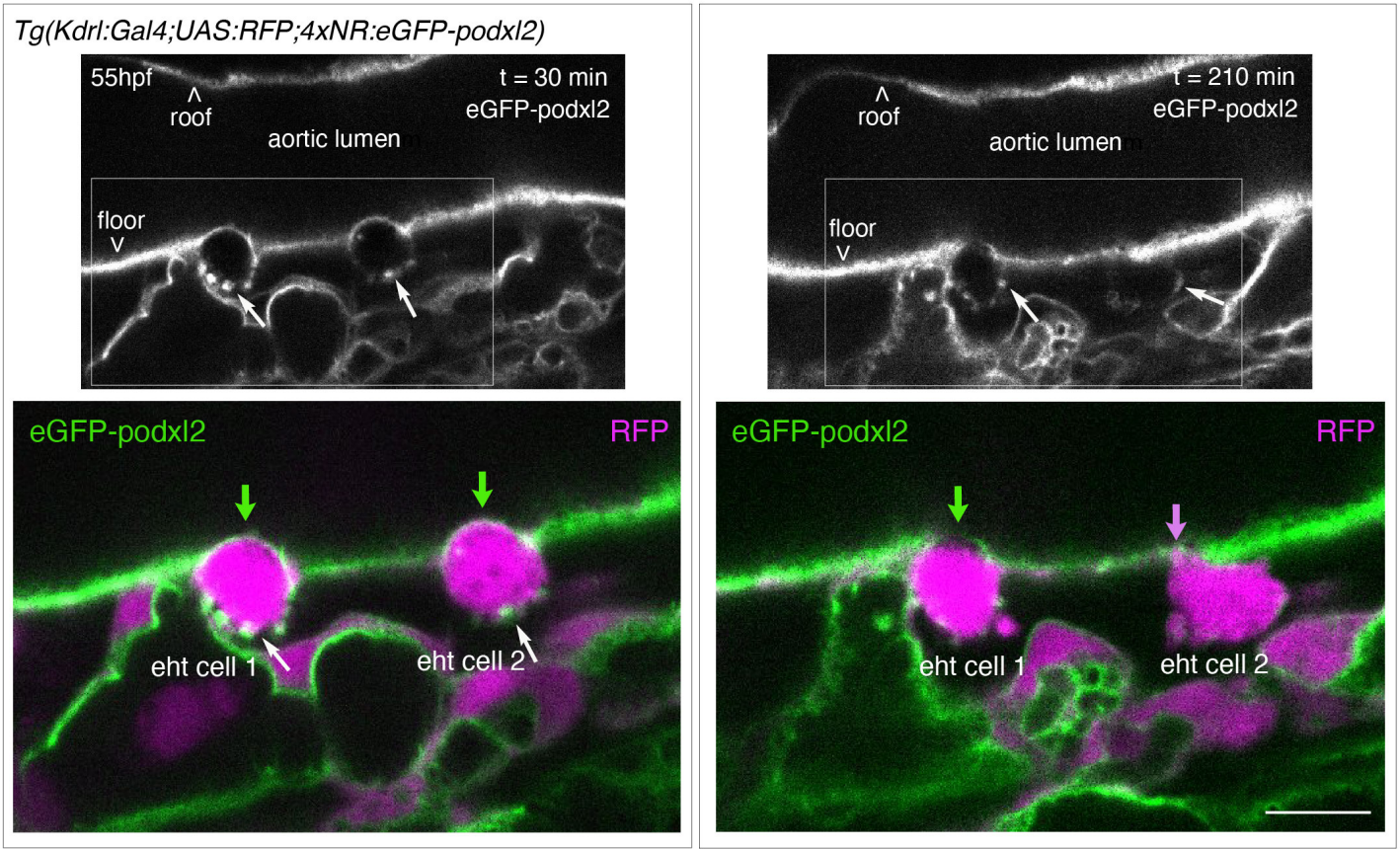
D
Tg(Kdrl:Gal4;UAS:RFP;4xNR:eGFP-podxl2)
55hpf
t = 30 min
eGFP-podxl2
roof
aortic lumen
floor
t = 210 min
eGFP-podxl2
eGFP-podxl2
RFP
eht cell 1
eht cell 2

Figure 2

A *Tg(Kdrl:Gal4;UAS:RFP;4xNR:eGFP-podxl2)*

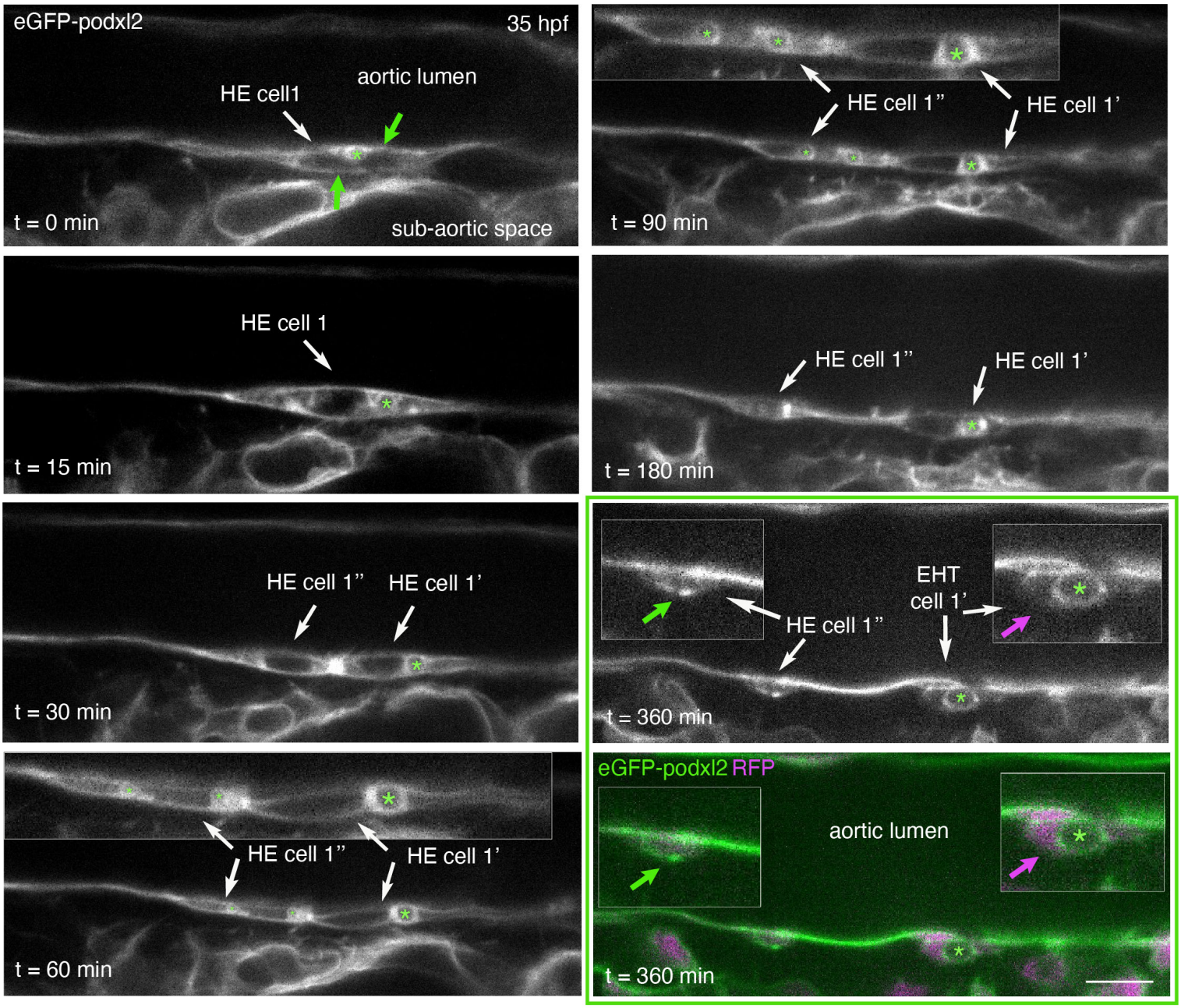

B

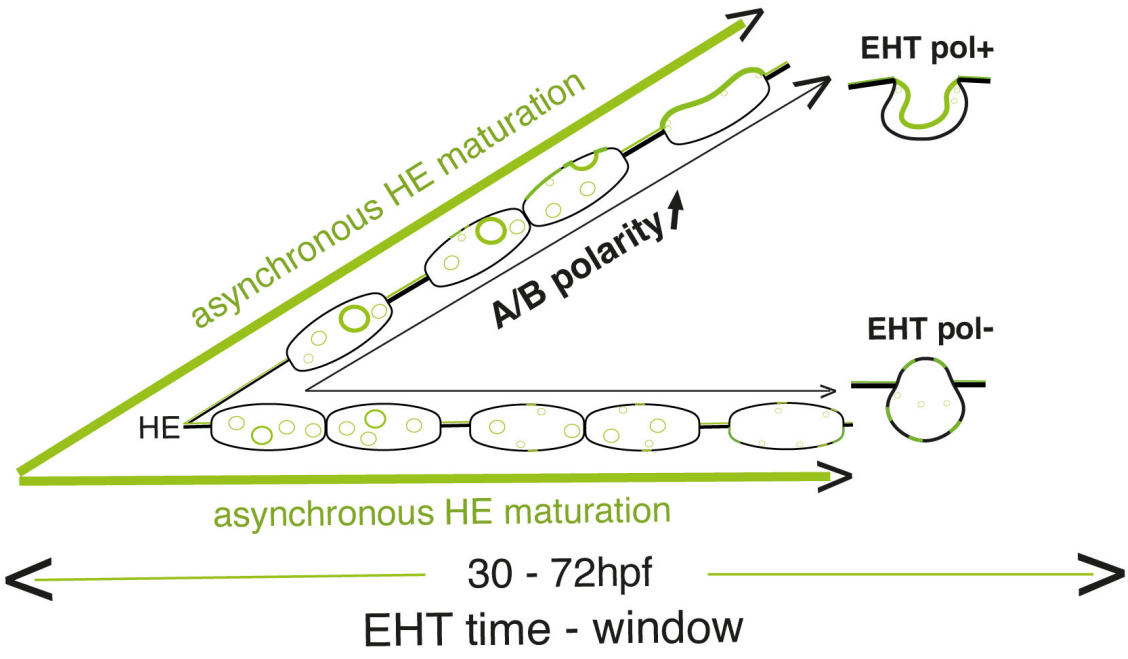

Figure 3

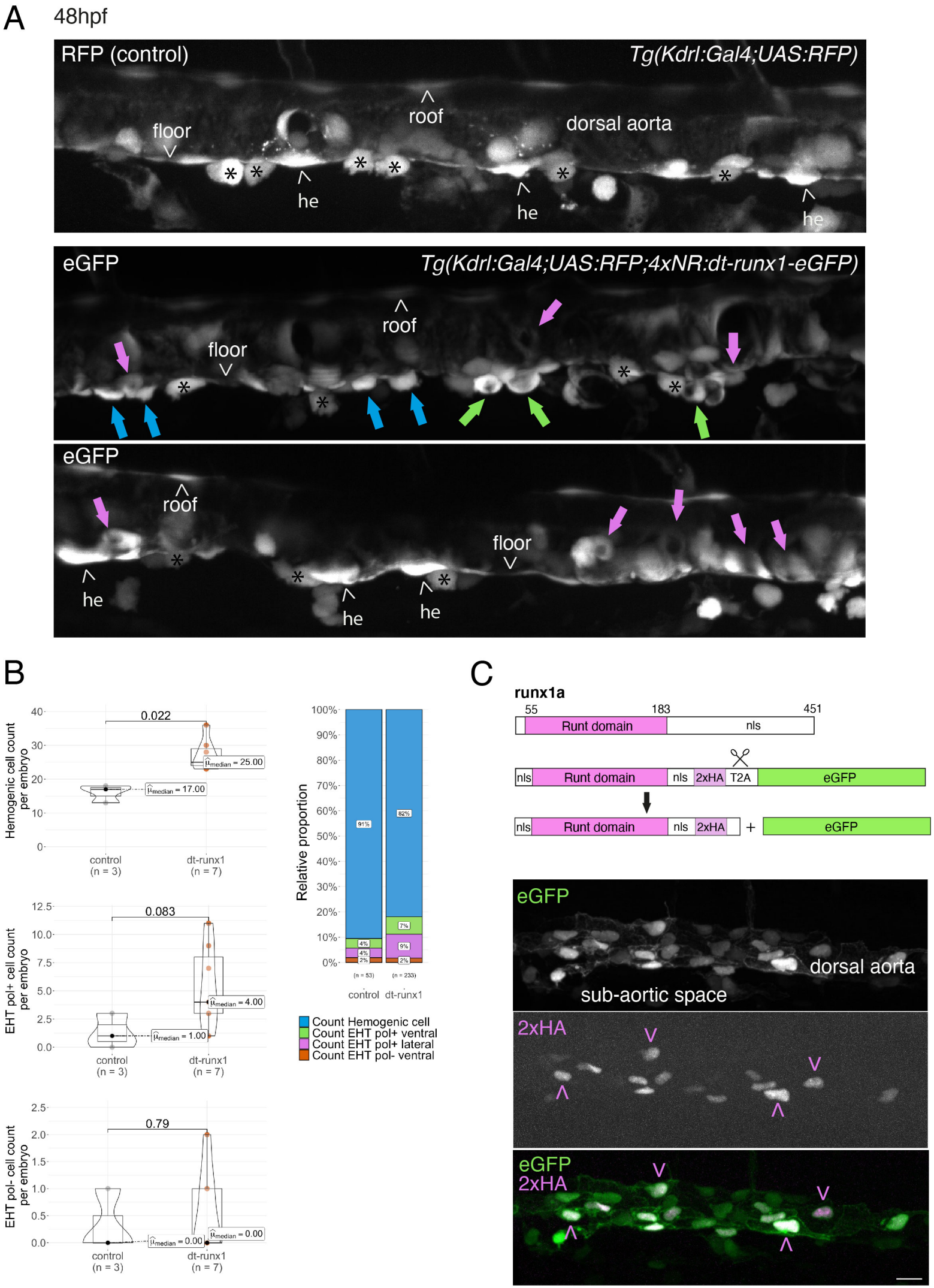
A
48hpf
RFP (control)
Tg(Kdrl:Gal4;UAS:RFP)
roof
floor
dorsal aorta
he
he
he
eGFP
Tg(Kdrl:Gal4;UAS:RFP;4xNR:dt-runx1-eGFP)
roof
floor
eGFP
roof
floor
he
he
he
B
Hemogenic cell count per embryo
0.022
μmedian = 25.00
μmedian = 17.00
control (n = 3)
dt-runx1 (n = 7)
EHT pol+ cell count per embryo
0.083
μmedian = 4.00
μmedian = 1.00
EHT pol- cell count per embryo
0.79
μmedian = 0.00
μmedian = 0.00
Relative proportion
91%
82%
7%
9%
4%
4%
2%
2%
(n = 53)
(n = 233)
control
dt-runx1
Count Hemogenic cell
Count EHT pol+ ventral
Count EHT pol+ lateral
Count EHT pol- ventral
C
runx1a
55
183
451
Runt domain
nls
nls
Runt domain
nls
2xHA
T2A
eGFP
nls
Runt domain
nls
2xHA
+
eGFP
eGFP
dorsal aorta
sub-aortic space
2xHA
eGFP
2xHA

Figure 4

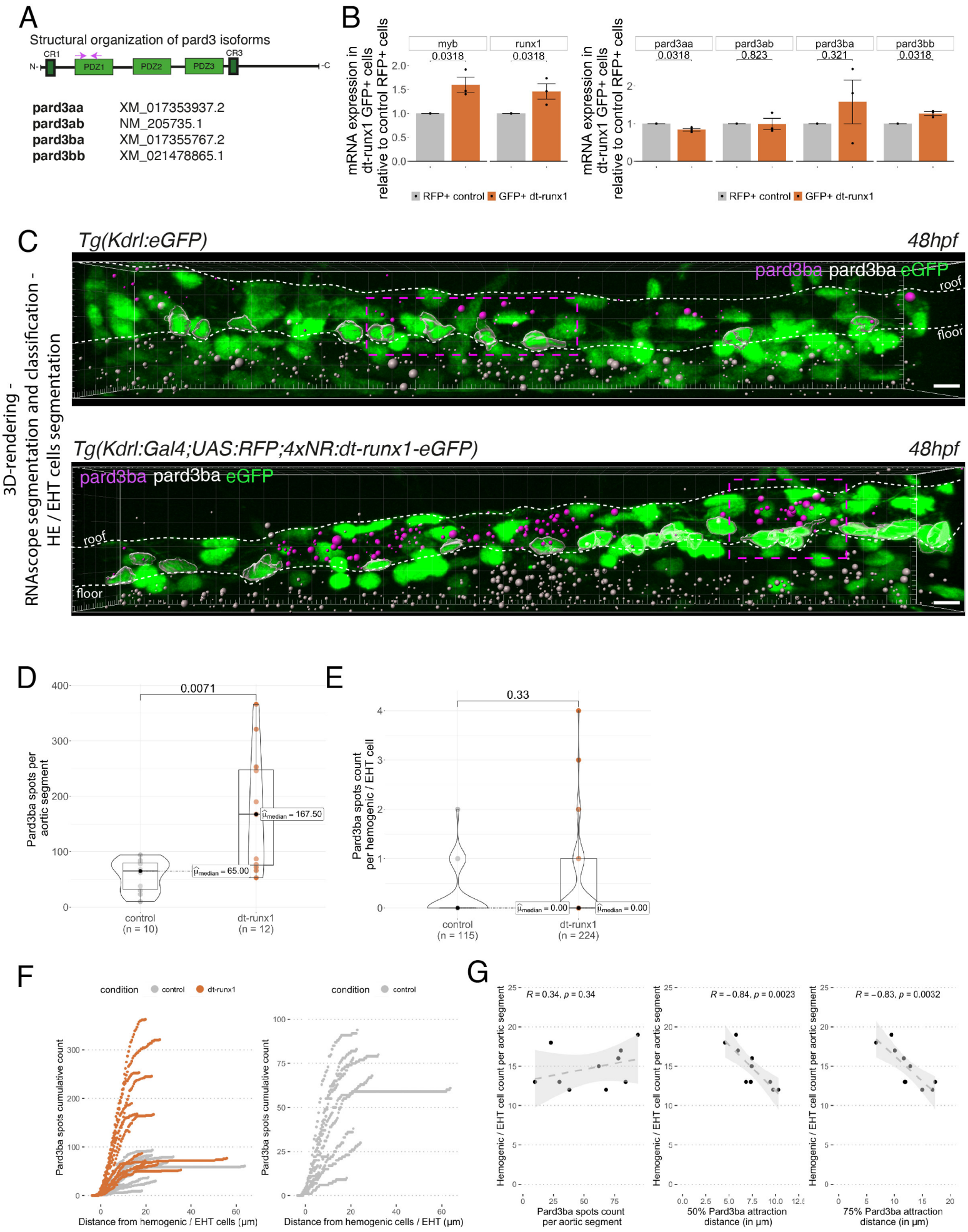
A
Structural organization of pard3 isoforms
CR1
CR3
N-
PDZ1
PDZ2
PDZ3
-C
pard3aa XM_017353937.2
pard3ab NM_205735.1
pard3ba XM_017355767.2
pard3bb XM_021478865.1
B
mRNA expression in dt-runx1 GFP+ cells relative to control RFP+ cells
myb 0.0318
runx1 0.0318
pard3aa 0.0318
pard3ab 0.823
pard3ba 0.321
pard3bb 0.0318
RFP+ control
GFP+ dt-runx1
C
3D-rendering - RNAscope segmentation and classification - HE / EHT cells segmentation
Tg(Kdrl:eGFP)
48hpf
pard3ba pard3ba eGFP
roof
floor
Tg(Kdrl:Gal4;UAS:RFP;4xNR:dt-runx1-eGFP)
48hpf
pard3ba pard3ba eGFP
roof
floor
D
0.0071
Pard3ba spots per aortic segment
$\hat{\mu}_{median}$ = 167.50
$\hat{\mu}_{median}$ = 65.00
control (n = 10)
dt-runx1 (n = 12)
E
0.33
Pard3ba spots count per hemogenic / EHT cell
$\hat{\mu}_{median}$ = 0.00
$\hat{\mu}_{median}$ = 0.00
control (n = 115)
dt-runx1 (n = 224)
F
condition control dt-runx1
Pard3ba spots cumulative count
Distance from hemogenic / EHT cells (µm)
condition control
Pard3ba spots cumulative count
Distance from hemogenic cells / EHT (µm)
G
R = 0.34, p = 0.34
R = −0.84, p = 0.0023
R = −0.83, p = 0.0032
Hemogenic / EHT cell count per aortic segment
Pard3ba spots count per aortic segment
50% Pard3ba attraction distance (in µm)
75% Pard3ba attraction distance (in µm)

Figure 5

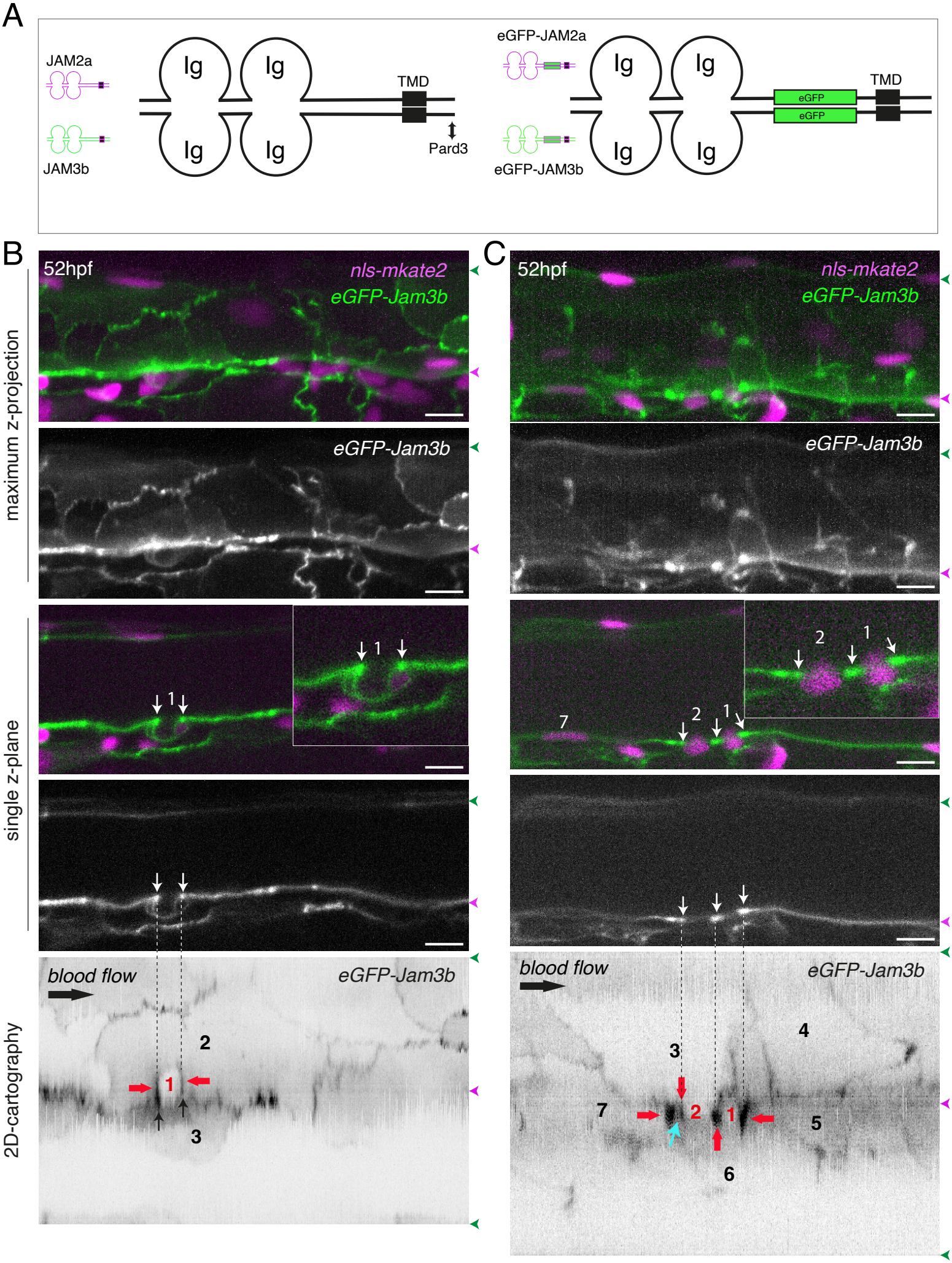
A
JAM2a
JAM3b
Ig
Ig
Ig
Ig
TMD
Pard3
eGFP-JAM2a
eGFP-JAM3b
eGFP
eGFP
TMD
B
C
52hpf
nls-mkate2
eGFP-Jam3b
eGFP-Jam3b
maximum z-projection
single z-plane
2D-cartography
blood flow
eGFP-Jam3b
1
2
3
4
5
6
7

Figure 6

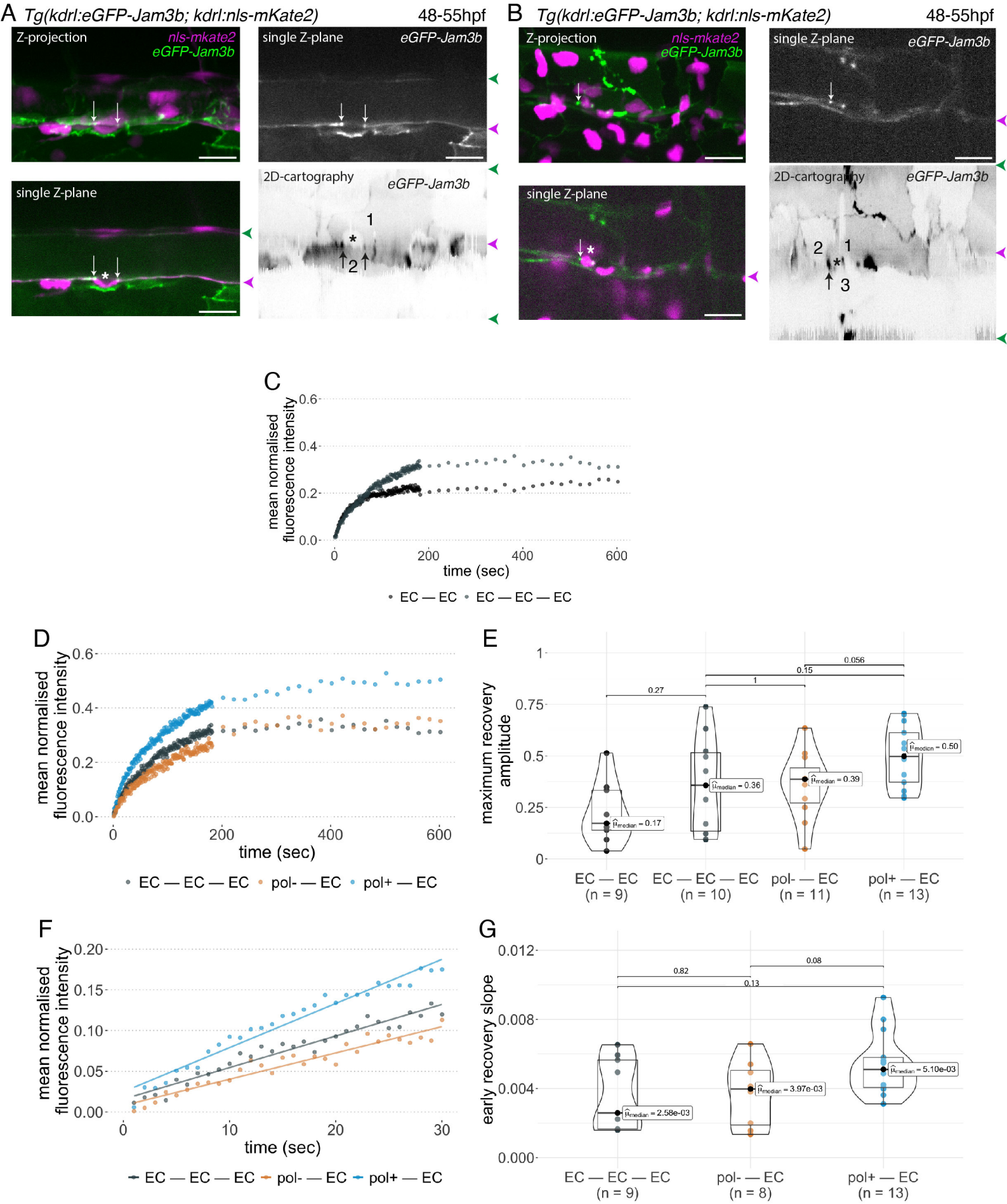
A
Tg(kdrl:eGFP-Jam3b; kdrl:nls-mKate2)
48-55hpf
Z-projection
nls-mkate2
eGFP-Jam3b
single Z-plane
eGFP-Jam3b
single Z-plane
2D-cartography
eGFP-Jam3b
1
2
B
Tg(kdrl:eGFP-Jam3b; kdrl:nls-mKate2)
48-55hpf
Z-projection
nls-mkate2
eGFP-Jam3b
single Z-plane
eGFP-Jam3b
single Z-plane
2D-cartography
eGFP-Jam3b
1
2
3
C
mean normalised fluorescence intensity
time (sec)
EC — EC
EC — EC — EC
D
mean normalised fluorescence intensity
time (sec)
EC — EC — EC
pol- — EC
pol+ — EC
E
maximum recovery amplitude
0.27
1
0.15
0.056
$\hat{\mu}_{median}$ = 0.17
$\hat{\mu}_{median}$ = 0.36
$\hat{\mu}_{median}$ = 0.39
$\hat{\mu}_{median}$ = 0.50
EC — EC (n = 9)
EC — EC — EC (n = 10)
pol- — EC (n = 11)
pol+ — EC (n = 13)
F
mean normalised fluorescence intensity
time (sec)
EC — EC — EC
pol- — EC
pol+ — EC
G
early recovery slope
0.82
0.13
0.08
$\hat{\mu}_{median}$ = 2.58e-03
$\hat{\mu}_{median}$ = 3.97e-03
$\hat{\mu}_{median}$ = 5.10e-03
EC — EC — EC (n = 9)
pol- — EC (n = 8)
pol+ — EC (n = 13)

Figure 7

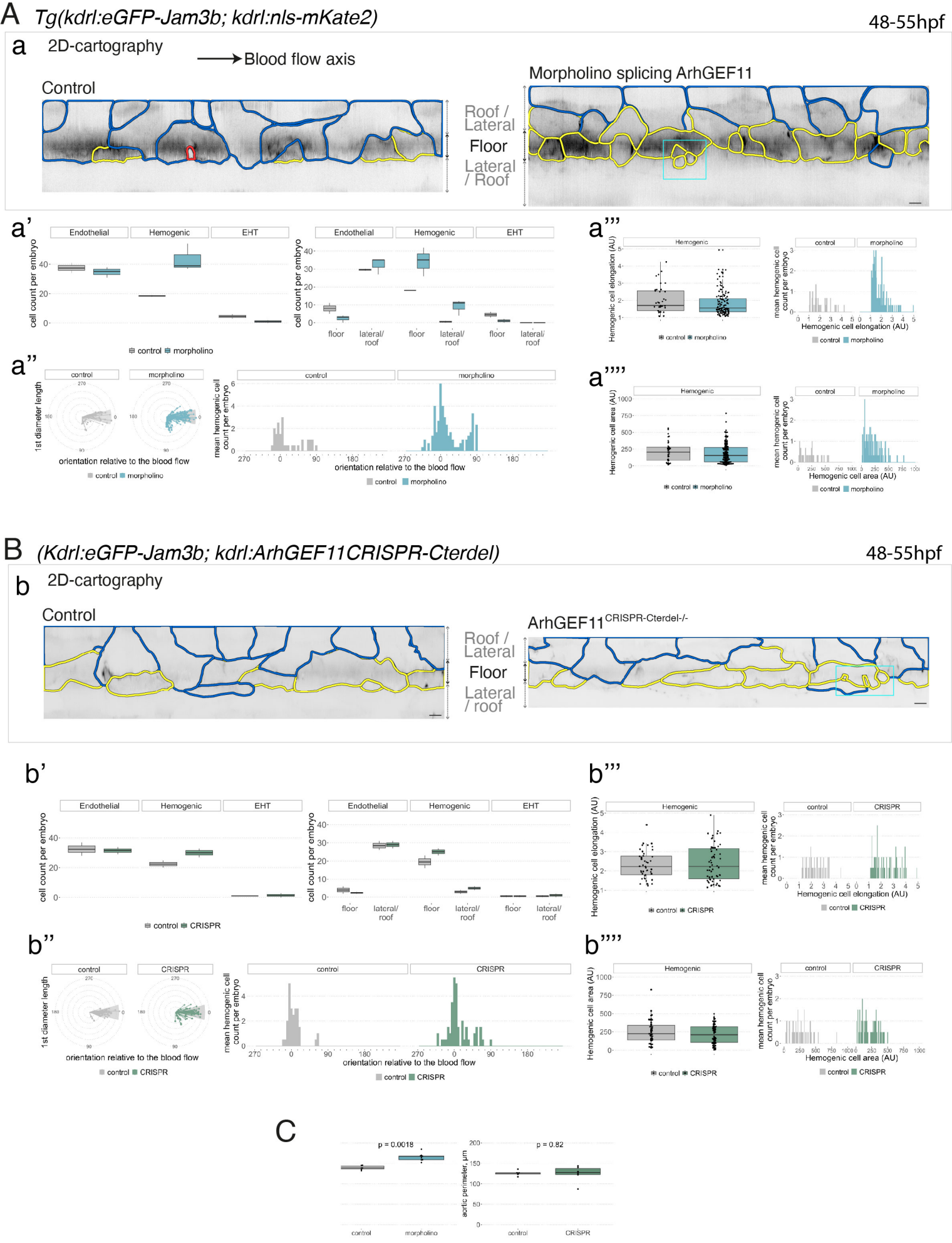
A
Tg(kdrl:eGFP-Jam3b; kdrl:nls-mKate2)
48-55hpf
a
2D-cartography
Blood flow axis
Control
Morpholino splicing ArhGEF11
Roof / Lateral
Floor
Lateral / Roof
a'
Endothelial
Hemogenic
EHT
cell count per embryo
control
morpholino
floor
lateral/ roof
a''
1st diameter length
orientation relative to the blood flow
mean hemogenic cell count per embryo
a'''
Hemogenic cell elongation (AU)
a''''
Hemogenic cell area (AU)
B
(Kdrl:eGFP-Jam3b; kdrl:ArhGEF11CRISPR-Cterdel)
48-55hpf
b
2D-cartography
Control
ArhGEF11CRISPR-Cterdel-/-
Roof / Lateral
Floor
Lateral / roof
b'
CRISPR
b''
b'''
b''''
C
p = 0.0018
p = 0.82
aortic perimeter, µm

Figure 8

A

+ splicing MO ArhGEF11/PDZ-RhoGEF exon38

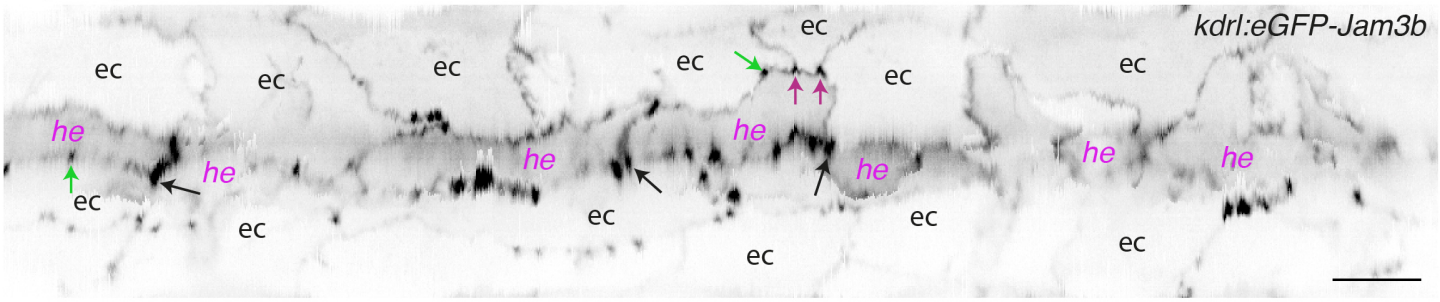

B

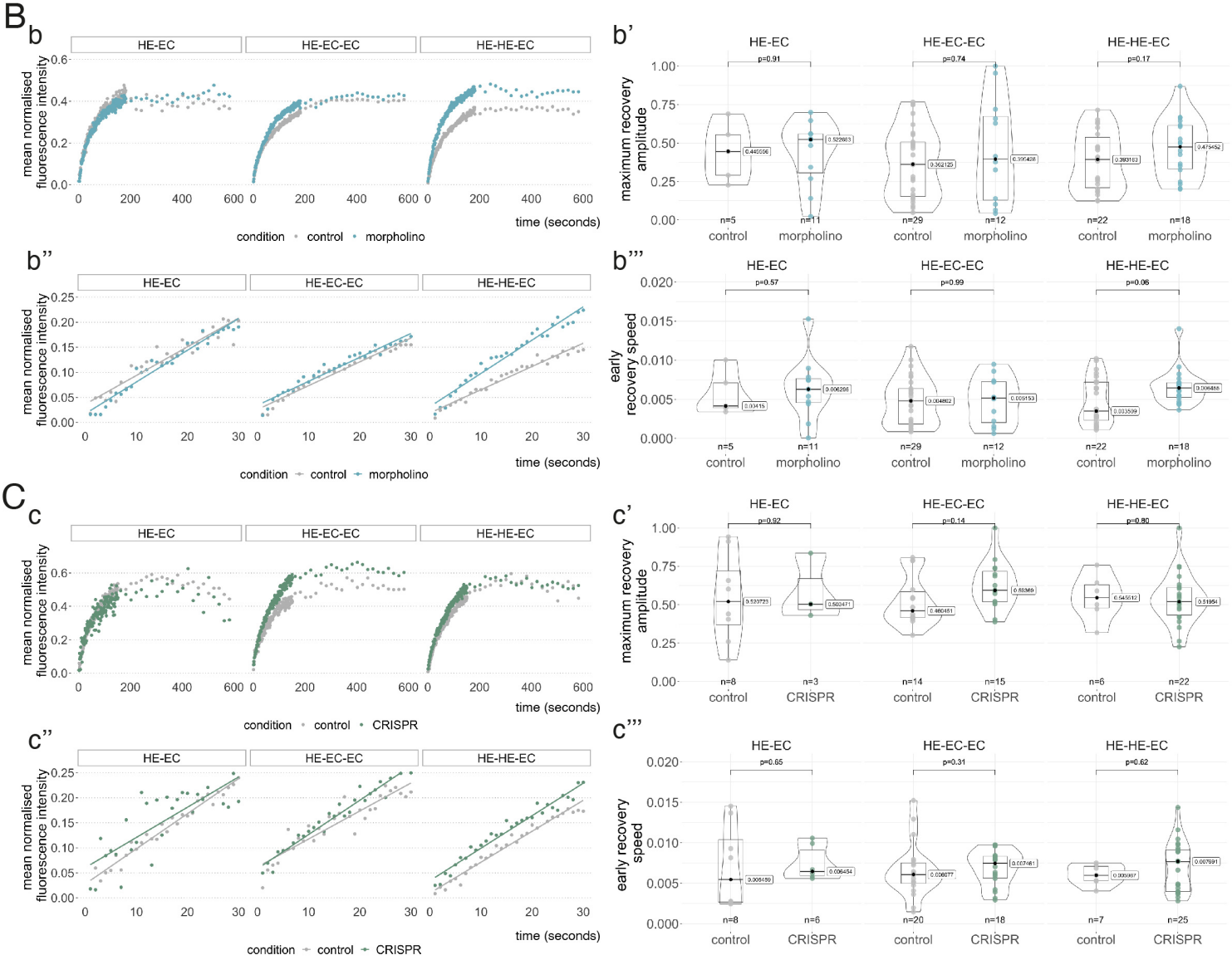

C
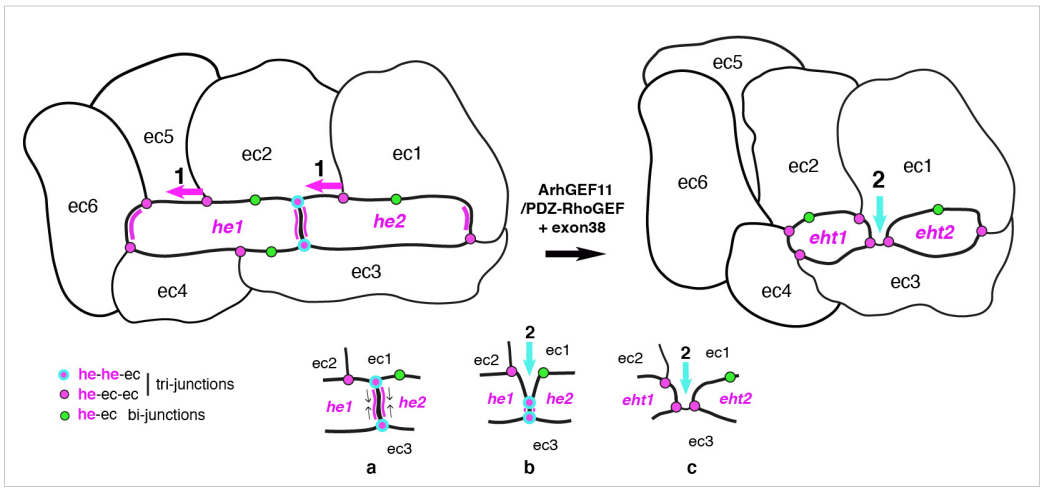
D